Orienting Structure to Serve Medical Functions

by

Huayu Tong

Department of Chemistry
Duke University

Date:_____
Approved:

_____
Benjamin Wiley, Supervisor

_____
Joseph Lo

_____
Jie Liu

_____
Aaron Franklin

Dissertation submitted in partial fulfillment of
the requirements for the degree of Doctor
of Philosophy in the Department of
Chemistry in the Graduate School
of Duke University

2022

ABSTRACT

Orienting Structure to Serve Medical Functions

by

Huayu Tong

Department of Chemistry
Duke University

Date:_____

Approved:

_____
Benjamin Wiley, Supervisor

_____
Joseph Lo

_____
Jie Liu

_____
Aaron Franklin

An abstract of a dissertation submitted in partial fulfillment of the requirements for the degree of Doctor of Philosophy in the Department of Chemistry in the Graduate School of Duke University

2022

Abstract

This thesis explores how the change in material and the structure can better serve medical functions. A 3D printed physical phantom and a hydrogel coated orthopedic implant were developed.

The purpose of physical phantom work was to characterize and improve the ability of fused filament fabrication to create anthropomorphic physical phantoms for CT research. Specifically, we sought to develop the ability to create multiple levels of x-ray attenuation with a single material. CT images of 3D printed cylinders with different infill angles and printing patterns were assessed by comparing their 2D noise power spectra to determine the conditions that produced a minimal and uniform noise. A backfilling approach in which additional polymer was extruded into an existing 3D printed background layer was developed to create multiple levels of image contrast. A print with nine infill angles and a rectilinear infill pattern was found to have the best uniformity, but the printed objects were not as uniform as a commercial phantom. An HU dynamic range of 600 was achieved by changing the infill percentage from 40% to 100%. The backfilling technique enabled control of up to 8 levels of contrast within one object across a range of 200 HU, similar to the range of soft tissue. A contrast detail phantom with 6 levels of contrast and an anthropomorphic liver phantom with 4 levels of contrast were printed with a single material. In conclusion, this work improves the uniformity and levels of contrast that can be achieved with fused filament fabrication, thereby enabling researchers to easily create more detailed physical phantoms including realistic, anthropomorphic textures.

The goal of the orthopedic implant work is to replace the damaged cartilage with a synthetic hydrogel. This requires a method for securing the hydrogel in a defect site with the same shear strength as the cartilage-bone interface. Bonding hydrogel to a titanium base that can in turn bond to bone could enable long-term fixation of the hydrogel, but current methods of forming bonds to hydrogels do not have the shear strength of the cartilage-bone interface. This thesis reports the first method for attaching a hydrogel to metal with the same shear strength as the cartilage-bone

interface. The average shear strength of the junction between 1.2-mm-thick hydrogel and metal made in this manner exceeded the shear strength of porcine cartilage-bone interface. The shear strength of attachment increased with the number of bacterial cellulose layers and with the addition of cement between the bacterial cellulose layers. This new method of attachment will be useful to the creation of hydrogel-coated orthopedic implants for treatment of osteochondral defects.

After creating the bonding between hydrogel and metal base, the thesis then introduces the work of a synthetic hydrogel. The goal of the work is to increase the mechanical strength of the hydrogel, which further increases the shear strength between the hydrogel and metal base. This work shows that reinforcement of annealed PVA with BC leads to a 3.2-fold improvement in the tensile strength (from 15.6 to 50.5 MPa) and a 1.7-fold increase in the compressive strength (from 56.7 to 95.4 MPa). The highly crystallized BC-PVA hydrogel that results from annealing is the first hydrogel with a tensile and compressive strength that exceeds that of cartilage. When tested against cartilage, annealed BC-PVA wore an opposing cartilage surface to the same extent as cartilage and was three times more resistant to wear than cartilage. The improved tensile strength of annealed BC-PVA enabled it to attach to a metal base with a shear strength 68% greater than the shear strength of cartilage on bone. The high strength, high wear resistance, and low COF of annealed BC-PVA make it an excellent material for replacing damaged cartilage.

The wear performance of the BC-PVA hydrogel was further improved by doping nanoclay into original hydrogel network. By using a two-step infiltration, a tensile strength of 37.98 MPa was achieved. The wear of opposing cartilage against the hydrogel was much better compared to cartilage itself. Thus, the nanoclay doped hydrogel also has the potential to be used in actual cartilage repair.

Contents

List of Figures

Acknowledgements

First, I would thank my advisor Dr. Benjamin Wiley for all the guidance and support he provided as well as Dr. Joseph Lo and Dr. Ehsan Samei for the guidance provided in 3D printed phantom project. I would also thank my collaborator, Hope Pegues, Jiacheng Zhao and Alina Kirillova for the wonderful collaborations. I benefit a lot from the assistance they provided to me and the conversation we had. I would thank Cindy Davis for facilitating CT scanning sessions. I would thank all my colleagues in Wiley lab who always willing to help me and talk with me. Finally, I would thank my family for their support and understanding. Without them, I won't focus on the graduate study, I also won't go through all the challenging moments. Thanks for all the efforts you provided to me that make me to be a better person.

1. Introduction

1.1 Motivation of This Work

Medical device is the device intended for serving medical functions, ranging from medical thermometers to implants. A report estimated the spending in 2016 on medical devices and in-vitro diagnostics totaled $173.1 billion in united states. The global medical devices market in 2020 was valued at $456.9 billion, which is an increase at a compounded annual growth rate (CAGR) of 4.4% since 2015.

In order to fulfill the increasing need, medical devices with specific properties need to be developed to better serve the medical functions.

For example, vascular stents, tubular implant that been widely used to open blocked vessels have undergo different design development over time. The bare-metal stents are the first generation and were made of corrosion-resistant materials, such as stainless steel or nitinol (Ni-Ti), they were implanted permanently.[1] The bare-metal stents were just passive mechanical devices and used for providing support for the vessel walls. Then, in 2002, the first DESs (Drug-Eluting stents) were introduced in the market. The structure was based on the previous design, but a drug-eluting durable polymer was coated on the outer surface.[2-4] The new design led to long-term safety and efficacy.

Similarly, by coating the traditional metal orthopedic implant with bioactive ceramics led to better osseointegration with bony tissue,

In terms of changing the structure to derive ideal function, it's also been widely adapted. Bending, torsion, tensile, compression can be implemented by changing the structure of the object. Panetta et al.[5] has shown that the hinge joint can be realized by a single component by changing structure. Tension can be achieved by using auxetic material, torsion can also be achieved by elastic textures.[6]

As a result, in order to better serve medical device, we need to find out the requirement for the specific medical device and then develop suitable materials and changing the structure to achieve the ideal properties that match the requirements.

In this work, I will talk about the work has been done regarding developing two medical devices. The first one is physical phantom and the second one is a hydrogel coated orthopedic implant for cartilage repair.

1.2 3D Printed Physical Phantom for Computed Tomography (CT)

Computed tomography (CT) is a medical imaging technique used to diagnose and screen for a variety of conditions of the head, chest, abdomen, pelvis, and spine.[7] CT is now widely used due to its ability to generate cross-sectional image thus provides more detailed information than the plain X-rays

The utility of CT for diagnosis has led to a 100-fold increase in its use between 1982 and 2006; approximately 80 million scans are performed per year in the US.[8] As it involves an extended exposure to an x-ray source from multiple angles, CT scanning naturally results in a greater x-ray dose that for a conventional x-ray. For example, the x-ray dose from a CT scan of the chest is 60 times greater than for a conventional chest x-ray.[9] Given the important role played by CT imaging and the potential radiation risk, it is critical that the lowest possible dose be used to meet clinical needs.

Since humans cannot be used to optimize CT imaging protocols due to radiation concerns and lack of objective ground truth, phantoms are used to test image quality.[10-13] Commonly used imaging phantoms for CT (e.g. Catphan®, ACR®) consist of simple objects of varying size in a uniform background. These common phantoms lack the physical realism necessary to evaluate the ability of a new imaging system or algorithm to detect clinically relevant tasks such as a small, low-contrast lesion in the complex three-dimensional matrix that is the human body, let alone account for variability in body structure across a patient population.

Virtual phantoms have been developed to create more anatomically realistic images for testing of CT imaging systems.[14-18] By performing a simulation of the CT imaging system *in silico*, it is hoped that virtual phantoms will enable virtual clinical trials to evaluate the performance of new technology.[19-21] It is much easier and cheaper to create the thousands of phantoms necessary to provide a statistical representation of the human population in a computer than with physical models. Although virtual phantoms are much more realistic than commonly used physical phantoms, virtual phantom simulations necessarily involve approximations and corrections to account for imaging processes that are difficult to model or are proprietary, including physical processes such as system noise as well as manufacturer reconstruction algorithms. It is challenging for a virtual imaging platform to account for every aspect of a clinical CT imaging system due to the difficulty of modeling complex physical processes as well as proprietary hardware designs and reconstruction algorithms. Therefore, it may be necessary to use anthropomorphic physical phantoms that are scanned on clinical systems, especially when evaluating new technology for which the accuracy of a virtual imaging simulation is less certain.

Over the last decade, researchers have made great advances in leveraging additive manufacturing to convert virtual phantoms into physical phantoms with increasing accuracy and realism.[22] Methods to convert virtual phantoms to physical phantoms for x-ray imaging include inkjet printing of photocurable resins,[23-25] inkjet printing on paper,[26, 27] and fused filament fabrication.[28-30] Each method has its advantages and disadvantages. Inkjet printing of resins can provide a phantom with features down to ~200 μm, but current commercially available printers (e.g. Polyjet) cost tens to hundreds of thousands of dollars and are closed systems in that they do not allow the owner to use custom inks or printing processes. It can also be difficult to load sufficient concentrations of custom materials into the printing resins to provide contrast without damaging the printer. Inkjet printing on paper is a much cheaper method that also has high resolution, but there are no commercially available systems to automate the stacking and alignment of many pieces of paper to create a phantom. It can also be challenging to load inkjet inks with

sufficient material to provide contrast without negatively affecting the printability of the ink. As paper is used as a substrate, it may be challenging to create a phantom with a low attenuation, such as for the lungs.

Fused filament fabrication (FFF), also known as Fused Deposition Modeling (FDM), can create relatively large objects in a fully automated manner.[31, 32] Although the printing resolution may be limited to 0.5 mm for hobby-level 3D printers, higher resolutions (50-100 μm) can be achieved by higher quality machines. The polymers used for FFF are very low in cost, and the open nature of FFF systems makes it easy to create new materials to mimic the x-ray contrast of different parts of the human body.

To date, studies of FFF for x-ray phantoms have determined the attenuation values for different 3D printing materials and infill densities, and printed 3D models to mimic the shape of bones, arteries, a skull, and the lungs.[28-30, 33, 34] One issue with the FFF models created to date is that they contain two or fewer contrast levels in the same print by either using different materials[29] or different infill densities.[28] If the default printer settings are used for such prints, the printer will create a solid shell at the boundary between the materials, which negatively impacts the realism of the model.[30] In addition, the infill printing pattern is clearly visible in most 3D models reported to date, which results in a distracting texture that does not mimic a uniform background.

In the following chapter, we examine what combination of infill angle and infill pattern most closely mimics a uniform background that minimizes FFF printing artifacts. In addition, we introduce a new approach called backfilling that enables printing multiple contrast levels in one object using a single material while achieving a smoother transition between the contrast levels. These methods are combined to 3D print a contrast detail phantom and liver phantom with multiple levels of contrast, both with a single, standard material. These methods will enable researchers to achieve a new level of anthropomorphic realism with low-cost FFF printers without the need to create custom 3D printing materials.

1.3 Cartilage Repair

Articular cartilage is the thin layer (2-4 mm) of highly specialized connection tissue of diarthrodial joints.[35] The principal function of cartilage is to distribute joints loads, and also to provide a smooth, lubricated surface for the relative movement of opposing joint surface, with minimal friction and wear.[36] Articular cartilage can be damaged due to the acute trauma[37] or cyclic mechanical load.[38, 39] However, mature cartilage doesn't have blood vessels, lymphatics or nerves[35], as a result, articular cartilage has a limited intrinsic healing capacity. Approximately 900,000 people[40] in United States suffer from cartilage damage every year with the knee been mostly affected.[41] 6.5 million of people suffered from arthritis in Canada is estimated to happen by 2031, which is 16% of population.[42] Arthritis also affected 70 million U.S. adults in 2005, and the estimated cost of arthritis was $60 billion, which also expected to increase to $100 billion by 2020.[43] Thus, an effective treatment is essential for the improving people's life quality and relieving the economic burden.

1.3.1 Current Therapies for Cartilage Repair

The treatment of the articular cartilage lesion remains problematic and is dependent on a wide range of factor including the patient's selection, daily activities, age, grade and quality of the lesion.[44] Conservative therapy can be selected when patient experience mild symptom or surgery could do more harm than good. Conservative therapy includes medication, weight loss, bracing, physical therapy, nutrition supply. etc. The goal of conservative treatment is to reduce the pain instead of healing the lesion. The asymptomatic lesion may lead to permanent knee damage, revealed in the long-term follow-up.[45] No structure improvement evidence has been found with the conservative therapy. [46] t

Surgical strategies can be selected for more severe cases, including bone marrow stimulation (microfracture), autologous chondrocyte implantation (ACI) and osteochondral auto/allograft.

Microfracture is to simulate the new cartilage growth by generating new blood supply. Typically, the damaged cartilage was removed by the surgeon, a sharp tool called awl was used to create multiple holes 3-4 mm apart in the subchondral bone area. This also create new blood supply from the bone marrow, along with the new cells which helps to form new cartilage. After the surgery, the patients need to go through strict rehabilitation to prevent excess load bearing in the microfracture area. The recovery may take 4-7 months until the patients can increase the activities.[47] Though improvement was found in the short-term (in 2 years), the long-term failure rate remained an issue. Deterioration was found after 18 months after surgery, especially in the patients older than 40 years.[48] Up to 62%'s long-term failure rate can be found in the cartilage survival test.[49]

Autologous chondrocyte implantation (ACI) is first documented in 1994[50] and is a cell-based treatment. The process is performed in several steps. First, the healthy cartilage sample is harvested from the non-weight bearing area. The sample, which contains healthy cartilage cells (chondrocyte) was cultivated in the laboratory for cell propagation for six weeks. Then, another implantation surgery occurred for implanting the newly grown cell. ACI is mainly used for younger patients with single defects larger than 2–4 sq cm and less than 3-6 mm depth.[51] The short-term failure rate of ACI is 5-13% .[52] But based on the data analysis of Rauno-Ravina and Jato meta[53], they didn't find evidence that ACI is more effective or safe than other conventional techniques. Multiple surgical processes, long rehabilitation time and periosteal flap complications have encouraged research in alternative treatment.[54]

During Osteochondral autologous transplantation (OAT), an osteochondral implant was harvested from the patients themselves in a non-weightbearing area, then the healthy cartilage, the graft was matched to the damaged surface and implanted in the area of defects. A single plug of cartilage or multiple plugs can be taken or transferred in the process. Due to cartilage immune privilege, the immune rejection of non-autologous articular cartilage has seldom been considered, which enables the transplantation of osteochondral allograft. Osteochondral allograft

transplantation has a similar process compared to OAT, except the graft was harvested from a donor instead of patients themselves.

Osteochondral autologous transplantation showed satisfactory results. Smailys et al treated osteochondral defects for 28 athletes, and 96% of them showed excellent results, and 93% of them returned to sports at their preinjury level after 6.5 months.[55] Many studies also showed an overall 85% success rate using free grafts for osteochondral allograft transplantation.[44]

Although with good overall results, the limitation of OAT and osteochondral allograft transplantation prevents further application. Due to the need for healthy cartilage plug from patients themselves in the non-load bearing area, the size of the cartilage defects needs to be small to ensure enough cartilage plug can be harvested.

For osteochondral allograft transplantation, medium to large, full-thickness lesions can be treated. However, fresh allografts, which provide a higher chondrocyte availability, have a higher risk of disease transmission. The cryopreserved frozen grafts reduced the possibility of disease transmission, but with low chondrocyte availability. Only 1% of all cartilage repair surgeries uses fresh allograft due to the limited supply.[56] The cost of the osteochondral allograft transplantation is also high.

Ideally, an artificial osteochondral plug that mimics the structure and properties of an osteochondral allograft can both serve its function and be widely available at a low cost.

1.3.2 Focal Resurfacing

Focal resurfacing is an emerging technique which is using an artificial implant to replace the damaged cartilage surface. Compared to the regeneration method like ACI, it allows immediate weight-bearing. The source is also widely available compared to the OAT. The surgical procedure usually starts with creating a vacant space for the artificial implant, then the implant was inserted in the hole and fixed with built-in fixation components.

Ideally, the artificial implant will match the properties of the actual cartilage. Current commercial implants are mainly made of metal, ceramic and plastic. However, the high COF made it easier to damage the opposing cartilage surface.

In addition, these materials are much stiffer than cartilage and will therefore cause an abnormal stress distribution in the joint, potentially contributing to the damage of surrounding cartilage. The failure rate for such implants is approximately 20% after 4 years.

1.3.4 Hydrogel Resurfacing

Due to the limitation of current focal resurfacing material, hydrogel, which has a lower COF and stiffness, became an emerging material for cartilage resurfacing. We will then talk about the requirement for cartilage-equivalent material

1.3.4.1 Requirement for Hydrogel

To act as a suitable material for cartilage resurfacing, the material needs to have similar or better properties in mechanical strength and stiffness, surface tribology and wear performance and great biocompatibility.

In case of weak mechanical properties, the replacement hydrogel won't be able to stand the load bearing during human activities, thus will lead to a quick failure and a re-surgery. If the COF is too high, it may also cause damage to the opposing cartilage surface.

Ideally, the hydrogel replacement material will be implanted in human body and stay functional in the long term, so we want it to be biocompatible so it won't affect the nearby cartilage or the human body, the hydrogel itself need to be non-biodegradable so it can stay in place for longer time.

Moreover, as an implantable device, the hydrogel needs to be adhered to bone or integrated to a base that can be implanted in the human body. The shear strength between the hydrogel and the substrate needs to be equivalent or higher than the connection between actual cartilage and the subchondral bone. The specific requirement and the current state will be covered in the following sections.

1.3.4.2 Mechanical Strength

The main task of cartilage is to support human body's daily activities over a long time without damage, so it's very important to have sufficient compressive and tensile strength to support the load induced during intensive activities. Human cartilage has a tensile strength range of 8.1- 40MPa, and a compressive strength range of 14-59 MPa.[58-60] The tensile and compressive modulus range of cartilage is 58-228 MPa and 8.1-20 MPa,[58-60] respectively. Currently, few synthetic hydrogels have matched the goal.

Yang et al[61] crosslinked Poly(vinyl alcohol) by 4-carboxyphenylboronic acid (CPBA) in the presence of calcium ions. The gel utilized the dual dynamic crosslinking method to form borate bonds between CPBA and PVA, as well as the ionic interaction between CPBA and Ca^{2+}. The strategy led to a compressive strength of 25 MPa and a compression modulus of 5.6 MPa. Kotov et al[62] reported a hydrogel with aramid nanofibers (ANFs) and PVA to achieve a compressive strength of 26.5 MPa and a compressive modulus of 4 MPa by utilizing the hydrogen boding between ANFs and PVA. Although the compressive strength reported is high, but the compressive modulus was not in the cartilage equivalent range.

Gong et al[63] fabricated a bacterial cellulose (BC) / PAAm double network hydrogel with a tensile strength of 40 MPa and a tensile modulus of 114 MPa, although the tensile strength matched the requirement, the compressive strength was only about 5 MPa, improvement in compressive strength was needed.

Wang et al[64] developed a 3D printable hydrogel consisted of cellulose nanocrystal (CNC) and poly (phenyl acrylate)-acrylamide (PA-AAm) copolymer. The gel introduced the hydrophobic component with has the in the gel which increased the mechanical properties with a highest tensile strength of 16.5 MPa and compression strength of 31.1 MPa, however, the tensile modulus (232.4 MPa) and compression modulus (65.5 MPa) was too big compared to cartilage. But as stated in the paper, the hydrogel performance can be tuned by the formula of the hydrogel, so it's promising that comparable mechanical strength can be achieved.

1.3.4.3 Lubrication and Wear

Another important task of the cartilage is to provide lubrication during the movement of joints, which further prevent wear. The lubrication of the cartilage can be characterized by the coefficient of friction (COF), the COF of cartilage is in the range of 0.001-0.1, however, the COF may relate not only to the material, but also the test conditions, long-term wear test may also be chosen while testing the hydrogel's lubrication properties.

Serro et al[65] developed an annealed PVA hydrogel with a COF of 0.09 between gel and stainless steel balls, 52% smaller than that of cartilage (0.19), the wear performance was not researched.

1.3.4.4 Hydrogel Fixation

Apart from the equivalent mechanical properties compared to cartilage, the hydrogel implant for defect cartilage replacement needs to have strong adhesion to the subchondral bone, ideally comparable to the shear strength of osteochondral junction, which was reported to 7.25 ± 1.35 MPa,[66] however, the commercially available glues do not meet the requirement. Currently, the strongest tissue adhesive report is cyanoacrylate,[67] with a lap shear strength of 0.7 MPa between 2 cartilage pieces. In contrast, the shear strength between nylon to nylon and steel to steel is 2.8 and 7.3 MPa, respectively. The adhesion of hydrogel remains a problem because of its high-water content. Most of the existing tissue adhesive was relied on the diffusion of molecules through water to interact with the polymer network. Research have been done on removing the interfacial water between the two surfaces to form intermolecular bonds inspired by the animals like mussel, barnacle and spider-web glues.[68-70] For example, Zhao et al[71] proposed an adhesive in the form of dry double-sided tape to remove the interfacial water thus received a strong adhesion on the wet tissue. A shear strength of 118 kPa was achieved.

So, in the following chapters, we will talk about the work have done in order to develop a hydrogel coated orthopedic implant. Briefly, in chapter 3, we will talk about a hydrogel fixation strategy which achieve a cartilage-equivalent shear strength between hydrogel and metal base. In chapter 4,

we will talk about the fabrication of a synthetic hydrogel composite which has a 50.5 MPa in tensile strength and a 95.4 MPa compression strength. The hydrogel also has an equivalent or better wear performance compared to cartilage, the shear strength between the hydrogel and the metal base is also larger than pig cartilage. Finally, in chapter 5, we introduced a nanoclay as a doping material to further increase the wear performance of the gel.

2. 3D Printed Physical Phantom for Computed Tomography (CT)

2.1 Introduction

Physical phantoms are commonly used to evaluate and calibrate medical imaging systems, but commercially available phantoms are costly and do not accurately reflect the structure of the human body. 3D printing can potentially solve these problems, and enable printing of realistic, patient-specific phantoms for the planning of surgeries or irradiation. The ideal 3D printing approach would create physical phantoms with the structures and HU values that mimic human organs and contrast agents. In addition, such an approach would be open rather than closed so as to enable the rapid development of new printing techniques and materials by the users. At present no 3D printing approach has met these criteria. The material set currently available for 3D printing is limited and does not intrinsically match the HU values of human organs, let alone contrast agents such as iodide. Researchers have developed ways around the limited materials set by filling in 3D printed molds with materials that have the target HU values,[72-74] but this approach lacks the convenience of a completely 3D printed phantom. Researchers has done utilized several additive manufacturing technique to create physical phantoms, include inkjet printing of photocurable resins,[23-25] inkjet printing on paper,[26, 27] and fused filament fabrication.[28-30]However, each method has its own advantages and disadvantages. Inkjet printing of resins has a high printing resolution, but the commercially available printer and printing resins are of high cost. The close-system nature of this printing method disables the ability to use customized materials, which limits the change in the phantoms' contrast level and material composition. Inkjet printing on paper also provides a high resolution, but it can also be challenging to load inkjet inks with sufficient material to provide contrast without negatively affecting the printability of the ink.

Although the resolution of FFF printing is typically limited to 0.5 mm for hobby-level printers, higher cost printers such as the nscrypt can easily achiever resolutions of 50 – 100 μm. FFF printers also offer the ability to print multiple materials of the owner's choice, including

materials that are custom made to mimic the contrast level of human anatomy. While the PolyJet printer costs several hundred thousand dollars, excellent FFF printers can be purchased for less than a few thousand dollars. These attributes make FFF an attractive printing modality, especially for CT imaging phantoms for which 0.5 mm resolution may be sufficient.

In this chapter, we examine what combination of infill angle and infill pattern most closely mimics a uniform background that minimizes FFF printing artifacts. In addition, we introduce a new approach called backfilling that enables printing multiple contrast levels in one object using a single material while achieving a smoother transition between the contrast levels. These methods are combined to 3D print a contrast detail phantom and liver phantom with multiple levels of contrast, both with a single, standard material. These methods will enable researchers to achieve a new level of anthropomorphic realism with low-cost FFF printers without the need to create custom 3D printing materials.

2.2 Material and Methods

2.2.1 CT Imaging

CT images were acquired with the Discovery 750 HD from GE Healthcare using the standard chest protocol with tube potential of 120 kV and current of 99 mA. An Axial scan mode was used. The rotation time was 0.4 s. The CT slice thickness is 0.625 mm. The filtered backprojection algorithm with STANDARD reconstruction kernel was used for every image. As an example of a commercial phantom made of uniform, tissue-equivalent material, a CT phantom insert representing blood (Multi-Energy CT Phantom, Gammex Inc., Middleton WI) was imaged with the printed objects as a control. The CT images shown are all single CT slices. The HU values are averaged over 20 slices. The standard deviation is averaged over 20 standard deviation numbers in each CT slice.

2.2.2 NPS Analysis

In the daily quality control of a CT scanner, the noise of the system is one of the key parameters that is examined. The phantom fabrication process may also result in intrinsic, structure noise that will affect the ability to create and discern features of interest. Thus, we first sought to minimize the noise level inherent to the FFF printing process. This was done by both examining the uniformity of the CT images, and plotting their 2D noise power spectrum (NPS).[75] The infill print pattern and number of infill angles was varied to minimize structure noise as seen on the NPS. The NPS analysis of the print was performed on 20 CT slices for each object using imQuest available via TG233.[76]

2.2.3 3D Printing

The FFF printing process involves creating a 3D model, converting it to an STL file, and converting the STL file to G-CODE instructions for the 3D printer. All the models with the exception of the liver were designed in Fusion 360 (Autodesk, San Rafael CA) and exported as an STL file for slicing. The STL files were sliced by Simplify3D (Simplify3D Software, Cincinnati OH) and exported as G-CODE for printing with a PRUSA MK3 (Prusa Research a.s. Czech Republic). The filament used throughout the study was polylactic acid (PLA, MatterHackers Inc. Lake Forest, CA, pro series silver) with a diameter of 1.75 mm.

For FFF printing, the filament is extruded through a heated nozzle (the print head) and deposited on a substrate as lines. The infill angles control the direction of extruded lines, and the infill pattern controls the pattern of the lines in 1 layer. The infill percentage is the amount of material that occupies the internal part of the print. By varying the infill percentage, one can change the amount of material deposited at the desired region. The infill percentage can be varied from 0% (hollow) to 100% (solid).

All prints were performed with a layer thickness of 0.2 mm, a printing temperature of 200 °C, a bed temperature of 60 °C, and a nozzle diameter of 0.4 mm. These are default print settings. All models were printed without a solid top and with 3 bottom layers with 100% infill.

The printing speed was 20 mm per min for the first layer, and 60 mm per min for the subsequent layers. The fan speed was 0 for the first layer and 100% for the other layers. A cylinder 30 mm in diameter and 0.4 mm height was printed in parallel with the object to enable the nozzle temperature to reach steady state after the fan was turned on between the first and second layers, i.e., the second layer of the 30 mm cylinder was printed before the second layer of the object.

The shell is a solid outline extruded on the outer surface of the object, serving as the outer wall of the print. The existence of a shell usually results in a high-density wall between 2 objects or surfaces. For printing the 2-level contrast model with shell or no shell, a 3D model of a cylinder 20 mm in diameter and a ring with an outer diameter of 30 mm and an inner diameter of 20 mm was loaded into Simplify3D. The inside cylinder and outside ring were assigned an infill percentage of 80% and 85% respectively. For printing the model with the shell, the number of shells was 1 and the outline overlap was 15%. For the print with no shell the outline overlap was 99%.

For the process of backfilling, which is essentially printing twice in the same location, a model for the background and a separate model for the backfilled volume were loaded into the software at the same time. We start with a background layer that has an infill percentage of 80% (HU = -150) and backfill in order to achieve the range of -150 to 50 HU that is typical for a human organ.[77] The infill percentage for the backfilling step was chosen to be 60% to ensure the print pattern was not visible. However, printing one layer within another will increase the height of the backfilled region, so the extrusion multiplier, which controls the material flow rate, must be reduced from the default value of 1 to prevent the printer nozzle from colliding with the backfilled region. From empirical testing, extrusion multiplier values between 0.1 and 0.4 avoided collision while extruding a consistent, continuous filament during printing.

For the contrast detail phantom, a cylinder 165 mm in diameter was printed as the background with an infill of 80%. Five backfilling processes were printed on the background with an extrusion multiplier between 0.1 and 0.3 with an increment of 0.05.

One CT slice of an XCAT Phantom[14] was manually segmented into 3 ranges denoted as "low" (184-224 HU), "high" (225-495 HU), and "all" (-50-495 HU). Each segmented image was converted into STL format, then loaded into Simplify3D for printing. The liver was embedded in a background cylinder with a diameter of 190 mm and an infill of 70% to avoid imaging artifacts. The "all" surface was printed with an extrusion multiplier of 0.15 to provide the cylinder background. The "high" and "low" surfaces were printed with the extrusion multiplier of 0.25 and 0.15, respectively, on the "all" section to achieve the desired anthropomorphic pattern.

2.3 Results

2.3.1 Uniformity

Before modifying the HU values of the phantoms, we first sought to create a phantom with a uniformity approaching that of a commercial phantom. First, we modified the number of infill angles. Figure 1A shows images taken from the Simplify 3D Software showing how changing the number of infill angles changes the appearance of a rectilinear infill pattern. The lines in this image are the path taken by the 3D printer's extruder. Note that the software image shows a 10% infill to better visualize the print plan, but that the actual cylinder was printed with 80% infill. As can be seen in Figure 1A-C, a commonly used rectilinear infill pattern with 2-angles is clearly visible in the CT image and there is a strong cross-like pattern in the 2D NPS. By averaging over up to nine infill angles, the infill pattern was no longer visible in the CT image, and the background appeared more random. The 2D-NPS pattern also showed less structure noise except for a peak at one specific frequency (about 0.5 mm^{-1}). Based on these results, nine infill angles were used for the rest of the printed objects discussed in this study.

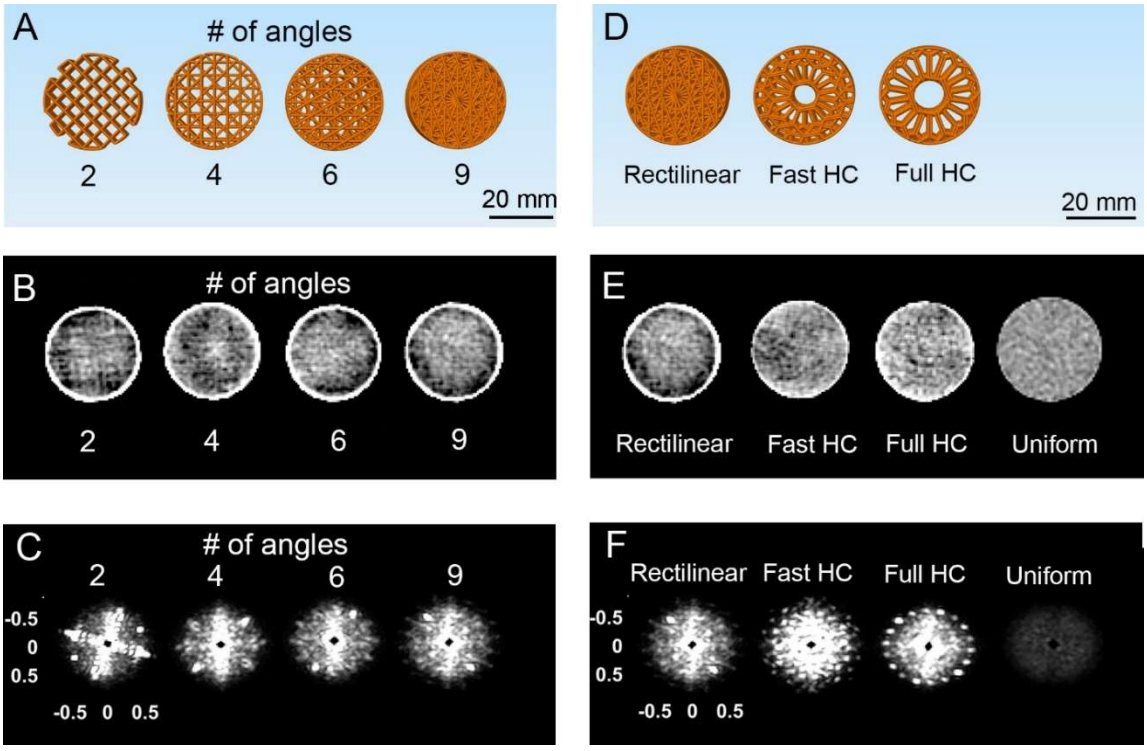

Figure 1 . (A) Simplify 3D software images for a rectilinear pattern with 2, 4, 6, or 9 infill angles and a 10% infill percentage for a cylinder 30 mm in diameter and 20 mm in height. (B) Single-slice (0.625 mm-thick) CT images of cylinders printed with the different infill angles shown in A, but with 80% infill. The CT image window width is 50 HU. (C) 2D NPS of the cylinders in Figure 1B. (D) Simplify 3D software images for different infill patterns. (E) CT image with a window width of 50 HU. (F) 2D NPS of cylinders with rectilinear, Fast Honeycomb, or Full Honeycomb infill pattern, printed with 9 angles and 80% infill. A "uniform" commercial phantom representing blood is included in E&F for comparison. The NPS window is [0,100] for all objects.

Besides the number of infill angles, the print pattern also has an effect on the uniformity of the CT image. Figure 1D-F compares a Rectilinear infill pattern to two others, Fast Honeycomb (Fast HC) and Full Honeycomb (Full HC). The rectilinear pattern with 9 angles is the most uniform as judged by the 2D NPS, but it also has a bright outer shell. The Full HC infill results in a more obvious pattern in the 2D NPS than the other two, likely because the size of the hole in the object is much larger than the others. For the Fast Honeycomb pattern, the 9-angle pattern can be seen in the 2D NPS. Based on these results, we find the rectilinear pattern in Figure 1F with 9 infill angles provides the most uniform background.

2.3.2 Creating Multiple Levels of Contrast

After optimizing the infill angle and pattern to maximize the uniformity of the printing objects in CT images, we next turned to improving control over the attenuation value of the print. As was demonstrated in previous studies,[28-30, 33, 34] a simple way to control the attenuation value of a print is to change the infill density. Figure 2 illustrates the effect of the infill percentage on the appearance and the HU value of test cylinders (20 mm in diameter and 30 mm in height). As shown in Figure 2C, when the infill percentage is low (20%), the print pattern is easily visible in the CT image, a condition that makes this infill percentage unsuitable for mimicking the texture of tissue. When the infill percentage is 40% or higher, the print pattern is not as obvious. Figure 2D demonstrates a linear relationship between the attenuation and the infill percentage. The typical attenuation range for soft tissue is -150 to 50 HU. This same range of contrast can be achieved using 80% to 100% infill.

Although the infill percentage can create multiple levels of contrast in the same object, it is challenging to make a smooth transition between different infill percentages. The default approach to printing multiple levels of contrast is shown in Figure 3A for a cylinder with two infill percentages. The software creates a two-layer-thick shell between the two areas of infill, which shows up as a bright line in the CT image (Figure 3D). If the shell is removed (Figure 3B), there is still a third level of contrast in between the two cylinders (Figure 3E). The presence of a shell in the CT image of the "no shell" cylinder is due to an artifact of the printing process. Figure 3B shows the path taken by the 3D printer's extruder results in u-turns at the interface between the inner and outer shell. Excess material tends to be extruded at these turning points, resulting in the observed shell. To address this issue, we devised the backfilling method illustrated in Figure 3C, in which we first print a background layer, and then extrude additional polymer into a desired region. Backfilling is essentially printing twice in the same position. As shown in Figure 3F, this method allows one to achieve two adjacent regions with different densities without an additional boundary in the transition region.

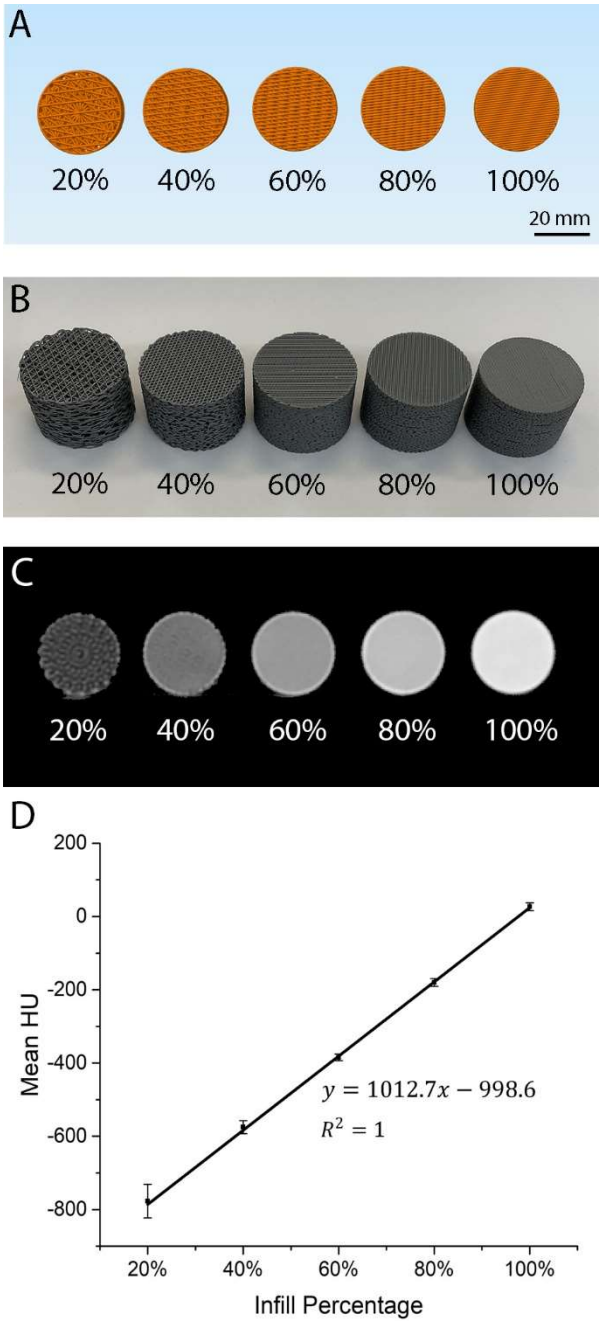

Figure 2 . (A) Simplify 3D software images of cylinders with different infill percentages for test cylinders 30 mm in diameter and 20 mm in height. All cylinders were printed using nine random infill angles. (B) Camera images of cylinders with different infill percentages. (C) CT image of cylinders with infill percentages ranging from 20% to 100%. The window width is 1250 HU. (D) The linear fit between mean HU and the infill percentage.

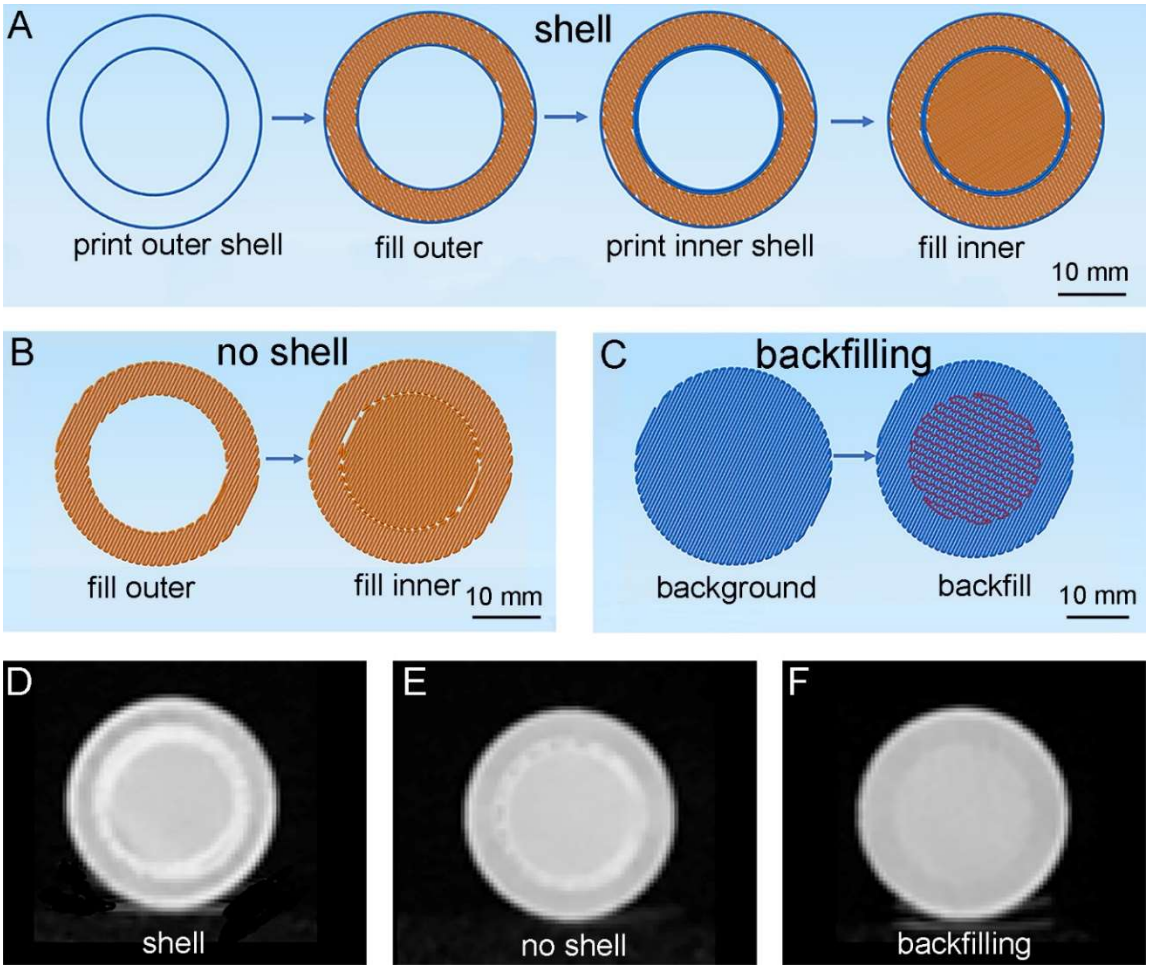

Figure 3. Simplify 3D software images for prints with (A) shell, (B) no shell, and (C) backfilling. (D-F) The corresponding CT images with a window width of 1250 HU. The outer ring or background regions were printed with nine infill angles and 80% infill with a rectilinear pattern. Shell and no shell are printed with a rectilinear pattern and infill percentages of 85% in the center. The backfilled region was printed with a 60% infill and Fast HC pattern with an extrusion multiplier of 0.2.

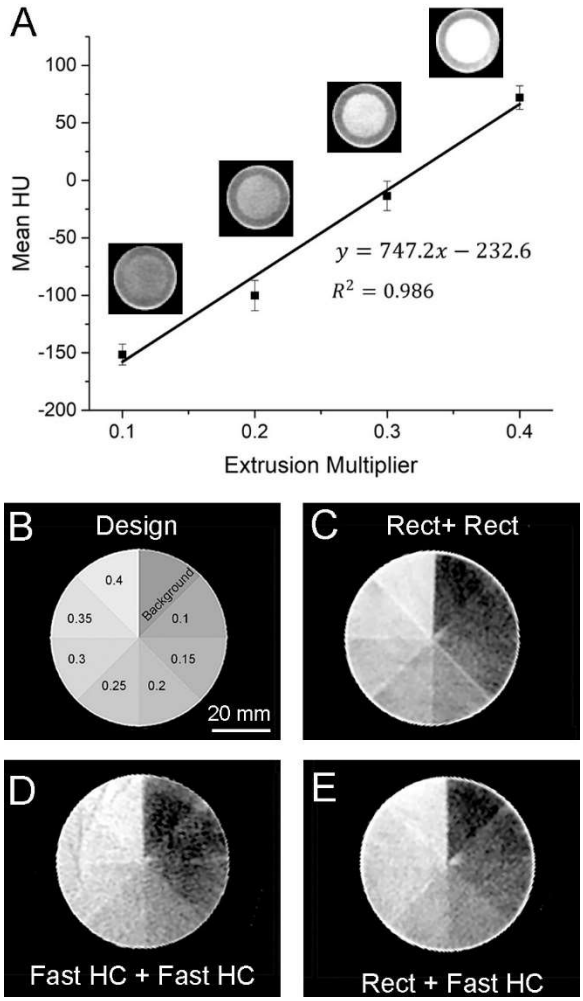

Figure 4. (A) Calibration fit for the HU value vs. extrusion multiplier. (B) Design of an 8-piece-pie denoting regions with different extrusion multipliers. (C-E) CT images of printed pies with different infill patterns. The CT window width was 250 HU for all images.

Figure 4A shows the linear relationship between the extrusion multiplier, a number which controls the material flow rate, used during backfilling and the corresponding HU value of the backfilled region. The standard deviations indicate that regions with an extrusion multiplier difference of 0.05 will have a measurable difference in their HU value. This suggests that the backfilling method can create objects with up to 8 levels of contrast with a single material. To test this possibility, we created a pie model (Figure 4B) wherein each backfilled slice of the pie used a different extrusion multiplier value. Figure 4C shows the CT image of the model created with a

rectilinear printing pattern. Although eight contrast levels are clearly visible in the CT image, there is also a thin line of higher contrast between the printed regions due to the over-extrusion from the nozzle when it changed directions. Switching the background and backfill pattern to Fast HC removed the problem of the high contrast boundary. However, the Fast HC method results in dark line artifacts visible in the print (upper left of Fig 4D) due to under-extrusion when a new extrusion process starts. Using a rectilinear background with a FAST HC infill can reduce both the high contrast boundary and the dark line artifacts. This printing approach allows up to eight levels of contrast with a smooth transition between adjacent regions.

Figure 5. (A) Simplify 3D software image showing the dimensions of the printed areas (3 – 20 mm). The different colors in (A) represent different printing processes with extrusion multipliers of 0.1, 0.15, 0.2, 0.25, 0.3 respectively. (B) Optical image of the contrast detail phantom. (C) CT image with a window width of 280 HU.

2.3.3 Phantom Applications

To demonstrate the clinical utility of this new printing methodology, we fabricated a contrast detail phantom containing targets with sizes and contrast levels embedded in a uniform background. This design was based on a previous phantom fabricated using polymer inkjet printing.[78] Figure 5 shows the design and resulting CT image of our contrast detail phantom, which contains 5 different contrast levels and 4 different sizes of cylindrical objects ranging from 3 mm to 20 mm.

As a second application we demonstrate the printing of an anthropomorphic phantom based on a virtual XCAT liver phantom (Figure 6A). The three contrast levels were printed with three backfilling processes on a cylindrical background, as illustrated by the design in Figure 6B. As can be seen in the resulting CT image of the printed liver phantom (Figure 6D), the details of the patient liver were replicated by the printed liver phantom.

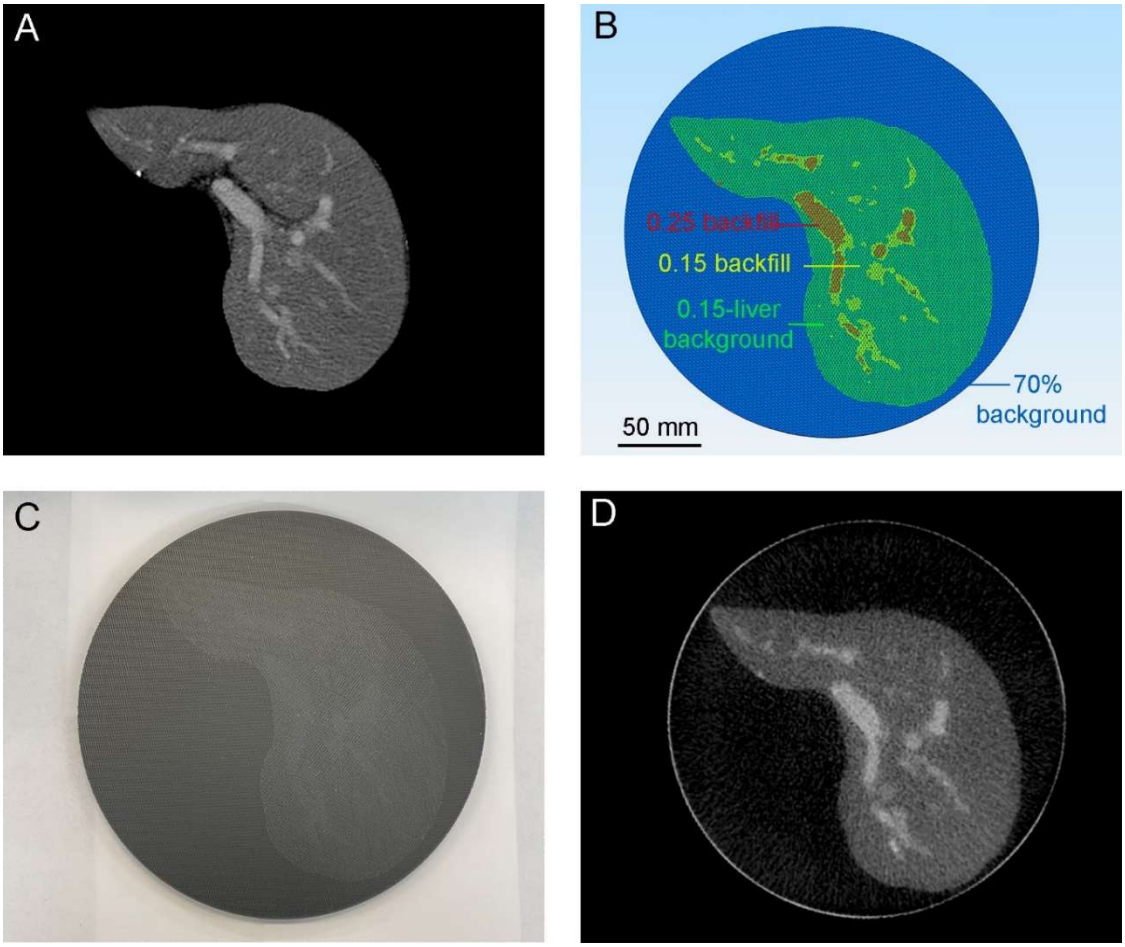

Figure 6. (A) Simulated CT image of virtual XCAT liver phantom. (B) Software design of the liver phantom. (C) Optical image of the printed liver phantom. (D) CT image of the printed liver phantom with window width of 350 HU. The phantom was printed with a 70% infill, rectilinear pattern for the cylinder, 60% infill, Fast HC pattern with an extrusion multiplier of 0.15 for the liver background, and 60% infill, Fast HC with an extrusion multiplier of 0.15 and 0.25 for the low contrast and high contrast regions, respectively.

2.4 Discussion

There is great interest in research related to optimization of CT technology. Virtual simulation offers diverse phantom designs and allows precise control over experimental parameters but may not be accurate enough for certain tasks such as simulation of system noise or proprietary reconstruction algorithms. Physical phantoms with known structure act as reference standards that are widely used for research and for quality assurance of clinical scanners. Current commercial CT phantoms have a uniform background and relatively simple shape, and thus cannot fully represent the complexity of human anatomy, giving them limited utility for patient-specific research. In an attempt to address the lack of realistic commercial phantoms, this study proposes new methods to fabricate physical phantoms with anthropomorphic structure and multiple levels of contrast.

3D printing is used because of its ability to create complicated shapes and designs with ease. Among various printing techniques, FFF was chosen for its many practical and unique characteristics. First, it is widely available and very cost effective. Our current printer and parts cost less than $3,000 and the materials cost $20/kg. Second, the open software allows custom control over parameters including the extrusion factor as well as devising new procedures such as backfilling. Third, FFF offers the ability to use a wide range of commercial and custom materials. By spanning the extremes from air to high density materials, FFF boasts a very wide dynamic range. In comparison, other techniques such as inkjet printing on paper require a substrate which imposes a baseline attenuation, which is undesirable for applications requiring very low attenuations such as lung phantoms.

Previous FFF-based phantoms were limited by the relatively simple printing pattern, resulting in obvious linear texture artifacts visible in the resulting CT image.[29, 30] We solved this problem by increasing the infill angles and optimizing the infill pattern during the printing process. As a result, the uniformity is improved after optimizing the printing parameters, both visually and in the 2D NPS.

Previous studies reported that the contrast level of the print can be changed by using different materials or by changing the infill percentage.[28-30, 33, 34] A different artifact arises, however, because current FFF phantoms do not have a smooth transition between two contrast levels. Instead, there is often an unrealistic boundary. Our proposed backfilling method solves this problem. Using rectilinear as the background infill pattern and fast honeycomb as the backfilling pattern led to the combination of uniform background and smooth transition between different contrast levels. The contrast levels within the backfilling region can also be controlled by varying the extrusion multiplier. Unlike previous reports limited to two contrast levels,[29, 30] our method can print up to eight levels of contrast in a single object.

The usefulness of our proposed techniques was demonstrated by designing and fabricating two medical imaging phantoms. First, we created a contrast-detail phantom. Unlike commercial phantoms that can cost thousands of dollars, this 3D-printed one can be created in 24 h for about $20 in material. Second, we showcased the ability of FFF to reproduce anthrophonic structure by creating a liver phantom with 4 levels of contrast and irregular shape. Such fabricated phantoms can be used in CT research including task-specific assessment of imaging technology or patient-specific optimization of acquisition protocols.

This study has several limitations. First, even after the optimization of the printing parameters, the 3D printed phantoms are less uniform than the commercial phantom used for comparison. A higher resolution FDM printer with a smaller nozzle size and finer motor control may address this problem, with the tradeoff of longer printing time and higher printer cost. The resolution of the current printer also makes it difficult to backfill regions less than 2 mm in diameter. In addition, there is some deviation between the desired and the actual contrast levels, which may be aggravated within a small region of the printed object due to inaccurate motor movements with a small amount of filament. These issues may be solved with a printer with more advanced motor and extrusion control.

Currently we are using a single material to provide the attenuation difference within the CT image, which may be adequate for evaluating non-contrast protocols on conventional CT systems. However, dual energy or photon counting CT requires discerning other materials like iodine or calcium. This can be potentially solved by multi-material printing using commercial or customized filaments, thanks to the open nature of FFF. Future work may focus on using the backfilling method and optimized printing parameters with multiple materials to create phantoms with multiple attenuation levels and material properties that are clinically relevant.

2.5 Conclusion

By demonstrating a new method to obtain up to eight levels of contrast with a single material, this study has improved the ability of fused filament fabrication to create realistic physical phantoms for CT imaging research. This study also describes the printing parameters that optimize the uniformity of a printed phantom area, and how to obtain smooth transitions between areas with different HU values. The utility of these methods was demonstrated by creating a contrast detail phantom with 6 levels of contrast and anthropomorphic liver phantom with 4 levels of contrast. The low-cost and easily customizable phantoms described here could facilitate the improvement of CT imaging protocols and the characterization of CT imaging systems.

3. Attaching Hydrogel to Metal with the Shear Strength of the Cartilage on Bone

3.1 Introduction

The highest reported shear strength (2.28±0.27 MPa) for a hydrogel on titanium was achieved by first bonding freeze-dried bacterial cellulose (BC, which consists of a network of celluose nanofibers) to titanium with an α-tricalcium phosphate (α-TCP) cement, followed by infiltration of polyvinyl alcohol (PVA) and poly(2-acrylamido-2-methyl-1-propanesulfonic acid (PAMPS) into the bacterial cellulose to create a BC-PVA-PAMPS hydrogel.[71] This approach was named Nanofiber-Enhanced STicking (NEST). Although the shear strength achieved with NEST represented a three-fold increase over the state-of-the-art, it did not achieve the highest values of the shear strengths (7.25±1.35 MPa) that have been reported for the human osteochondral junction. In addition, the way in which the shear strength of the samples was tested in that previous work, i.e., in a plug-to-plug orientation, did not allow for direct comparison with the shear strength of cartilage with the same test fixture.

The goal of this work was to increase the adhesive shear strength between a hydrogel and a metal substrate so that it matched the shear strength of attachment between cartilage and bone in the same test fixture. To do this, several alternative cements were compared to α-TCP. Although these alternative cements increased the shear strength of attachment between porous titanium plugs, they did not increase the adhesive shear strength between the BC-PVA-PAMPS hydrogel and porous titanium. We hypothesized the shear strength of the hydrogel on titanium was limited by delamination of the cellulose nanofiber layers, which are oriented parallel to the direction of the applied shear force. This hypothesis was tested by wrapping the BC layer over the sides of the cylindrical metal plug such that the cellulose nanofibers were oriented perpendicular to the direction of the applied shear force. The BC layers and the resulting hydrogel were secured in place with a shape memory alloy clamp. This change in nanofiber orientation increased the shear strength of attachment to be equivalent to the porcine osteochondral junction in the same test fixture. In this

orientation, the shear strength of attachment increased with the number of BC layers, which increased the force required to fracture the hydrogel at the periphery of the plug. This new method of hydrogel attachment will be useful to those seeking to develop orthopedic devices with surfaces that mimic the properties of cartilage.

3.2 Material and Method

3.2.1 Materials

Bacterial Cellulose (BC) was purchased from Gia Gia Nguyen Co. Ltd. Poly(vinyl alcohol) (PVA) (fully hydrolyzed, molecular weight: 145,000 g mol-1), N,N'-methylenediacrylamide (MBAA, 97.0%), 2-hydroxy-4'-(2-hydroxyethoxy)-2-methylpropiophenone (I2959), potassium persulfate (KPS), 2-acrylamido-2-methylpropanesulfonic acid sodium salt (AMPS, 50 wt.% solution in water) and phosphoserine were purchased from Sigma Aldrich. Phosphate buffered saline (PBS) was purchased from VWR International. Ti-6Al-4V ELI (Grade 23) powder was purchased from 3D Systems. α-tricalcium phosphate (α-TCP) was purchased from Goodfellow Corporation. 100 mesh stainless steel powder was purchased from Alfa Aesar. Zinc phosphate cement was purchased from Prime-Dent. RelyX Luting 2, RelyX Unicem, RelyX Ultimate cements and the Scotchbond Adhesive were purchased from 3M ESPE.

3.2.2 Additive Manufacturing of Titanium

Titanium plugs were fabricated via selective laser melting (SLM) of Ti-6Al-4V ELI powder on a titanium substrate in an inert argon atmosphere using a 3D Systems DMP ProX 320. Plugs were designed to have a diameter of 6 mm and a height of 6.35 mm. The top 1 mm of the plug was composed of a porous strut structure with a porosity of 70%, as reported previously.[71] After printing, the samples were removed from the build plate via wire electrical discharge machining and cleaned by sonication for 15 min in DI water to remove the excess unadhered powder.

3.2.3 Preparation of Samples for Cement Shear Testing

Several cements were tested between two porous titanium plugs. To prepare the sample with α-TCP cement, a dry cement mixture consisting of 0.040 g phosphoserine (PPS), 0.312 g of α-TCP and 0.048 g of stainless-steel powder (SSP) was placed into a small dish, 0.140 ml of water was added, and the powder was rapidly mixed with the water. Approximately 0.150 ml of the wet cement mixture was added on top of a porous titanium plug in a metal die with an inner diameter of 6 mm. A second titanium plug was immediately placed into the die with the porous layer in contact with the wet cement, and the sandwich structure was pressed together for 1 hour at 250 MPa. The sample was placed into water at 85°C for at least 24 hours to facilitate the transformation of α-TCP into hydroxyapatite and was stored in water until just prior to shear testing.

To prepare the sample with zinc phosphate cement, approximately 1 g of the liquid was mixed with 2 g of powder for 90 seconds. The addition of the powder into the liquid was carried out slowly, smoothly and carefully with constant stirring. After that, approximately 0.150 ml of the wet zinc phosphate cement mixture was added on top of the first porous titanium plug in a metal die with an inner diameter of 6 mm. The second titanium plug was immediately placed into the die with the porous layer in contact with the wet cement, and the sandwich structure was pressed together for 1 hour at 250 MPa with a hydraulic press or for 2 minutes by hand. After the cement was completely dry (~2 hours), the sample was placed into water at 22°C for at least 24 hours and was stored in water until just prior to shear testing.

To prepare the sample with RelyXTM Luting 2 and RelyXTM Unicem cement, approximately 0.150 ml of the wet RelyXTM Luting 2 or RelyXTM Unicem cement mixture was added on top of the first porous titanium plug in a metal die with an inner diameter of 6 mm. The second titanium plug was immediately placed into the die with the porous layer in contact with the wet cement, and the sandwich structure was pressed together for 1 hour at 250 MPa with a hydraulic press or for 2 minutes by hand. The sample was placed into water at 22°C for at least 24 hours and was stored in water until just prior to shear testing.

To prepare the sample with RelyXTM Ultimate cement, Scotchbond Adhesive was first applied to the porous surfaces of both titanium plugs. The adhesive was allowed to set for 20s before being blown by air for another 5s. After that, approximately 0.150 ml of the wet RelyXTM Ultimate cement mixture was added on top of the first porous titanium plug in a metal die with an inner diameter of 6 mm. The second titanium plug was immediately placed into the die with the porous layer in contact with the wet cement, and the sandwich structure was pressed together for 1 hour at 250 MPa with a hydraulic press or for 2 minutes by hand. The sample was placed into water at 22°C for at least 24 hours and was stored in water until just prior to shear testing.

3.2.4 Preparation of Freeze-Dried BC

All hydrogel samples were made with freeze-dried BC. BC sheets were cut and placed between 2 metal plates. A 6.59 kg weight was applied to the metal plate to flatten the BC sheets. The BC sheets were frozen at -80 ℃ and then in liquid nitrogen. Note that if the BC sheets are placed directly into liquid nitrogen without the pre-freezing step they fractured. The BC sheets were then removed and freeze-dried at -78°C for 24h.

3.2.5 Preparation of Samples for Hydrogel Plug-to-Plug Shear Testing

Several cements were used to attach the hydrogel between two porous titanium plugs to test the adhesive shear strength.

For the α-TCP sample, a cement mixture consisting of 0.080g PPS, 0.624 g of α-TCP, and 0.096 g of SSP was placed into a small dish, 0.280 ml of water was added, and the powder was rapidly mixed with the water. Then 0.150 ml of the wet cement mixture was added on top of the porous titanium plug in the die. The Freeze-Dried BC sheet was then placed on top of the cement in the die, and an additional 0.150 ml of the wet cement mixture was added on top of the BC sheet. A second porous titanium plug was then placed on top of the Freeze-Dried BC sheet in the die to

create a sandwich structure. The sandwich structure was pressed for 1 hour at 250 MPa. The sample was placed into water at 85°C for 24 hours to facilitate the transformation of α-TCP into hydroxyapatite. The sample was then placed into a hydrothermal reactor with a mixture of PVA (40 wt.%) and DI water (60 wt.%) to infiltrate PVA into the BC layer. The sample was frozen at -78°C and thawed to room temperature to further increase the strength of the hydrogel. The sample was then soaked in a solution containing AMPS, (30 wt.%) cross-linker (MBAA, 60 mM), and heat initiator (potassium persulfate, 0.5 mg ml-1) for 24 hours. The hydrogel was heat cured at 60 °C for 8 hours and the sample was soaked in DI water for at least 24 hours.

For the zinc phosphate cement, approximately 1 g of the liquid was mixed with 2 g of powder for 90 seconds. The addition of the powder into the liquid was carried out slowly, smoothly and carefully with constant stirring. Approximately 0.150 mL of the wet zinc phosphate cement mixture was added on top of the first porous titanium plug in a metal die with an inner diameter of 6 mm. The BC sheet was then placed on top of the cement in the die, and an additional 0.150 mL of the wet cement mixture was added on top of the BC sheet. The second porous titanium plug was then placed on top of the BC sheet in the die to create a sandwich structure. The sandwich structure was pressed for 1 hour at 250 MPa or for 2 minutes by hand. After the cement was completely dry (~2 hours), the sample was placed into water at 22°C for 24 hours to rehydrate the BC. The sample was then placed into a hydrothermal reactor with a mixture of PVA (40 wt.%) and DI water (60 wt.%) to infiltrate PVA into the BC layer. The sample was frozen at -78°C and thawed to room temperature to further increase the strength of the hydrogel. The sample was then soaked in a solution containing AMPS, (30 wt.%) cross-linker (MBAA, 60 mM), and heat initiator (potassium persulfate, 0.5mg ml-1) for 24 hours. The hydrogel was heat cured at 60 °C for 8 hours and the sample was soaked in DI water for at least 24 hours.

For the RelyXTM Luting 2 and RelyXTM Unicem cement, approximately 0.150 mL of the wet RelyXTM Luting 2 or RelyXTM Unicem cement mixture was added on top of the first porous titanium plug in a metal die with an inner diameter of 6 mm. The BC sheet was then placed on top

of the cement in the die, and an additional 0.150 mL of the wet cement mixture was added on top of the BC sheet. The second porous titanium plug was then placed on top of the BC sheet in the die to create a sandwich structure. The sandwich structure was pressed for 1 hour at 250 MPa or for 2 minutes by hand. The sample was placed into water at 22°C for 24 hours to rehydrate the BC. The sample was then placed into a hydrothermal reactor with a mixture of PVA (40 wt.%) and DI water (60 wt.%) to infiltrate PVA into the BC layer. The sample was frozen at -78°C and thawed to room temperature to further increase the strength of the hydrogel. The sample was then soaked in a solution containing AMPS, (30 wt.%) cross-linker (MBAA, 60 mM), and heat initiator (potassium persulfate, 0.5mg ml-1) for 24 hours. The hydrogel was heat cured at 60 °C for 8 hours and the sample was soaked in DI water for at least 24 hours.

For the RelyxTM Ultimate cement, Scotchbond Adhesive was first applied to the porous surfaces of both titanium plugs and both surfaces of a BC sheet. The adhesive was allowed to set for 20 seconds before being blown by air for another 5 seconds. After that, approximately 0.150 mL of the wet RelyXTM Ultimate cement mixture was added on top of the first porous titanium plug in a metal die with an inner diameter of 6 mm. The BC sheet was then placed on top of the cement in the die, and an additional 0.150 mL of the wet cement mixture was added on top of the BC sheet. The second porous titanium plug was then placed on top of the BC sheet in the die to create a sandwich structure. The sandwich structure was pressed for 1 hour at 250 MPa or for 2 minutes by hand. The sample was placed into water at 22°C the rehydrate the BC. The sample was then placed into a hydrothermal reactor with a mixture of PVA (40 wt.%) and DI water (60 wt.%) to infiltrate PVA into the BC layer. The sample was frozen at -78°C and thawed to room temperature to further increase the strength of the hydrogel. The sample was then soaked in a solution containing AMPS, (30 wt.%) cross-linker (MBAA, 60 mM), and heat initiator (potassium persulfate, 0.5mg ml-1) for 24 hours. The hydrogel was heat cured at 60 °C for 8 hours and the sample was soaked in DI water for at least 24 hours.

3.2.6 Preparation of Samples for Single-Plug Shear Testing

For preparing the pig cartilage samples used for the shear test, the pig knee was first clamped on a bench vise. An osteochondral autograft transfer system (OATS) tool was used harvest the osteochondral plug from the pig knee. The OATS donor harvester was positioned on the pig knee surface and tamped approximately 15 mm into the surface. The handle was rotated to harvest the plug and withdrawn. The pig plug was extruded out by the core extruder. The pig plug was cut to make the bone region 8 mm in length

Preparation of all hydrogel samples started with cutting the freeze-dried BC. The freeze-dried BC was placed on that to avoid the direct contact with the laser cutter. Another metal plate is placed on the edge of the BC to ensure the BC stay in its place. The BC was cut in the shape of an octagon with an inner diameter of D mm and 8 legs which has leg lengths of L mm and widths of W=0.383D. The sample was labeled as BC-D-L after cutting. The 8-piece star shape (BC-D-L) was generated by MATLAB and loaded into adobe illustrator. For example, the 3 layers BC shear test sample was fabricated with 3 pieces of BC-6.5-2 from top to bottom. The following cutting settings were used: Speed = 100%, Power = 20%, and Frequency = 100. After cutting, the BC was removed and placed in petri dish.

For adhering three pieces BC to the shear test rod with one layer of cement and a clamp, a stainless-steel test rod was machined to have a top section with a diameter of 5.7 mm and a height of 2 mm, and a bottom section with a diameter of 17 mm and a height of 13 mm. The three pieces of cut BC were placed in an alignment fixture. Scotchbond Universal Adhesive was applied to the layer of the BC in contact with the rod and the top surface of the rod. The adhesive was allowed to set for 20 seconds before being blown by air for another 5 seconds. About 0.15 g RelyX Ultimate Cement was then applied to same surfaces coated with the Scotchbond Universal Adhesive. The rod was pressed into the BC layers and then into the ring clamp. The cement was cured for 1 h. The sample was heated in an oven at 90°C for 10 min to shrink the clamp. The sample was then soaked in DI water for 1 hr in a centrifuge tube.

For creating the sample without the cement, the same procedure was followed as above but no adhesive or cement was applied to the BC or the rod. For creating samples with three layers of cement, additional adhesive and cement was applied as described above between each layer of BC, in addition to between the BC and the rod. For testing samples with 2 layers of BC, the top diameter of the rod was 5.8 mm instead of 5.7 mm, and the size of the cut BC layers were BC-6.5-2 and BC-6.5-2. For testing samples with 6 layers of BC, the top diameter of the rod was 5.2 mm, and the size of the cut BC layers were 3 pieces of BC-6.5-2.25 and 3 pieces of BC-6.5-2.

After attachment of BC to the metal rod, all hydrogel samples were made by infiltrating PVA and PAMPS into the BC. For infiltration of PVA, the rehydrated sample was placed in a hydrothermal bomb with 40% PVA and 60% DI water. The hydrothermal bomb was heated at 120 ℃ for 24 h to infiltrate PVA into the BC layers. After 24 h, the hydrothermal bomb was removed from the oven and opened while it was hot. The sample was taken out from the bomb and the extra PVA around the sample was manually removed. The sample was placed into a -80 ℃ freezer and taken out from the freezer after 30 minutes. The sample was thawed to room temperature before the next step, infiltration of PAMPS. The thawed sample was put into a 30% AMPS (2-acrylamido-2-methylpropanesulfonic acid) solution with 9 mg/mL MBAA crosslinker, 5 mg/mL I2959 and 0.5 mg/mL KPS for 24 h (all fully dissolved). The sample was taken out and cured with UV for 15 minutes. It was transferred to an air-tight centrifuge tube and placed into a 60℃ oven for 8 h for heat curing. After curing, the implant was placed in PBS for rehydration.

3.2.6 Shear Test

Shear testing was performed on a 830LE63 Axial Torsion Test Machine equipped with a 100 lb load cell. Each test was performed in customized shear test fixtures. Fixture 1 (see Figure 7) was used for shear testing of samples in a plug-to-plug configuration. The plugs were placed in the fixture so that the interface between the plugs was centered in the gap between the L-shaped metal plates that make up the fixture. For shearing of cartilage or hydrogel on metal samples, the sample was secured in a cylindrical hole in the left side of fixture 2 (see Figure S2). The hole size was 6

mm for the pig plug and 7 mm for the hydrogel samples. Spacers were added underneath the samples to precisely align the shear plane to the cartilage-bone or hydrogel-metal interface. The right side of the fixture was machined to have a complementary half-cylinder that was used to push the hydrogel or cartilage off of their substrates. The diameter of the right half-cylinder matched that of the left side (either 6 or 7 mm). Rubber was placed between the sample and the right shear fixture to apply pressure during the shear test in order to minimize cleavage and peeling. A crosshead displacement rate of 2 mm min-1 was used for all the measurements.

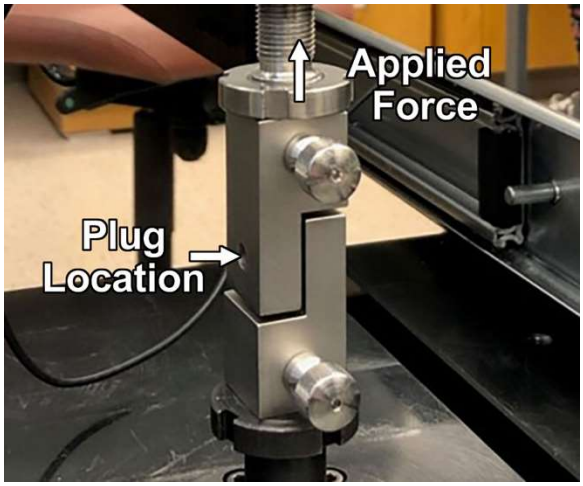

Figure 7. Image of shear test fixture 1, used for shear testing of the plug-to-plug samples shown in Figure 1A and B.

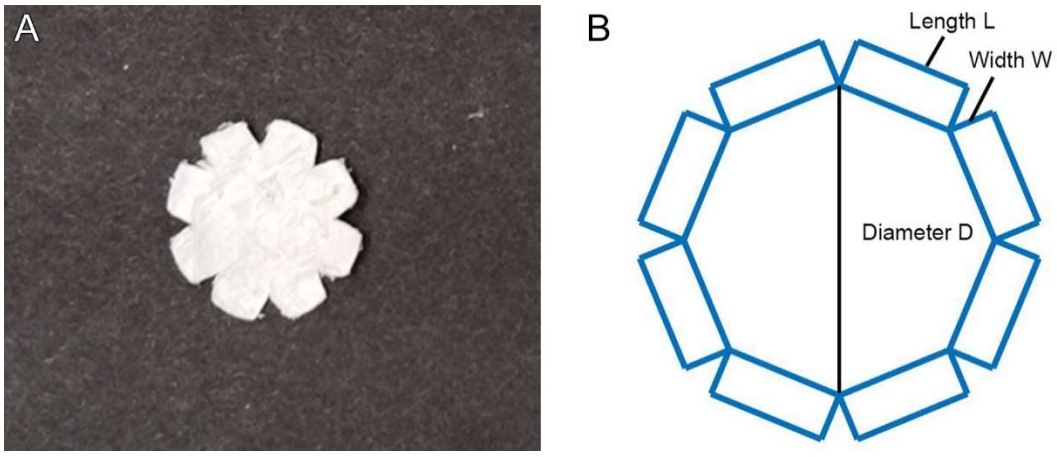

Figure 8. (A) Example of BC sheet cut with legs for wrapping over the edge of the metal rod. (B) Diagram denoting the diameter D, length L, and width W describing the dimensions of the sheet.

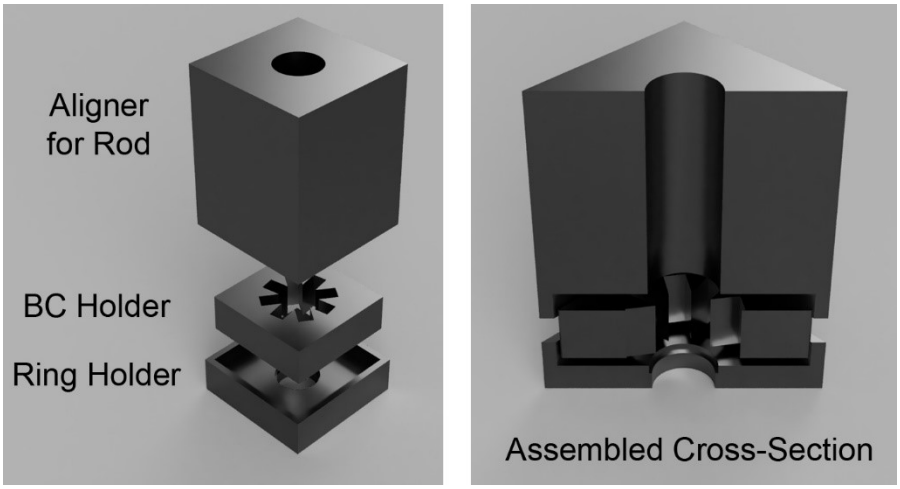

Figure 9. Rendering of the fixture used for aligning the rod, cut BC, and ring clamp.

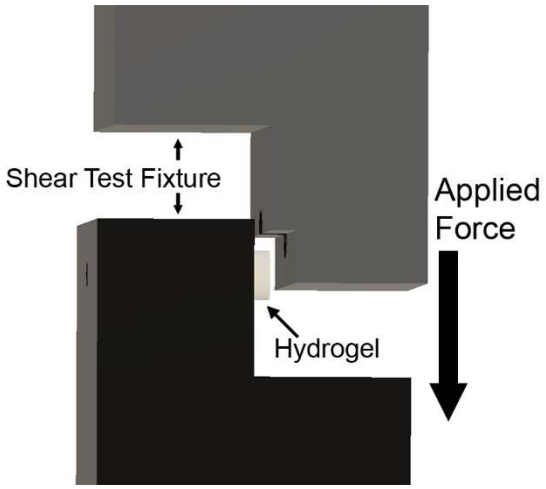

Figure 10. Schematic of shear test fixture 2, used for shearing cartilage off bone and the clamped hydrogel off from metal rods.

3.3 Results and Discussion

3.3.1 Testing of Cements in a Plug-to-Plug Orientation

Following upon our previous efforts to increase the shear strength of hydrogel attachment with the NEST method, we tested the shear strength of other cements besides the α-TCP cement described previously.[71] The shear strength of alternative cements was first tested between two titanium plugs topped with a 1-mm-thick layer of 3D printed struts with a porosity of 70%. In the case of the α-TCP cement used previously, the sandwich structure was pressed together in a die at 250 MPa to reduce the porosity of the cement.[71] The other plugs were pressed together by hand. An example image of a sample made with a RelyX Ultimate cement before and after shear testing is shown in Figure 11A.

Shear testing was performed on a Test Resources 830LE63 Axial Torsion Test Machine equipped with a 100 lb. load cell and a custom-made shear testing fixture (see Figure 7). Note that in this "plug-to-plug" sample configuration, the shear force is applied evenly over the entire area of attachment. As shown in Figure 11C, all the alternative cements that were tested exhibited higher

shear strengths than α-TCP cement for bonding two porous titanium plugs. All sample fracture surfaces indicated cohesive failure similar to the RelyXTM Ultimate cement sample shown in Figure 11A.

Next, we tested the attachment of the same cements to the BC-PVA-PAMPS hydrogel in a sandwich structure. The sample was prepared by cementing a BC sheet between the titanium plugs. The sample was either pressed together by hand for 2 minutes, or for 1 hour at 250 MPa. PVA and PAMPS were then infiltrated into the BC to create a hydrogel. An image of a sample prepared with the RelyXTM Ultimate cement is shown in Figure 11B.

In contrast to the results for bonding porous titanium, none of the alternative cements pressed by hand increased the shear strength of hydrogel attachment relative to α-TCP pressed at 250 MPa (Figure 11D). We hypothesized the relatively low strength of attachment was due to a lack of penetration of the cements into the nanofibrous BC matrix. This hypothesis was tested by pressing the other cements at 250 MPa in the wet state prior to curing, similar to the case of α-TCP. The application of pressure increased the shear strength for each alternative cement. However, none of the shear strengths were significantly greater than that achieved with α-TCP. It was surprising that the RelyXTM Ultimate cement, for example, exhibited a shear strength 6.9 times higher than α-TCP for bonding porous titanium, but did not significantly increase the shear strength for bonding the hydrogel.

Scanning electron microscopy (SEM) images of the fracture surfaces for the porous titanium (Figure 11E) and hydrogel (Figure 11F) samples were taken to determine the reason for the lower shear strength of the hydrogel samples. For the porous titanium sample (Figure 11E), a number of smooth fracture surfaces are visible in the SEM image, indicating failure was due to the fracture of the cement. However, in the case of the hydrogel sample, no smooth fracture surfaces are visible for the cement. Instead, the SEM image shows the nanofibrous surface of the BC. No fiber pull-out or fiber fracture is readily apparent in the image. Instead, it appears as though failure was due to delamination of the layers of nanofibers in the BC.

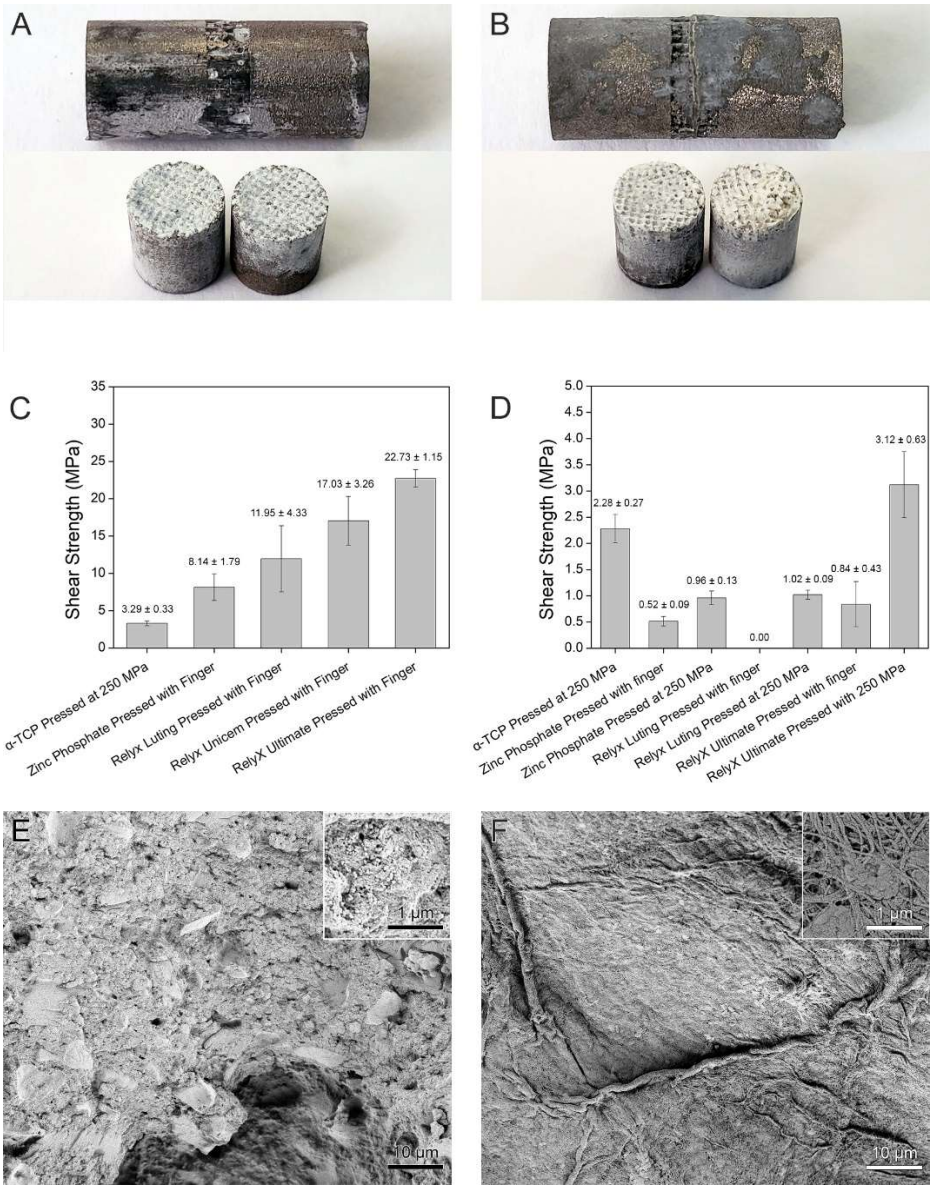

Figure 11. (A) Image of two titanium plugs bonded with RelyX Ultimate cement before and after shear testing. (B) Image of two titanium plugs bonded to BC-PVA-PAMPS hydrogel with RelyX Ultimate cement before and after shear testing. (C) Adhesive shear strengths of two titanium plugs bonded with various cements. (D) Adhesive shear strengths of two titanium plugs bonded to the BC-PVA-PAMPS hydrogel with various cements. (E) SEM image of the fracture surface in (A). (F) SEM image of the fracture surface in (B).

3.3.2 Overcoming the Delamination of the Bacterial Cellulose

Figure 12 shows the layered structure of the BC is readily apparent when imaged by SEM in a direction perpendicular to the sheet. The sample in Figure 12 was prepared by freeze-drying

and cutting the BC. The layered nature of BC has been noted in a number of previous studies.[79-84] It is due to the layer-by-layer construction of the BC film by bacteria at the air-liquid interface. Studies of collagen in cartilage have indicated it also has a layered structure, albeit one in which the layers start by being oriented perpendicular to bone and then curve over to be parallel to the cartilage surface.[85] The structure of collagen layers in cartilage suggests the attachment strength of the BC-PVA-PAMPS hydrogel can be increased if the BC layers are curved over such that the nanofiber sheets in the BC are oriented perpendicular to the direction of shear. A perpendicular orientation of the nanofiber sheets relative to the direction of shear should increase the shear strength because removal of the BC-PVA-PAMPS from the titanium would then require fracture of the BC nanofibers. In contrast, shear-induced fracture of the BC-PVA-PAMPS hydrogel in a direction parallel to the surface of the BC sheets involves delamination of the layers and breaking relatively few nanofibers (see Figure 11F). This situation is similar to the case of fiber reinforced polymer composites, which are 25-40 times stronger in the plane of the fiber sheets than out of plane.[86] Indeed, the highest shear strength achieved in Figure 11D (3.12 MPa) is approximately 6 times lower than the tensile strength of the hydrogel, a test which involves nanofiber fracture.[87]

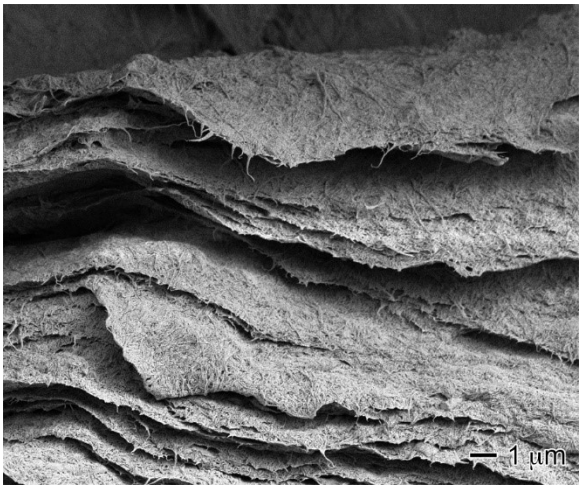

Figure 12. SEM image of a cross-section of a bacterial cellulose sheet.

Our strategy for orienting the BC nanofibers in the hydrogel perpendicular to the direction of shear is to wrap the hydrogel around the periphery of the metal plug and secure the hydrogel in place with a shape memory alloy clamp. The clamps were received in their temporary (deformed) state. Upon heating, the clamps shrink back to their permanent shape. The shape memory alloy clamp was chosen over other potential clamps due its small size and high clamping force. For the ring clamps used here, the supplied diameter was 6.4 mm, the ring thickness was 0.27 mm, and the ring height was 1 mm. Upon heating, this clamp supplies a nominal clamping force of 300 N (67 lbf). A NiTiNb shape memory alloy (Alloy H from Intrinsic Devices, Inc.) was chosen for the clamp due to its convenient operating temperature and large temperature range over which the clamping force is maintained. For this alloy, the full clamping force is obtained at 165 °C and is maintained from -65°C to +300°C. The NiTiNb alloy is also more corrosion resistant than NiTi, which is used currently in implants, suggesting that it is biocompatible.[88-90]

A brief overview of how the hydrogel is attached to a metal base is illustrated in Figure 13. Freeze-dried BC sheets were cut into octagonal shapes with 8 legs that can be bent over the edges of the implant (see Figure 8 for an example). This shape was designed to minimize excess BC that would otherwise be folded up on the sides of the cylinder. The pieces of cut BC were placed into a fixture (see Figure 9) that facilitated centering and alignment of the ring clamp with the pieces of BC and the metal rod, which in this case was stainless steel. The metal rod was pushed down through the fixture so that the ring pushed the pieces of BC onto the metal rod. The sample was subsequently heated in an oven at 90 °C to initiate clamping (which starts at a temperature of 50 °C). The part was then heated in a hydrothermal bomb at 120 °C for 24 with PVA to infiltrate the polymer into the BC. Finally, the BC-PVA was infiltrated with PAMPS by soaking in a solution of 30% AMPS (2-acrylamido-2-methylpropanesulfonic acid) with 9 mg/mL MBAA crosslinker, 5 mg/mL I2959 and 0.5 mg/mL KPS for 24 h. The sample was cured with UV for 15 minutes, followed by curing at 60°C for 8 h for heat curing.

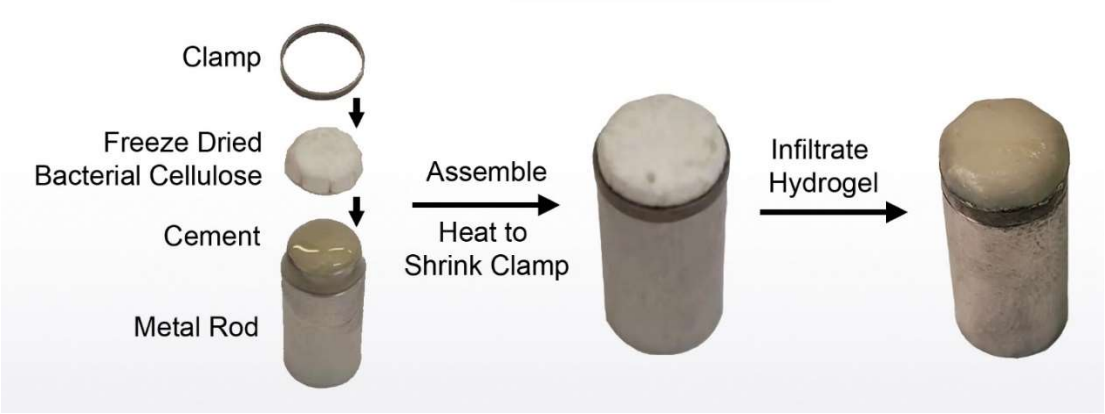

Figure 13. Overview of the novel method of attaching a hydrogel to a metallic plug with a shape memory alloy clamp.

Having the right distance between the inner diameter of the ring and the outer diameter of the rod was critical to achieving a high clamping force without breaking the BC. For example, for attachment of three pieces of BC to the metal rod, the outer diameter of the rod was 5.7 mm and the inner diameter of the ring was 6.4 mm, leaving 0.35 mm for the three pieces of BC. Each piece of frieze-dried BC was 0.14 ± 0.03 mm, for a total thickness of 0.42 mm, so the BC had to be compressed by approximately 6% per sheet to slide the ring into place. This compression of the BC allowed the ring to build up clamping force as it was heated. If the ring shrank with no resistance from the BC, then there would be no clamping force. If the space between the rod and metal rod was reduced below 0.35 mm, then the BC fractured as the ring was slid over the BC.

We next sought to directly compare the strength of attachment of the hydrogel to the rod to the strength of attachment of cartilage to bone. This was not possible with the plug-to-plug configuration used for the samples in Figure 11 because there is no way to attach a rod to the surface of cartilage with the same strength as the osteochondral junction. Previous tests of the shear strength of the osteochondral junction have used an L-shaped jig that pulls a square-shaped piece of cartilage off bone while constraining the movement of cartilage in a direction perpendicular to the shear plane.[66, 91] To perform a similar test with our cylindrical specimens, we fabricated the shear test

fixture shown in Figure 10. The specimen was secured in a cylindrical hole in the left side of the fixture. The right side of the fixture was machined to have a complementary half-cylinder that was used to push the hydrogel or cartilage off of their substrates. A crosshead displacement rate of 2 mm min^{-1} was used for all the measurements (same rate as for the previous measurements in a plug-to-plug configuration). We note that while fixture 1 in Figure 7 applies the shear force relatively evenly over a given interface, fixture 2 in Figure 10 focuses the applied force on one edge of the rod. This difference in the manner in which the force is applied is expected to lead to a lower observed shear force relative to fixture 1, especially since fixture 2 can potentially cause cleavage and peel stresses.

Figure 4A shows the results for shear testing samples with shear test fixture 2. Pig cartilage had an average shear strength of 1.16 ± 0.35 MPa. Figure 4B shows the cartilage was sheared cleanly off of the underlying bone in this sample. The lower shear strength of cartilage measured with fixture 2 relative to previous work (2.45 ± 0.85 to 2.6 ± 0.58 MPa) may be due to the cylindrical shape of our specimens, which may concentrate stress over a smaller area at the edge of the specimen compared to the rectangular specimens tested previously.[66, 91] We attempted to avoid stress concentration by shearing the sample with a matching cylindrical surface, but this attempt may not have been entirely successful. There may have also been some peeling and/or cleavage in addition to shear due to imperfect alignment or imperfect constraining of the cartilage from moving out of the shear plane. Although we obtain a lower number for the shear strength of cartilage than previous authors, the fact that we perform a direct comparison with hydrogel samples in the same fixture should still provide a valid answer to the question of whether we have achieved cartilage-equivalent shear strength. Further, we note that the standard deviation of our cartilage shear strength measurements (± 0.35 MPa) is lower than those obtained previously (>0.85 MPa), indicating our measurement method is at least as precise as previous efforts.

By using a shape memory clamp without cement, a hydrogel sample with three layers of BC was attached to the metal rod with a shear strength of 0.98 MPa (Figure 4A). We note that this

result is well-within the error of the average shear strength for pig cartilage, indicated cartilage-equivalent shear strength can be achieved with the clamp alone. Figure 14C shows the attachment failed due to the hydrogel being pulled out of the clamp. The hydrogel is also dented where it was contacted by the shear fixture, but this is difficult to observe in Figure 14C.

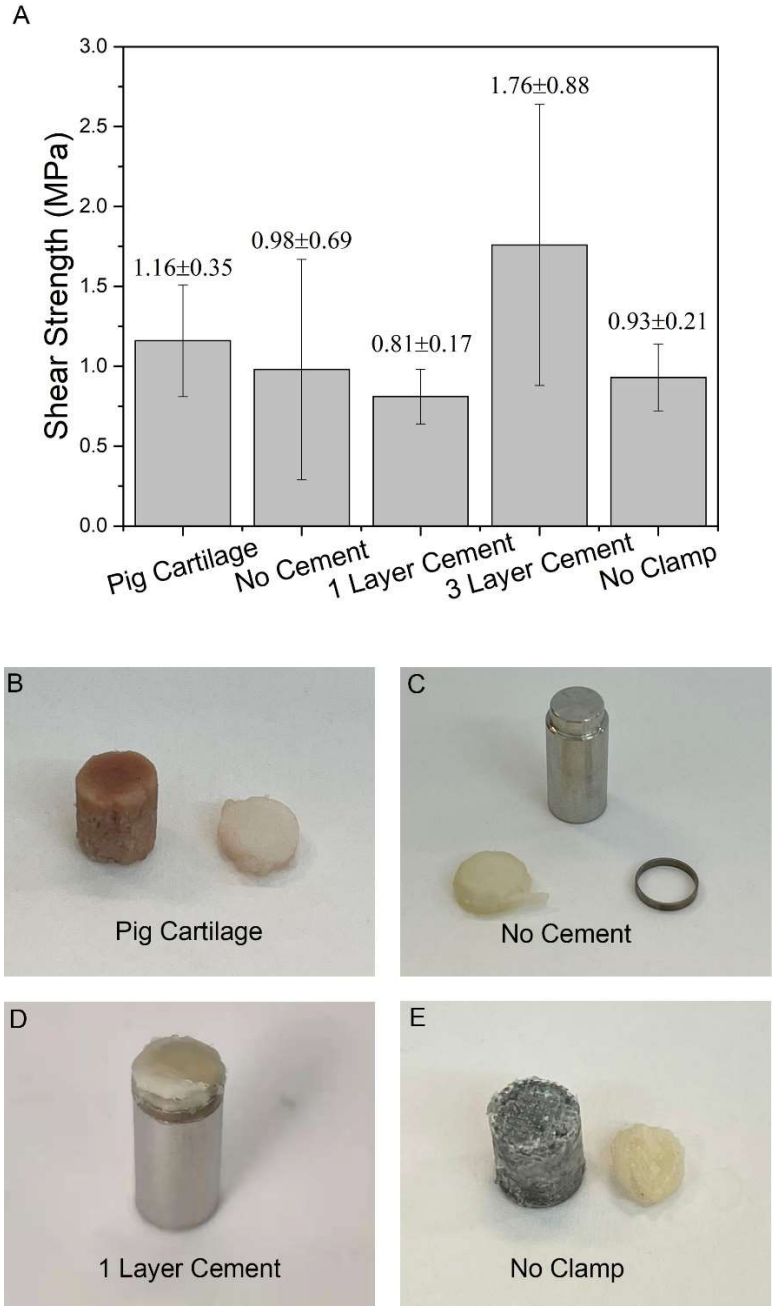

Figure 14. (A) Results for shear testing with the fixture shown in Figure 10. N=3 for all measurements. (B-E) Shear testing samples after failure.

Addition of 1 layer of cement between the hydrogel and the metal rod resulted in an attachment strength of 0.81 ± 0.17 MPa. This result indicates the addition of cement underneath the first layer of BC does not increase the strength of attachment beyond what was achieved with the clamp alone. However, the addition of cement did change the failure mode. The hydrogel fractured rather than pulled out of the clamp (see Figure 14D). The failure mode in 14D is preferable in the context of a hydrogel-capped implant because even though the hydrogel fractured it is still covering the metal and not exposing an opposing cartilage surface to wear by a metallic surface, for which the coefficient of friction is higher than that of the hydrogel.[87]

Next, we made a sample with 3 layers of cement, one layer beneath each of the three BC layers. In this case the average shear strength increased to 1.76 ± 0.88 MPa. This average shear strength exceeds that measured for the pig cartilage samples, but the standard deviation makes the difference in measurements not statistically significant. The addition of cement in between the layers may have increased the average strength by creating a layered composite of cement between each of the BC layers that reinforced the hydrogel. The failure mode for this sample was similar to the case of 1 layer of cement.

We attempted to create a sample in which the hydrogel was attached to the surface of the metal rod with only the cement and not the clamp. This sample proved impossible to make because, without the clamp, the hydrogel detached from the metal pin during the PVA infiltration process. Presumably the expansion of the hydrogel during PVA infiltration created a sufficient shear force to detach the hydrogel from the surface of the smooth metal rod. Instead, we attached 3 layers of hydrogel to a porous titanium plug with cement between each layer. This sample was prepared with Rely X Ultimate cement and was pressed at 250 MPa, similar to the best result in Figure 11D. Shear testing of this “no clamp” sample with fixture 2 yielded a shear strength of 0.93 ± 0.21 MPa. Note that this shear strength is 3.4 times lower than the shear strength of 3.12 ± 0.63 measured with

fixture 1, indicating that method of measurement used with fixture 2 leads to a lower observed shear strength for a sample with an identical interface. Figure 14E shows this sample failed cohesively in a similar manner as the cartilage sample.

The way in which the samples made with the shape memory alloy clamp fractured (see for example Figure 14D) suggests that the shear strength of the samples is limited by the tensile force required to fracture the hydrogel that is curved over the edge of the implant. The shear test pushes the hydrogel off of the metal pin, which creates a tensile force on the hydrogel that is clamped around the sides of the pin. This tensile force can either pull the hydrogel out of the clamp (Figure 14C) or cause the hydrogel around the periphery of the pin to fracture (figure1 14D). These results suggest that the shear strength of attachment can be increased by making the hydrogel layer thicker. Figure 15A shows the results testing this hypothesis. As expected, the shear strength of attachment increases as the number of BC layers is increased from two to six. However, none of the differences in the results were statistically significant. Each of these samples had one layer of cement in between the BC layer and the metal pin, and all failed cohesively (see Figure 15B-D).

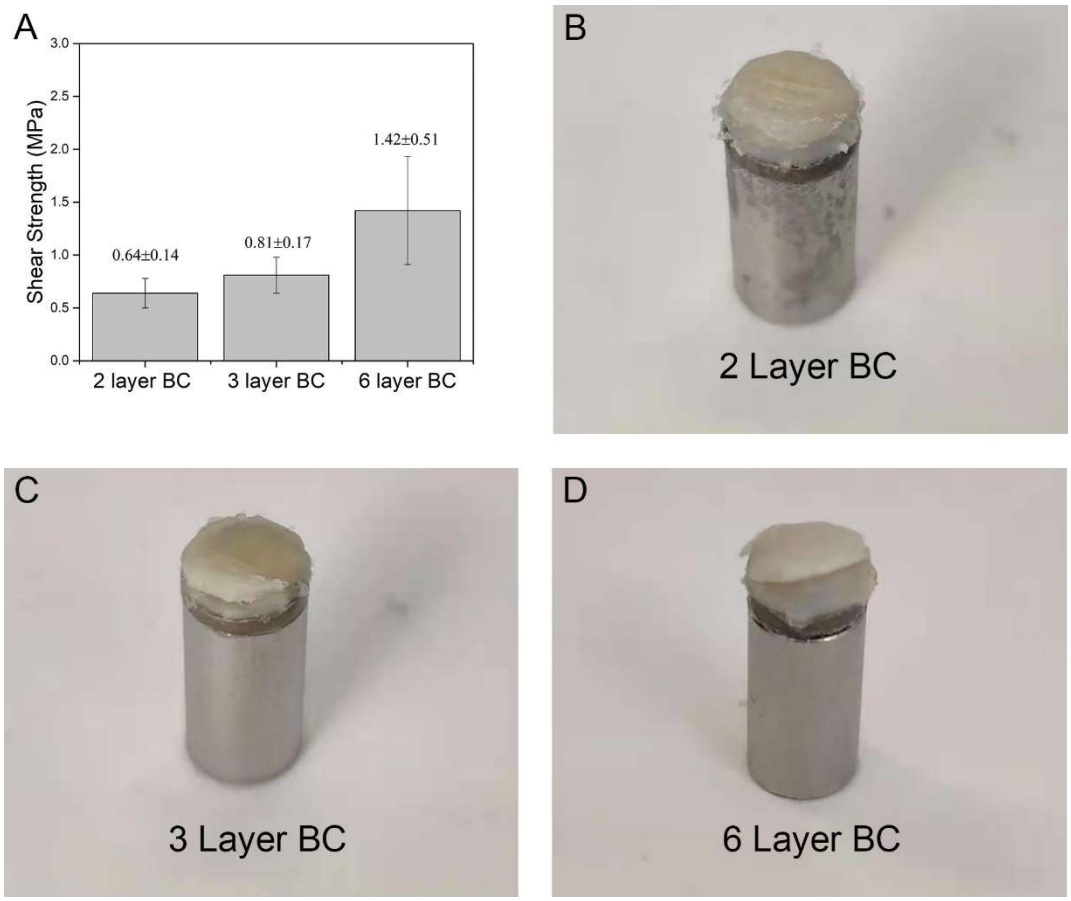

Figure 15. (A) Results for shear testing with the fixture shown in Figure 10. N=3 for all measurements. (B-D) Shear testing samples after failure.

3.3.3 Application of a Clamp to the Creation of Hydrogel-Capped Implants

Shape memory alloy clamps can be produced in a variety of sizes for clamping hydrogels to the surface of implants for repair of osteochondral defects. Figure 16 shows an example of using a larger shape memory alloy clamp to attach the BC-PVA-PAMPS hydrogel to an osteochondral implant with a diameter of 20 mm. In this case five pieces of BC were cut into shapes with 8 octagonal legs that allowed the legs to fold over the edge of the implant. A 0.25-mm-thick coating of commercially pure titanium was applied to the stem of the implant and underneath the base with a plasma spray process in order to improve integration with bone.[92] The top surface of the implant had a radius of curvature of 20 mm to match the native curvature of the femoral condyle.[93] Figure

16B&C show an example of how such an implant would be used to resurface the knee. Figure 16B shows an example of a cartilage defect. The surgeon would drill out a hole over the defect site that is complementary to the shape of the hydrogel-capped implant. The hydrogel-capped implant would then be pressed into the hole to replace the damaged cartilage.

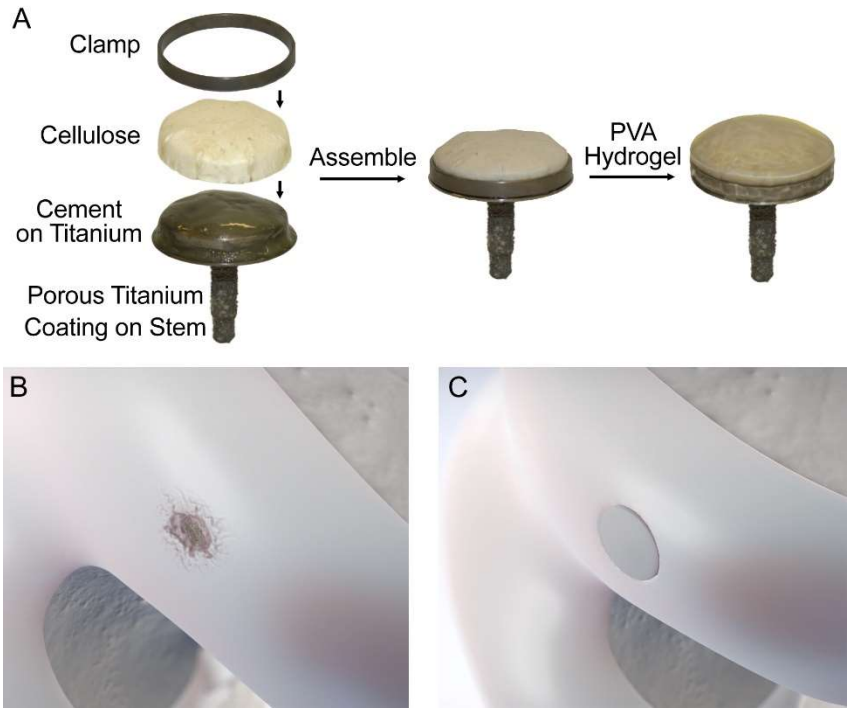

Figure 16. Process for attaching the BC-PVA-PAMPS hydrogel to a titanium implant for treatment of osteochondral defects.

3.4 Conclusion

In conclusion, we have developed a process that enables the attachment of a hydrogel to the surface of an orthopedic implant with the same shear strength as the cartilage-bone interface. Clamping the hydrogel around the periphery of the implant reorients the nanofibers in the BC so that they are perpendicular to the direction of shear. This reorientation increases the average strength of attachment by necessitating fracture of the nanofiber sheets to shear the hydrogel off the metal rod. Without this reorientation, the BC layers delaminate, resulting in a lower shear

strength. The clamping process can be used in conjunction with adhesive cements to prevent the hydrogel from being pulled out of the clamp. The shear strength also increased with the number of BC layers used in the hydrogel, indicating the shear strength is limited by the tensile force required to fracture the hydrogel at the periphery of the implant. This new method of hydrogel attachment can be used to create hydrogel-capped orthopedic implants with joint-facing surfaces that mimic the mechanical and tribological properties of cartilage, and bone-facing surfaces that enable integration with bone for long-term fixation.

4. A Synthetic Hydrogel Composite with a Strength and Wear Resistance Greater than Cartilage

4.1 Introduction

We have previously reported an approach to create a cartilage-equivalent hydrogel by infiltrating a bacterial cellulose (BC) nanofiber network with polyvinyl alcohol (PVA) and poly(2-acrylamido-2-methyl-1-propanesulfonic acid sodium salt) (PAMPS). [94] This hydrogel exhibited a tensile strength of 22.6 MPa and a compression strength of 20 MPa. In comparison, the range of tensile and compression strengths reported for human cartilage are 8.1-40 MPa and 14-59 MPa, respectively.[95-97] Thus, there is still room to improve the strength of hydrogels to be at the higher end of the range of strengths reported for cartilage, or to even exceed cartilage in strength, while having a similar modulus, coefficient of friction, and resistance to wear.

In preparing the BC-PVA-PAMPS hydrogel, we used the freeze-thaw method to gel the PVA-water mixture after infiltration into the BC. This gelation step is necessary to increase the strength of the PVA hydrogel, and to prevent dissolution of the PVA in the following PAMPS infiltration step. The freeze-thaw method is commonly used to create PVA hydrogels with tensile strengths up to 1 MPa.[98-101] The increase in strength upon freezing and thawing the PVA is attributed to crystallization of the PVA chains and phase segregation.[98, 99] The tensile strength of PVA hydrogel can be further increased to 18-20 MPa by drying and annealing the PVA, followed by rehydration.[102-104] We will hereafter often refer to the process of drying, annealing, and rehydration as simply "annealing" to be concise, i.e., an "annealed" hydrogel is one that has gone through the process of drying, annealing, and rehydration. The reason for the higher strength of annealed hydrogels is that the annealing process greatly increases the crystallinity and decreases the water content of PVA relative to the freeze-thaw process. A disadvantage of the annealing process is that it can result in more bubbles and cracks in the PVA, especially as the sample thickness increases or water content increases.

Given the higher tensile strength of annealed PVA relative to freeze-thawed PVA, we decided to test whether changing from a freeze-thaw to annealing process can improve the mechanical strength of a BC-PVA-PAMPS hydrogel while retaining adequate control over the hydrogel shape and defect content. Given the tensile strength of a BC-PVA-PAMPS hydrogel (22.6 MPa), is already similar to the tensile strength of a PVA hydrogel made by annealing (20 MPa), it was not obvious that switching to the annealing process for a BC-reinforced hydrogel would yield further improvements in the mechanical strength. In addition, the presence of BC or PAMPS could potentially interfere with the crystallization of PVA that occurs during the annealing process, thereby hindering the improvement in mechanical strength that occurs as a result of crystallization. It was also not clear whether we could obtain high-quality, bubble-free, crack-free samples after annealing PVA reinforced with BC. Obtaining samples that are as free of defects as possible is necessary to maximizing the mechanical strength of the hydrogel. Finally, it was unclear whether the lower water content of the annealed hydrogel might cause the COF and opposing surface wear to be too high.

This work shows that reinforcement of annealed PVA with BC leads to a 3.2-fold improvement in the tensile strength (from 15.6 to 50.5 MPa) and a 1.7-fold increase in the compressive strength (from 56.7 to 95.4 MPa). The highly crystallized BC-PVA hydrogel that results from annealing is the first hydrogel with a tensile and compressive strength that exceeds that of cartilage. Reinforcement of the PVA with BC essentially eliminated the deformation and bubbles that would otherwise occur during annealing. When tested against cartilage, annealed BC-PVA wore an opposing cartilage surface to the same extent as cartilage and was three times more resistant to wear than cartilage. The COF of BC-PVA against cartilage was equivalent to that of cartilage against cartilage. In contrast to results with freeze-thawed BC-PVA, addition of PAMPS to the annealed BC-PVA decreased the tensile strength of the hydrogel due to a loss of crystallized PVA and an increase in water content. The improved tensile strength of annealed BC-PVA enabled it to attach to a metal base with a shear strength 68% greater than the shear strength of cartilage on

bone. The high strength, high wear resistance, and low COF of annealed BC-PVA make it an excellent material for replacing damaged cartilage.

4.2. Methods

4.2.1 Materials

Bacterial Cellulose (BC) was purchased from Gia Gia Nguyen Co. Ltd. Poly(vinyl alcohol) (PVA) (fully hydrolyzed, molecular weight: 145,000 g mol^{-1}), N,N'-methylenediacrylamide (MBAA, 97.0%), 2-hydroxy-4'-(2-hydroxyethoxy)-2-methylpropiophenone (I2959), potassium persulfate (KPS) and 2-acrylamido-2-methylpropanesulfonic acid sodium salt (AMPS, 50 wt.% solution in water) were purchased from Sigma Aldrich. Phosphate buffered saline (PBS) was purchased from VWR International. Fetal bovine serum (FBS, Canada origin, collected from cattle typically 12-24 months old) was purchased from Corning. Shape memory alloy ring clamps were purchased from Intrinsic Devices.

4.2.2 Fabrication of BC-PVA-PAMPS Hydrogel

BC sheets were pressed to be 0.5 mm thick and placed into a hydrothermal reactor with a mixture of PVA (40 wt.%) and DI water (60 wt.%). The hydrothermal reactor was sealed and heated at 135°C for 24 hours to allow the PVA to diffuse into the voids of BC and form a BC-PVA hydrogel. The BC-PVA hydrogel was removed from the reactor when hot (>85°C). Note the hydrothermal reactor was pressurized with hot steam and is a burn hazard, so personal protective equipment including lab coat, heat resistant gloves and full-coverage face shields should be used when opening the reactor. The residual PVA solution was removed by scrapping the surface of the BC-PVA samples with a metal spatula. The samples were frozen at -78°C for 30 minutes and thawed at room temperature to physically crosslink the PVA network. The BC-PVA hydrogel was then soaked in a solution of AMPS (30 wt.%), MBAA (60 mM), I2959 (50 mM) and KPS (0.5 mg mL-1) for 24 hours. The hydrogel was cured with a UV transilluminator (VWR International) for 15 minutes on each side, and further cured in an oven at 60°C for 8 hours to ensure even and

complete curing. The resulting BC-PVA-PAMPS hydrogel was stored in PBS for at least 24 hours before further characterization.

4.2.3 Fabrication of Annealed BC

BC sheets were pressed to be 0.5 mm thick. The BC sheets were then placed into a 90°C oven for 24 hours before being annealed at 90°C for an additional hour. The resulting annealed BC was cut into the desired shape and stored in 0.15 M PBS for at least 24 hours.

4.2.4 Fabrication of PVA Hydrogel

To fabricate the PVA hydrogel, a slurry of PVA (40 wt.%) and DI water (60 wt.%) were mixed in a metal baking pan (diameter: 203.2 mm) and heated at 120°C for 20 minutes in an autoclave sterilizer. To make annealed PVA hydrogel, the resulting hydrogel was dried in an oven at 90°C for 24 hours before being annealed at 90°C, 120°C or 140°C for an additional hour. To make freeze-thawed PVA hydrogel, the autoclaved hydrogel was frozen at -80°C for 30 minutes and thawed at 23°C for 30 minutes. The resulting PVA hydrogel was cut into the desired shape and stored in 0.15 M PBS for at least 24 hours before tests.

4.2.5 Fabrication of Annealed BC-40 wt.% PVA Hydrogel

BC sheets were pressed to be 0.5 mm thick and placed into a hydrothermal reactor with a mixture of PVA (40 wt.%) and DI water (60 wt.%). The hydrothermal reactor was sealed and heated at 135°C for 24 hours to allow the PVA to diffuse into the voids of BC and form a BC-PVA hydrogel. The BC-PVA hydrogel was removed from the reactor when hot (>85°C). Note the hydrothermal reactor was pressurized with hot steam and created a burn hazard, so personal protective equipment including lab coat, heat resistant gloves and full-coverage face shields should be used when opening the reactor. The residual PVA solution was removed by scrapping the surface of the BC-PVA samples with a metal spatula. The samples were dried in an oven at 90°C for 24 hours before annealing at 90°C, 120°C or 140°C for an additional hour. The resulting annealed BC-PVA hydrogel was cut into a desired shape and stored in 0.15 M PBS for at least 24 hours before tests.

4.2.6 Fabrication of Annealed BC-10 wt.% PVA Hydrogel

BC sheets were pressed to be 0.5 mm thick and placed into a baking pan (15.6 cm × 8.6 cm × 4.2 cm). Approximately 30 mL of 10 wt.% PVA solution was added to the baking pan. The baking pan was placed in an oven at 90°C for 24 hours and annealed at 90°C for an additional hour. The resulting annealed BC-PVA hydrogel was cut into the desired shape and stored in 0.15 M PBS for at least 24 hours.

4.2.7 Fabrication of Annealed BC-PVA-PAMPS Hydrogel

BC sheets were pressed to be 0.5 mm thick and placed into a hydrothermal reactor with a mixture of PVA (40 wt.%) and DI water (60 wt.%). The hydrothermal reactor was sealed and heated at 120°C for 24 hours to allow the PVA to diffuse into the voids of BC and form a BC-PVA hydrogel. The BC-PVA hydrogel was removed from the reactor when hot (>85°C). Note the hydrothermal reactor was pressurized with hot steam and created a burn hazard, so personal protective equipment including a lab coat, heat resistant gloves and full-coverage face shields should be used when opening the reactor. The residual PVA solution was removed by scrapping the surface of the BC-PVA samples with a metal spatula. The samples were dried in an oven at 90°C for 24 hours before being annealing at 90°C, 120°C or 140°C for an additional hour. The annealed BC-PVA hydrogel was then soaked in a solution of AMPS (30 wt.%), MBAA (60 mM), I2959 (50 mM) and KPS (0.5 mg mL-1) for 24 hours. The hydrogel was cured with a UV transilluminator (VWR International) for 15 minutes on each side, and further cured in an oven at 60°C for 8 hours to ensure even and complete curing. The resulting annealed BC-PVA-PAMPS hydrogel was stored in PBS for at least 24 hours before further characterization.

4.2.8 Fabrication of Hydrogel on the Stainless-Steel Pin

Preparation of all hydrogel samples started with cutting the freeze-dried BC. The BC is cut in the shape of an octagon with diameter D and 8 legs which has leg length of L and widths of W=0.383D (See **Figure 8** for example). The sample was labeled as BC-D-L after cutting. The 8-piece star shape (BC-D-L) was generated by MATLAB and loaded into Adobe Illustrator. In Adobe

Illustrator the stroke of the shape is changed to 0.0001 pt to ensure accurate cutting. The file is sent to the laser cutter (Epilog Fusion M2) by using the print function and the laser cutter was selected as the printer. The vector process is used, with 100% speed, 20% power and 100% Frequency. These setting can be changed in the printer preference tab. For cutting the BC, a clean metal plate was placed on the bed of the laser cutter, and the freeze-dried BC was placed on onto the metal plate. Another metal plate is placed onto the edge of the BC to ensure the BC stays in place. The focus was adjusted and the shape was cut by the machine. After cutting, the BC was collected and stored in a petri dish for future use.

For preparing the shear test samples, six pieces of BC were adhered to the stainless-steel rod with one layer of cement and a clamp. On overview of the assembly method is shown in **Figure 13**. A stainless-steel test rod was machined to have a top section with a diameter of 5.2 mm and a height of 2 mm, and a bottom section with a diameter of 6.75 mm and a height of 13 mm. Three pieces of BC-6.5-2.25 and 3 pieces of BC-6.5-2 were placed in an alignment fixture. Scotchbond Universal Adhesive was applied to the layer of the BC in contact with the rod and the top surface of the rod. The adhesive was allowed to set for 20 seconds before being blown by air for another 5 seconds. About 0.15 g of RelyX Ultimate Cement was then applied to the same surfaces coated with the Scotchbond Universal Adhesive. The rod was pressed into the BC layers and then into a shape memory alloy ring clamp. The cement was cured for 1 h. The sample was heated in an oven at 175°C for 10 min to shrink the clamp. The sample was then soaked in DI water for 1 hr in a centrifuge tube before future use. The sample with BC on top then went through the specific hydrogel fabrication process.

Compression test samples were fabricated using the stainless-steel rod and a clamp, but without cement. Wear test samples were fabricated with a stainless-steel rod 5.7 mm in diameter and 38 mm in height, 3 pieces of BC-6.5-2, and the shape memory alloy ring, but without cement.

4.2.9 Monotonic Tensile and Compression Tests

Monotonic tensile tests were carried out on an Instron 1321 (Instron, Norwood, MA, USA) and a TestResources 830 (TestResources, Shakopee, MN, USA) load frame at a rate of 0.25 mm s^{-1}. The finished hydrogel was cut into an ASTM D638-14 Type V shape with a titanium hollow punch for testing (see **Figure 20** for examples). The dimensions of the samples were measured with a caliper before testing. The ultimate tensile strength (UTS) was the maximum stress measured before fracture in the case of the BC-PVA samples, or the maximum compressive stress at 80% strain for the PVA samples. The tensile modulus was taken as the slope of the stress-strain curve at a stress of 1 MPa for comparison with previous studies of human cartilage.[96]

The compressive properties of all samples were measured with an axial Torsion System (TestResources 830LE63). Cylindrical samples of PVA were cut out of films of hydrogel samples with a hollow steel punch with a diameter of 4 mm. BC-PVA samples were attached to a metal pin for compression testing in order to have a sample that was sufficiently thick. The dimensions of the samples were measured with a caliper before testing. The compressive properties were measured with a strain rate of 0.05 s^{-1}. The ultimate compressive strength was taken as the maximum stress measured before fracture. The compressive modulus was derived as the slope of the stress-strain curve at a stress of 0.4 MPa for comparison with previous studies of human cartilage.[97]

4.2.10 Differential Scanning Calorimetry

Differential scanning calorimetry (DSC) was performed on hydrogel samples to determine the PVA crystallinity. The tests were completed on a TA TGA550. In a typical experiment, a hydrogel sample of approximately 5 mg was placed in an aluminum pan and heated at a scanning rate of 10 °C/min under a nitrogen gas flow from 25°C to 300°C. Typical thermograms for PVA, BC-PVA and BC-PVA-PAMPS hydrogels are shown in **Figure 17**.

The calculation for how much of the PVA was crystallized, i.e., the degree of crystallinity, was adopted from Hassan et al.[105] After the DSC thermogram was acquired, the area under the melting peak over the range 140-220°C (as shown in **Figure 18**) was integrated to obtain a value

with units of $J \cdot °C \cdot S^{-1} \cdot g^{-1}$. This number was then divided by the heating rate (0.17 $°C \cdot S^{-1}$) to obtain ΔH ($J \cdot g^{-1}$). The crystallinity of PVA was then calculated by dividing ΔH for the sample by the heat required for melting a 100% crystalline PVA sample, $\Delta H_c = 138.6\ J/g$, and the weight fraction of PVA in the sample, w_{PVA},

$$\chi_{PVA} = \frac{\Delta H}{w_{PVA} \times \Delta H_c}$$

where χ_{PVA} is the crystallinity of the PVA.

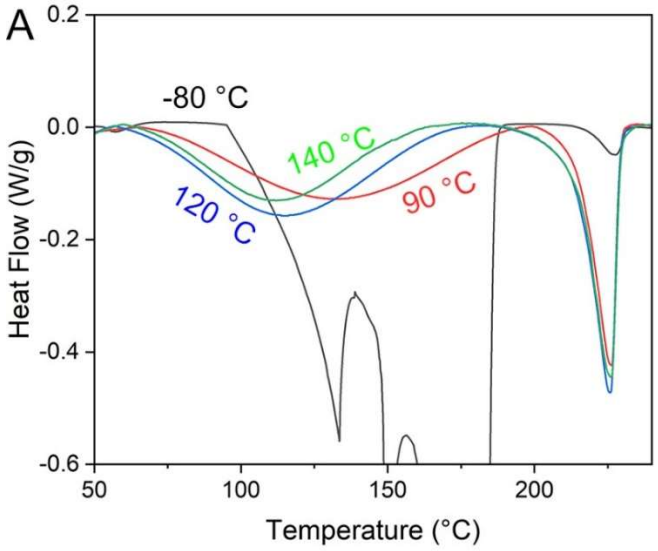
A
-80 °C
140 °C
90 °C
120 °C
Heat Flow (W/g)
Temperature (°C)

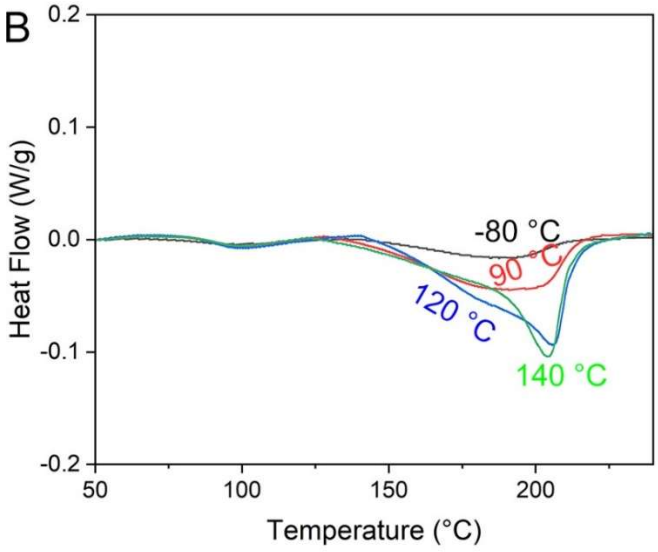
B
-80 °C
90 °C
120 °C
140 °C
Heat Flow (W/g)
Temperature (°C)

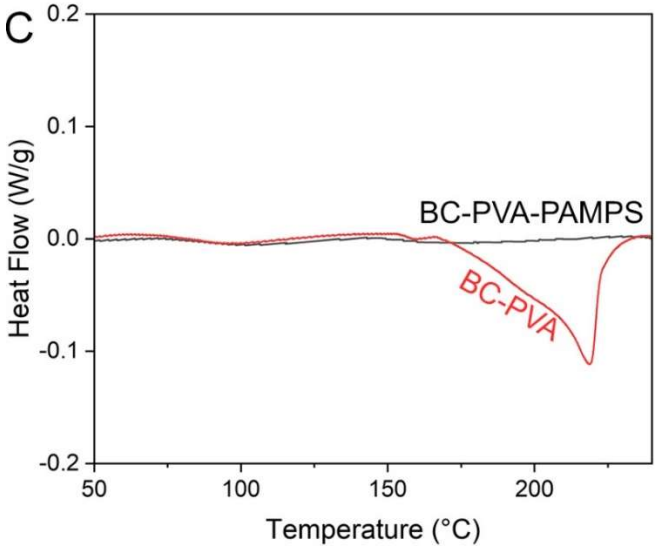
C
BC-PVA-PAMPS
BC-PVA
Heat Flow (W/g)
Temperature (°C)

Figure 17. DSC thermograms for (A) freeze-thawed and annealed PVA hydrogels, (B) freeze-thawed and annealed BC-PVA hydrogels (B), (C) annealed BC-PVA and BC-PVA-PAMPS. The concentration of the AMPS solution to make the BC-PVA-PAMPS was 10 wt%.

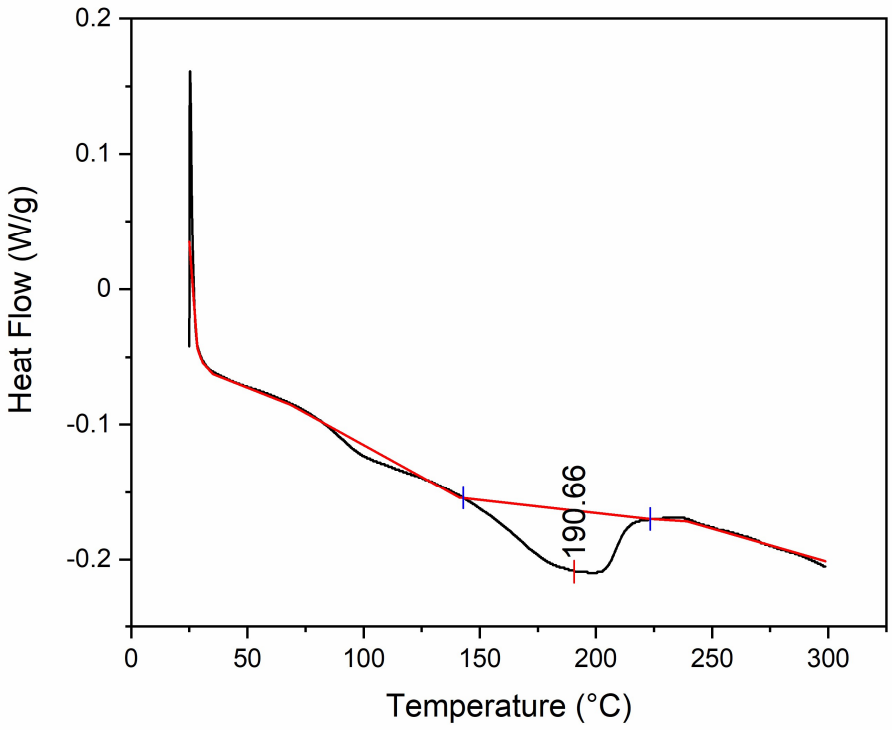

Figure 18. DSC thermogram for an annealed BC-PVA hydrogel sample demonstrating how the peak was integrated.

4.2.11 Measurement of Solid Weight Fraction

The weight of approximately 1 g of hydrated hydrogel was measured before drying at 90°C for 24 hours. The weight of the dehydrated sample was then measured. The weight after dehydration was divided by the weight before dehydration to determine the solid weight fraction of the hydrogel sample.

4.2.12 Wear Testing

The wear resistance of the hydrogels and porcine cartilage samples were determined with the pin-on-disk setup shown in **Figure 19**. The pin-on-disk method was used with an Anton Paar

Rheometer (MR302) and a tribology accessory (SCF7). Cartilage samples were harvested from pig femurs with an osteochondral autograft transfer system (Arthrex). The femurs were purchased from a local grocery store and frozen at -78°C before harvesting the samples. Hydrogel samples were polished with #600, #800, #1000, #1200, #1500, #2000, #2500 and #3000 sandpapers to make them smooth prior to testing. A hydrogel pin was fabricated by using the method described in section 2.8. A disk of hydrogel or porcine cartilage with a diameter of 12.7 mm was adhered with cyanoacrylate glue (Gorilla Glue Company) to the sample holder. The testing parameters were as follows: 1,000,000 rotations; angular speed: 319 rounds per minute (maximum linear velocity: 100 mm s-1); normal force: 28.26 N (pressure: 1 MPa). A pressure of 1 MPa was applied to each sample for 5 minutes before tests started. The tests were performed in FBS. FBS is often used during wear tests to mimic the lubrication provided by synovial fluid[106-108].

After the wear test, the samples were rehydrated in FBS for 24 hours to allow the gels to recover from the applied pressure before the wear depth was measured with a High-Resolution X-ray Computed Tomography (Micro-CT) Scanner (Nikon XTH 225 ST). A 3D model of the reconstructed Micro-CT images was rendered with Avizo 9 Lite. To measure the wear depth, a slice of the 3D model was taken in the middle of the wear mark. The wear depths were measured from the images of the middle slices with ImageJ.

For calculating the COF, we determined the total friction force (F) from the torque (T) and the radius of the pin in the pin-on-disk setup (R):[109]

$$F = \frac{3T}{2R}$$

The *COF* can then be calculated by:

$$COF = \frac{F}{F_N}$$

Here F_N is the normal force (28.26 N). The linear velocity (v) was calculated by:

$$v = \omega R$$

where ω was the angular speed of the pin.

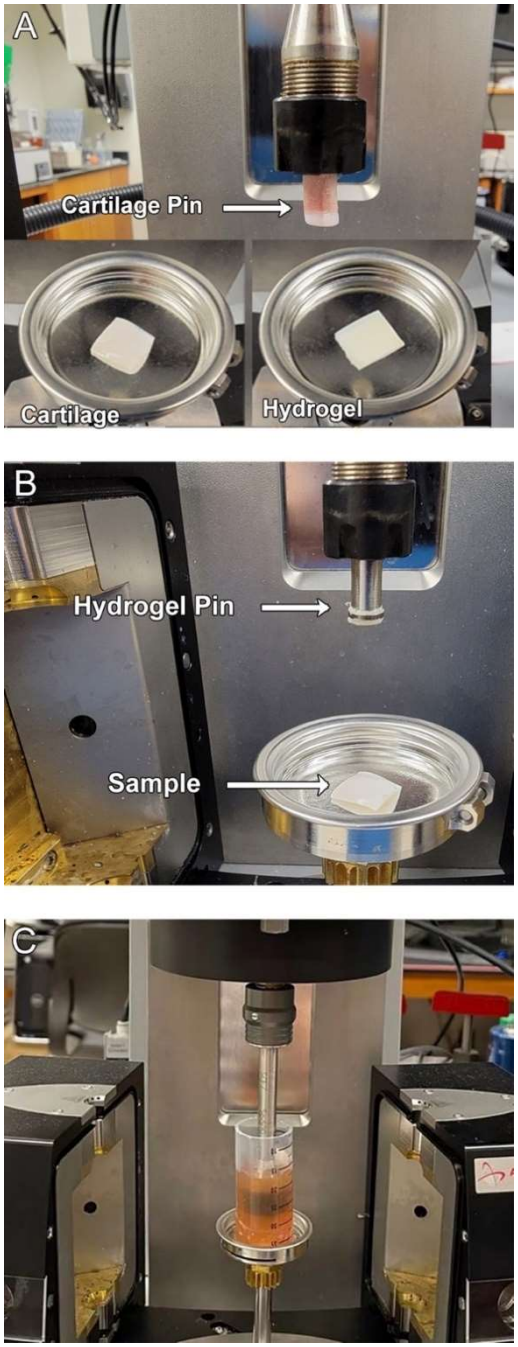

Figure 19. Images of the test setup using (A) a cartilage pin and (B) a hydrogel pin for the measurement of the wear and COF. (C) Image during the wear test.

4.2.13 Shear Testing

Shear testing was performed on an 830LE63 Axial Torsion Test Machine equipped with a 100 lb load cell. Each test was performed in a customized shear test fixture (see **Figure 10**). For shearing of cartilage or hydrogel on metal samples, the sample was secured in a cylindrical hole in the left side of the fixture. The hole size was 6 mm for the pig plug and 7 mm for the hydrogel samples. Spacers were added underneath the samples to precisely align the shear plane to the cartilage-bone or hydrogel-metal interface. The right side of the fixture was machined to have a complementary half-cylinder that was used to push the hydrogel or cartilage off of their substrates. The diameter of the right half-cylinder matched that of the left side (either 6 or 7 mm). Rubber was placed between the sample and the right shear fixture to apply pressure during the shear test in order to minimize cleavage and peeling. A crosshead displacement rate of 2 mm min^{-1} was used for all the measurements.

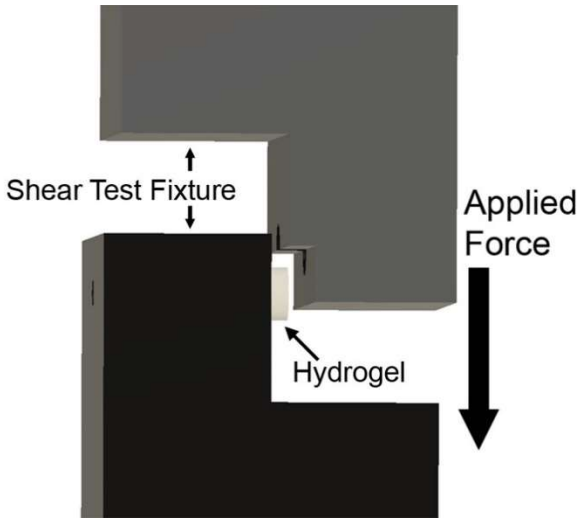

Figure 10. Image of the shear test fixture used for shearing cartilage off bone and the hydrogel off metal rods.

4.3. Results

4.3.1 Effect of Annealing on Morphology

We first examine the effect of the hydrogel composition on the shape of the sample after drying, annealing and rehydration (or simply "annealing" to be concise). **Figure 20A** shows a sample of BC became wrinkled and folded at the edges after annealing. BC samples that were annealed in a 10 wt% solution of PVA were also deformed (**Figure 20B**). The PVA layer that forms on top of the BC after annealing contains a large number of bubbles and easily delaminates from the BC film. The bubbles are presumably the result of the evaporation of water. **Figure 20C** shows a sample of 40 wt% PVA also formed a large number of bubbles and deformed during the annealing process. However, reinforcement of 40 wt% PVA with BC allowed the hydrogel to retain its shape without deformation after annealing. We attribute this lack of deformation to the higher solid content and tensile modulus of the BC-reinforced PVA. The nanoscale network of the BC layer appears to suppress the formation of the large bubbles that are visible in the 40 wt% PVA sample. Comparing Figure 1B&D indicates that the approach of infiltrating a high concentration of PVA into BC in a hydrothermal bomb, followed by removal of excess PVA from the BC surface, results in a more uniform hydrogel than if a BC sample is placed in a more dilute PVA solution that is concentrated via drying. These results demonstrate that, unlike BC alone, PVA alone, or the combination of BC with a 10 wt% of PVA, the BC infiltrated with 40 wt% PVA could retain its shape and remain relatively free of bubbles and other defects after annealing.

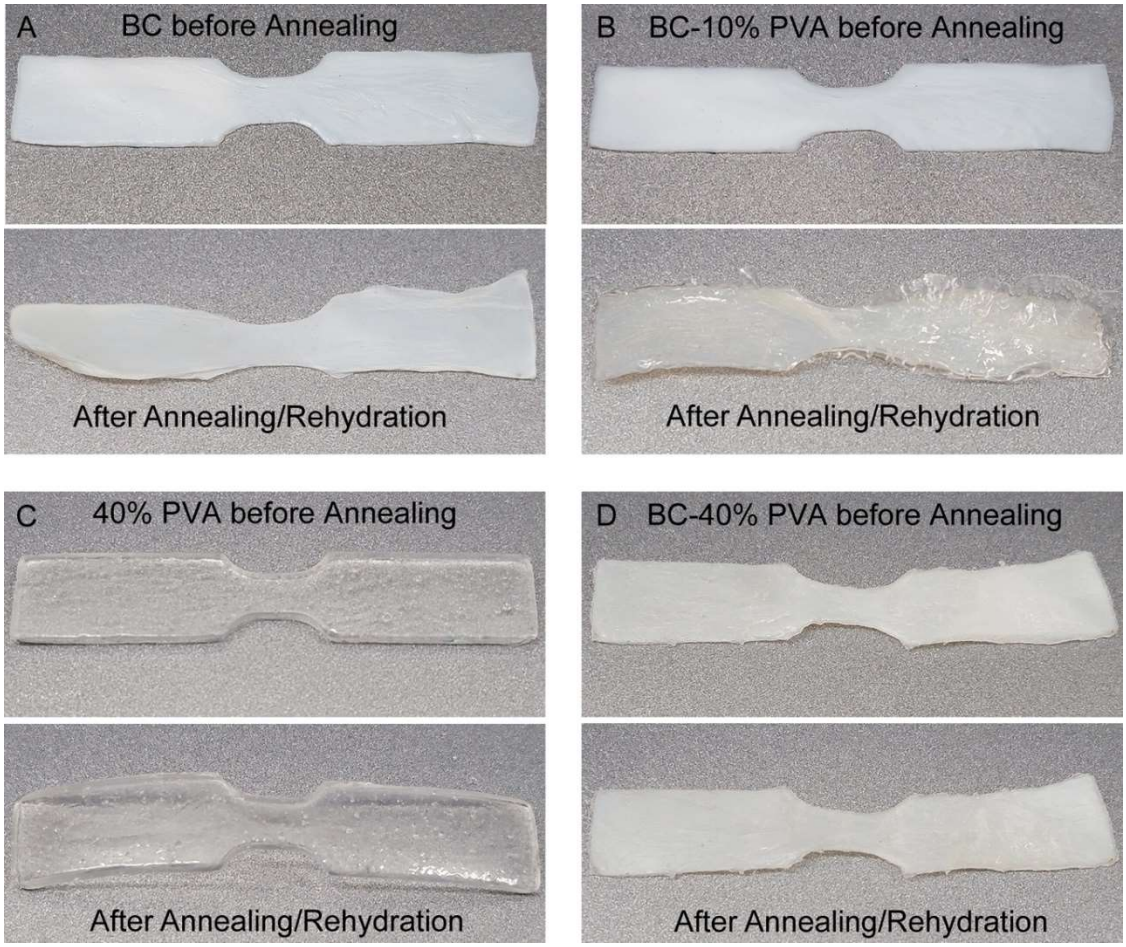

Figure 20. Hydrogel samples before and after annealing and rehydration. All samples were annealed at 90°C for 25 hours and rehydrated in PBS solution for 24 hours at 23°C. (A) A sample of BC without PVA. (B) A sample of BC that was annealed in a solution of 10 wt% PVA. (C) A sample of PVA. (D) A BC sample that was infiltrated with 40 wt% PVA in a hydrothermal bomb for 24 hours at 120°C before annealing and rehydration.

4.3.2 Effect of Annealing on the Mechanical Properties of PVA hydrogel

To determine the effects of annealing on the mechanical properties of various hydrogel compositions, we first analyzed the effects of annealing on a PVA hydrogel as a reference point. The PVA was fully hydrolyzed with a molecular weight of 145,000 g mol^{-1}. A 40 wt.% PVA solution was dried at 90°C for 24 hours, annealed at 90°C, 120°C or 140°C, and then placed in a 0.15 M PBS solution for 24 hours for rehydration. PVA samples that underwent a freeze-thaw cycle were tested for comparison. **Figure 21A** and **21B** show that annealing the hydrogel dramatically increased the tensile and compressive strength relative to samples that had undergone a freeze-thaw cycle. **Figure 22D** show that, relative to the freeze-thaw process, annealing increased the tensile strength by 60 times (from 0.26 to 15.6 MPa) and the compressive strength by 9 times (from 14.8 to 140.8 MPa). Increasing the annealing temperature from 90°C to 140°C led to an increase in the tensile strength and modulus, similar to previous work.[102, 103] The increase in strength and modulus has been ascribed to the increase in the crystallinity and solid content of the hydrogel after annealing. **Figure 21E** confirms that the crystallinity and solid content of the annealed PVA hydrogels are much greater than that of a freeze-thawed PVA hydrogel. For example, a PVA hydrogel made via the freeze-thaw process has an overall solid content of 0.09 and a PVA crystallinity of 0.21, whereas a PVA hydrogel made via annealing at 90°C has an overall solid content of 0.42 and a PVA crystallinity of 0.58. The crystallites formed during annealing strengthen the otherwise amorphous PVA by acting as tough cross-links that redistribute applied stresses and hinder crack propagation.[102, 110] The crystallites also increase the solid content and strength of the hydrogel by reducing the amount of water taken up by the PVA when it is soaked in 0.15 M PBS after annealing.

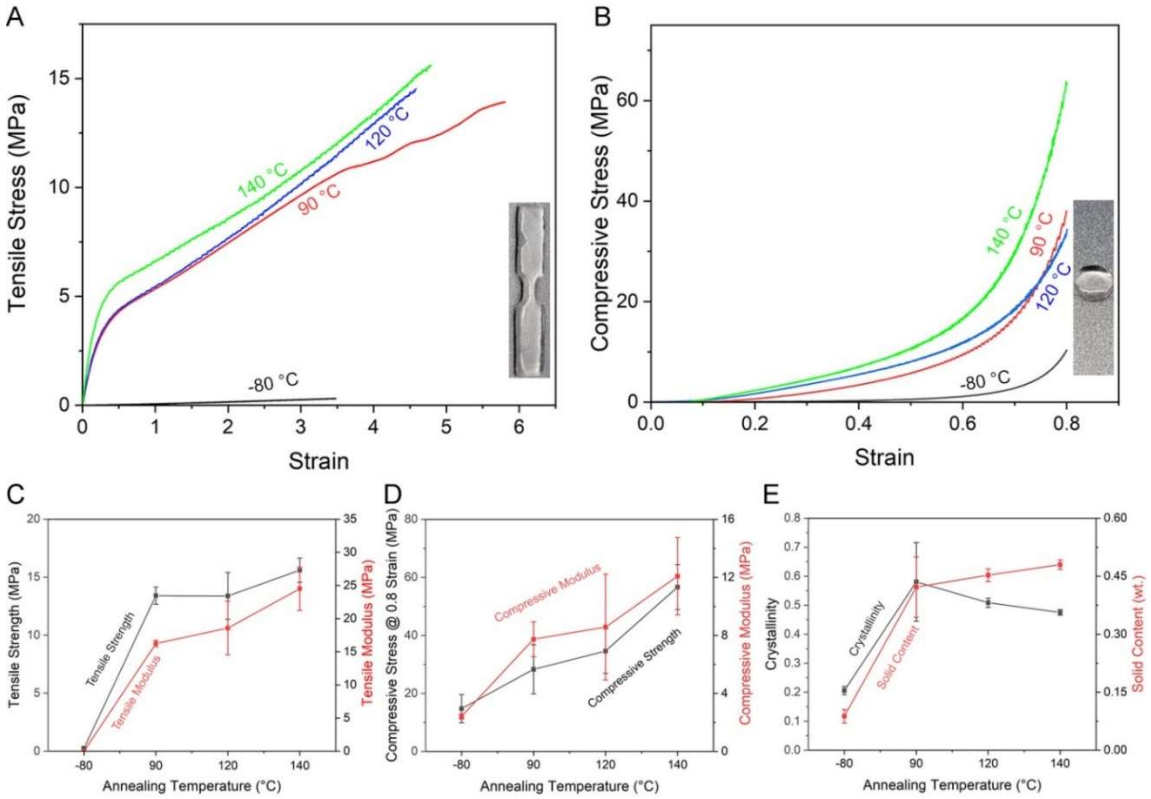

Figure 21. (A&B) Representative tensile stress-strain curves and compressive stress-strain curves for PVA hydrogels annealed at different temperatures. (C) Tensile strength and moduli of PVA annealed at different temperatures. (D) Compressive stress at 0.8 strain and moduli of PVA annealed at different temperatures. (E) Crystallinity and solid content weight fraction of PVA annealed at different temperatures.

4.3.3 Effect of Annealing on a BC-PVA hydrogel

Next, we applied the same annealing process to BC-PVA hydrogels. As with the PVA hydrogels, the BC-PVA hydrogels were dried at 90°C for 24 hours, annealed at 90°C, 120°C or 140°C, and then placed in a 0.15 M PBS solution for 24 hours for rehydration. **Figure 22A** and **22C** show the tensile strength of the annealed BC-PVA hydrogels reached 50.4 MPa, an increase of 4.6 times relative to the BC-PVA that went through a freeze-thaw cycle, and an increase of 3.2 times relative to annealed PVA that was not reinforced with BC. **Figure 22B and 22D** show the compressive strength increased from 55.32 MPa to 95.35 MPa after annealing. Similar to the PVA hydrogel, this dramatic increase in strength can be attributed to the increase in crystallinity and solid content after annealing. **Figure 22E** shows the crystallinity of the BC-PVA hydrogel increased from 0.07 after a freeze-thaw cycle to 0.4 after annealing. The solid weight fraction of the BC-PVA hydrogel increased from 0.11 after a freeze-thaw cycle to 0.53 after annealing. These results shows that PVA can still form crystallites within the nanofibrous BC network, and that these crystallites increase the solid content and strength of the hydrogel.

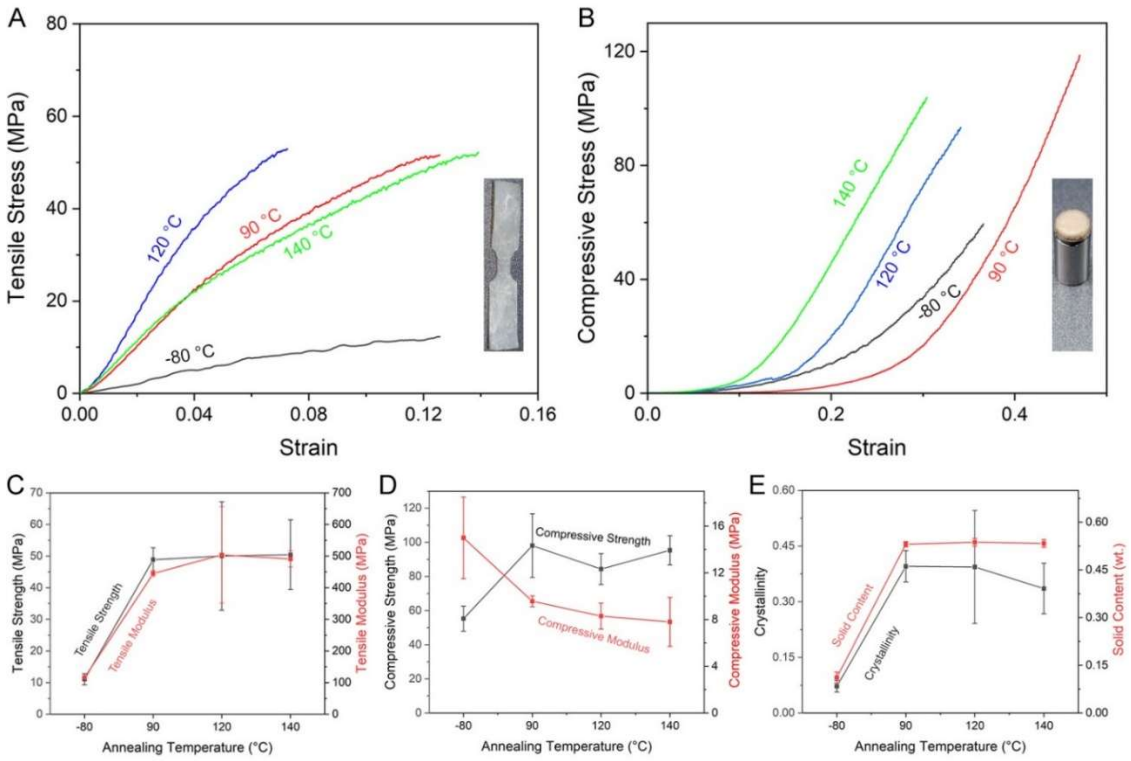

Figure 22. (A &B) Representative tensile and compressive stress-strain curves) for BC-PVA hydrogels annealed at different temperatures. (C) Tensile strength and moduli of BC-PVA annealed at different temperatures. (D) Compressive strength and moduli of BC-PVA annealed at different temperatures. Crystallinity and solid content weight fraction (E) of BC-PVA annealed at different temperatures. Crystallinity here stands for the weight fraction of crystalline PVA in the entire hydrogel sample, including the PVA and water.

4.3.4 Effect of PAMPS on an Annealed BC-PVA hydrogel

We previously reported that the incorporation of PAMPS into a BC-PVA hydrogel made with a freeze-thaw cycle resulted in an increase in the tensile and compressive strength of the hydrogel.[94] Thus, we next sought to determine the effect of incorporating PAMPS into an annealed BC-PVA hydrogel. As shown in **Figure 23A**, the addition of PAMPS into the annealed BC-PVA hydrogel led to a decrease in the solid content relative to BC-PVA alone, from 0.53 to 0.37. DSC thermograms (see **Figure 17**) show that after the addition of 10 wt% PAMPS, the peak from melting crystalline PVA disappeared, indicating the addition of PAMPS destroys the PVA

crystallites that form during the annealing process. The decrease in solid content and loss of crystallinity upon addition of PAMPS led to a decrease in the tensile strength (from 48.9 MPa to 20.8 MPa), tensile modulus (from 444.8 MPa to 150.5 MPa) and compressive strength (from 98.1 MPa to 56.0 MPa in **Figure 23B**) of the hydrogel. The increase in water content of the hydrogel and loss of strength was likely due to the fact that PAMPS is a negatively charged polymer, and this negative charge results in an osmotic pressure that swells the hydrogel with water.[94]

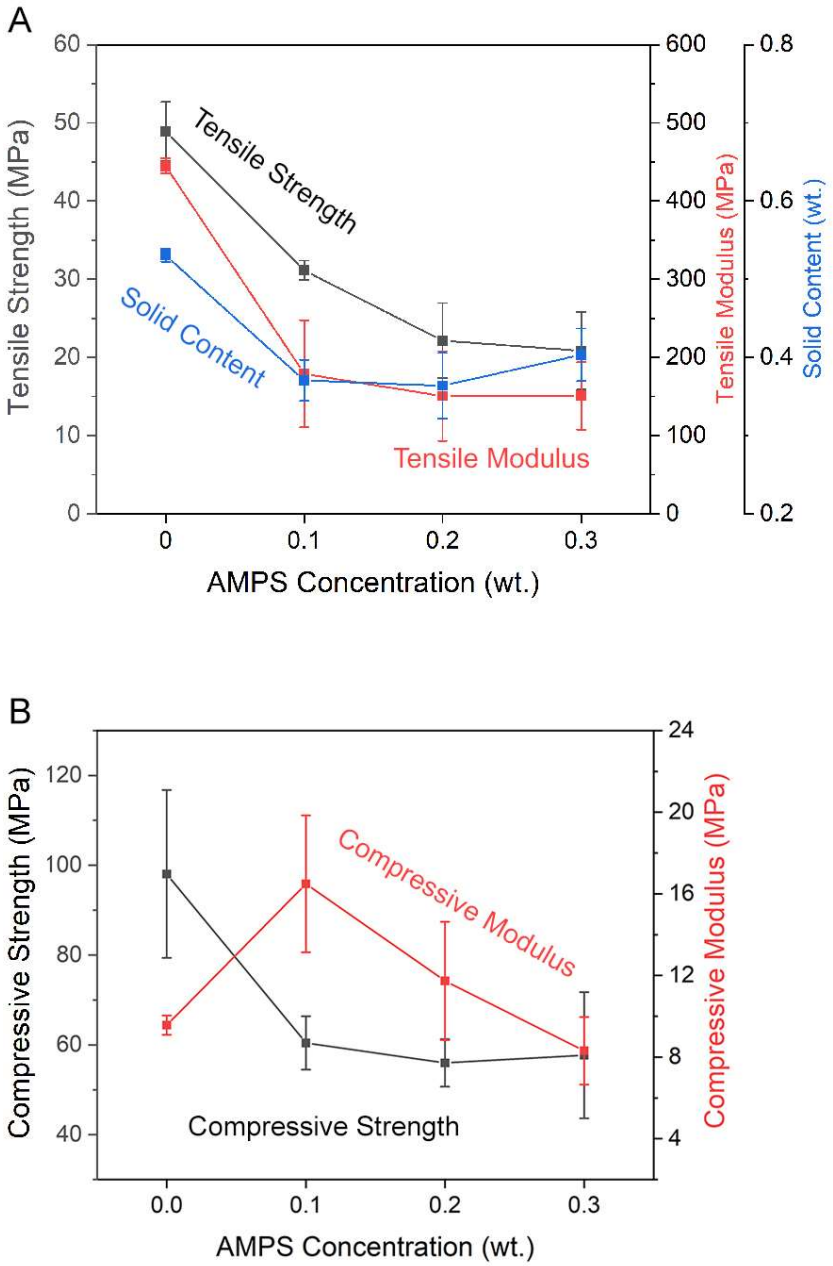

Figure 23. (A) Tensile strength, tensile moduli and solid content weight fraction of BC-PVA-PAMPS hydrogels that were made with solutions containing different concentrations of the AMPS monomer. BC-PVA samples were annealed before infiltration of AMPS. (B) Compressive strength and moduli of BC-PVA-PAMPS hydrogels.

4.3.5 Wear and COF of Hydrogels against Cartilage

The wear resistance of a potential replacement for cartilage exceeds that of cartilage to ensure durability and minimize the generation of wear debris that could potentially cause an adverse biological reaction. We have previously shown that the wear resistance of a BC-PVA-PAMPS hydrogel is equivalent to that of cartilage and is superior to that PVA or PVA-PAMPS when tested against a stainless-steel pin.[94] These hydrogels were made by applying a freeze-thaw cycle to crystallize the PVA. Here we compare the wear resistance of PVA-based hydrogels (PVA, BC-PVA, and BC-PVA-PAMPS) that have been dried and annealed at 90ºC to that of porcine cartilage when tested against a porcine cartilage plug in FBS. **Figures 19** shows our pin-on-disc configuration for testing the wear of hydrogels in fetal bovine serum (FBS). The porcine cartilage plug was rotated against the hydrogel surface 10^6 times under 1 MPa of pressure and at a speed of 319 rotations per minute (maximum linear velocity was 100 mm s^{-1}). **Figure 24A** is a schematic illustration of how the wear test was performed.

Figure 24B shows cross-sectional Micro-CT images of the hydrogels that were acquired in the center of the wear mark to measure the maximum wear depth. **Figure 24C** compares the wear depth of the hydrogels and cartilage. The wear depth of the BC-PVA hydrogel with 0% AMPS was 70.1 μm. The addition of 20% AMPS decreased the mean wear depth to 65.9 μm, but the difference between the 0% and 20% AMPS samples was not statistically significant. This comparison illustrates that the negative charge and higher water content caused by incorporating PAMPS into an annealed BC-PVA hydrogel does not significantly improve the wear resistance. Both of these values were 3 times lower than the wear depth on the cartilage sample, which was 227.8 μm. The wear depth for annealed and rehydrated PVA was 301.0 μm, four times greater than either BC-PVA sample. These results indicate the presence of BC in the hydrogel can dramatical improve the wear resistance of an annealed PVA hydrogel to be superior to that of cartilage

We also recorded the COF during the wear test. Cartilage maintained a constant COF of 0.020 during the test. The COF of BC-PVA decreased during the test from 0.040 to 0.021. The BC-PVA hydrogel with 20% AMPS had a similar COF as that without AMPS. In contrast, the COF of PVA increased dramatically during the test, from 0.033 to 0.135. Previous work has similarly demonstrated the COF of PVA against cartilage increases over time while the COF of cartilage against cartilage is constant.[111, 112] The increase in the COF for a PVA-Cartilage interface has been ascribed to transfer of damaged PVA to the cartilage surface, which in turn decreases the ability of the cartilage surface to maintain a lubricating water layer.[112] The incorporation of BC into PVA clearly inhibits damage of the hydrogel, allowing it to maintain a low coefficient of friction similar to that cartilage during the wear test. The presence of AMPS in the hydrogel does not appear to be necessary for maintaining a low COF and high resistance to wear.

It is critical that materials used for cartilage replacement on one side of the joint, i.e., on the femoral condyle, do not cause wear of cartilage on the opposing surface, i.e., the tibial plateau. Traditional orthopedic materials like cobalt-chrome and ultra-high molecular-weight polyethylene are known to damage an opposing cartilage surface to a greater extent than hydrogels due to the higher COF and hardness of traditional orthopedic materials.[113-115] To assess the wear caused by BC-PVA and BC-PVA-PAMPS hydrogels on cartilage, we created hydrogel plugs for wear testing (see **section 4.2.8**). Hydrogel plugs were pressed against cartilage samples (see **Figure 25A** and **Figure 19B**) with 1 MPa of pressure, and rotated 10^6 times at a speed of 319 rotations per minute (the maximum linear velocity at the circumference of the pin was 100 mm s^{-1}).

Figure 25B shows cross-sectional Micro-CT images of the cartilage samples that were acquired in the center of the wear mark to measure the maximum wear depth. **Figure 25C** compares the wear depth on cartilage caused by the hydrogels or cartilage. The wear caused by the BC-PVA on cartilage (247 ± 16 μm) was not significantly different from the wear caused by cartilage on

cartilage (228 ± 12 μm). The addition of PAMPS into the BC-PVA reduced the wear on the opposing cartilage surface to 81 ± 27 μm, significantly below the wear of cartilage on cartilage.

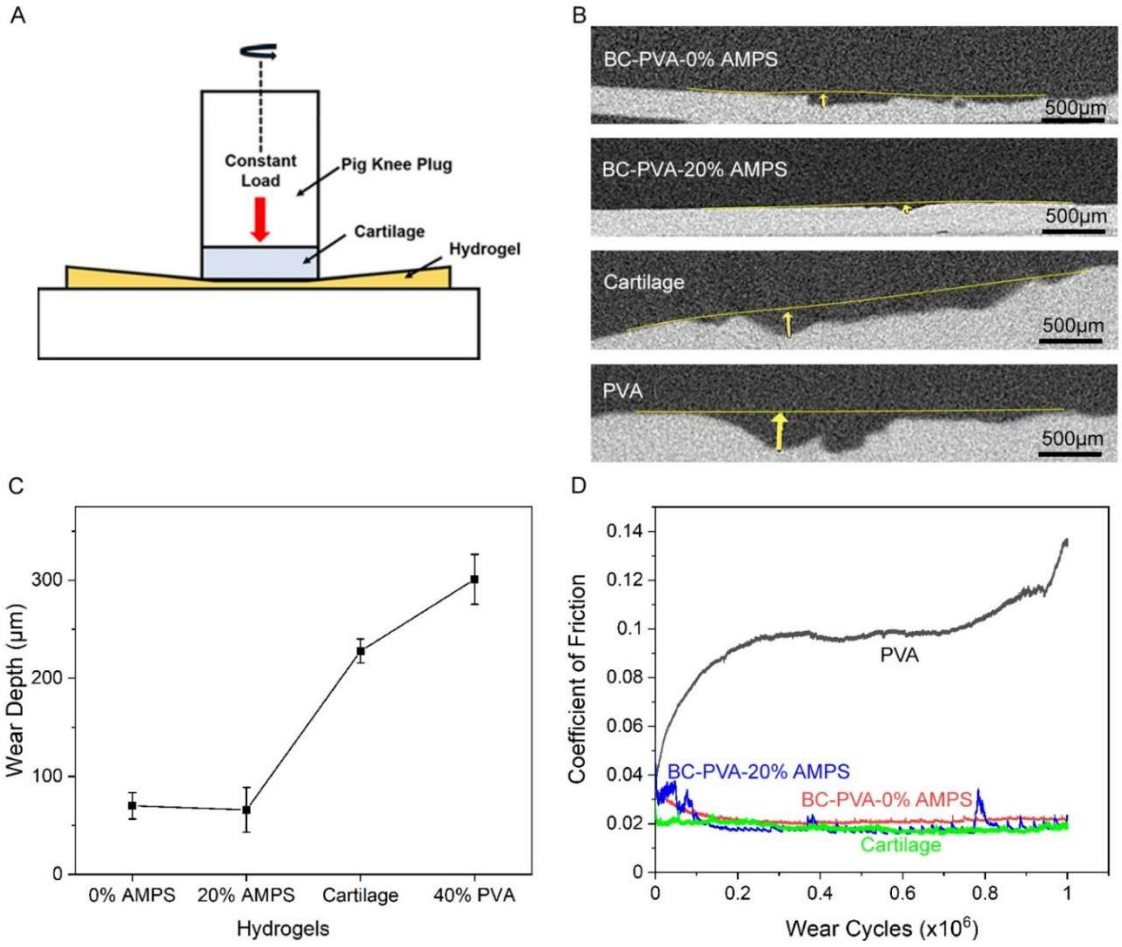

Figure 24. (A) A schematic for how the wear of hydrogels vs. cartilage was measured. (B) Micro-CT cross-section images and (C) the wear depth of cartilage and hydrogel samples after 106 cycles under 1 MPa of pressure, a spin rate of 100 mm/s, and with FBS as the lubricant. (D) The coefficient of friction between cartilage and the hydrogels during the tests over 24 hours.

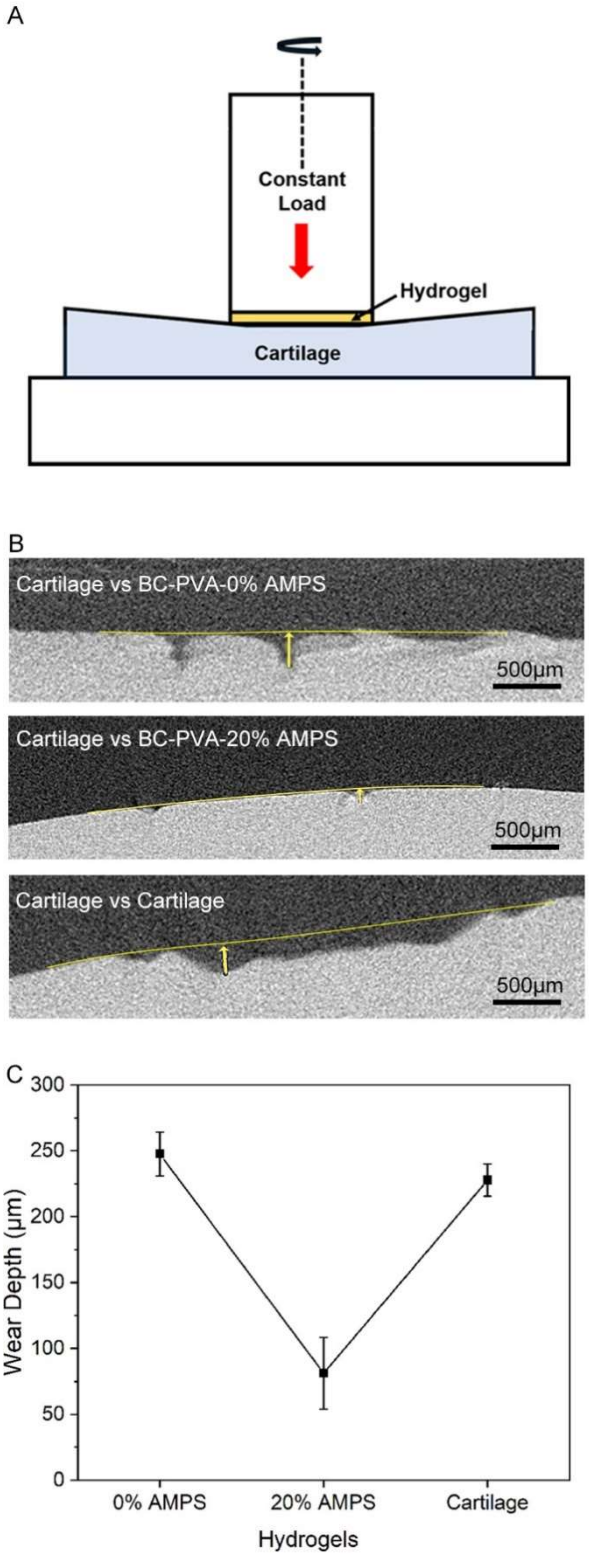

Figure 25. (A) A schematic for how the wear of cartilage vs. hydrogels was measured. (B) Micro-CT cross-section images and (C) the wear depth of cartilage and hydrogel samples after 106 cycles under 1 MPa of pressure, a spin rate of 100 mm/s, and with FBS as the lubricant.

4.3.6 Shear Strength

We hypothesized that increasing the tensile strength of the hydrogel should also increase the shear strength. In order to be used for a cartilage replacement material, a synthetic hydrogel must be secured into a defect site with the same shear strength as the junction between cartilage and bone. One way to accomplish this goal is to have hydrogels that directly attach to bone or cartilage with sufficient strength, but this is not yet possible. Alternatively, the hydrogel can be attached to a metallic base, such as titanium, which has the ability to integrate with bone. We have previously reported the ability to attach BC-PVA-PAMPS hydrogels to a metallic base with a shear strength equivalent to the cartilage-bone interface. This attachment method used the same combination of adhesive and shape memory alloy ring that we used to construct the hydrogel plugs for wear testing. Previous tests indicated the strength of hydrogel attachment was limited by the tensile force required to fracture the hydrogel that is curved over the edge of the metallic base. Thus, increasing the tensile strength of the hydrogel should in turn increase the shear strength with which the hydrogel is attached to a metallic base.

The setup used for shear testing is illustrated in F**igure 10**. **Figure 26** shows the results for shear testing a plug of porcine cartilage on bone extracted from a pig knee, testing of a BC-PVA-PAMPS hydrogel made with the previous freeze-thaw process, and testing a BC-PVA hydrogel annealed at 90 °C and then rehydrated. Both of the hydrogels are attached to stainless-steel rods with a combination of RelyX Ultimate cement and a shape memory alloy ring. The BC-PVA shear strength of 1.98 is significantly greater than that of porcine cartilage (*p*-value from one-way ANOVA is <0.05). The average value of the shear strength for BC-PVA is also 40% greater than that of BC-PVA-PAMPS, but the error in the measurements is such that the difference in these values are not statistically significant. Comparison of the sample after failure show that while pig cartilage was sheared completely off of the underlying bone, both BC-PVA-PAMPS (made with the freeze-thaw process) and BC-PVA (made by annealing at 90 °C, followed by rehydration) were

fractured on one side of the cylindrical sample but remained attached. These results show that the shear strength of attachment for the annealed BC-PVA is greater than that of pig cartilage.

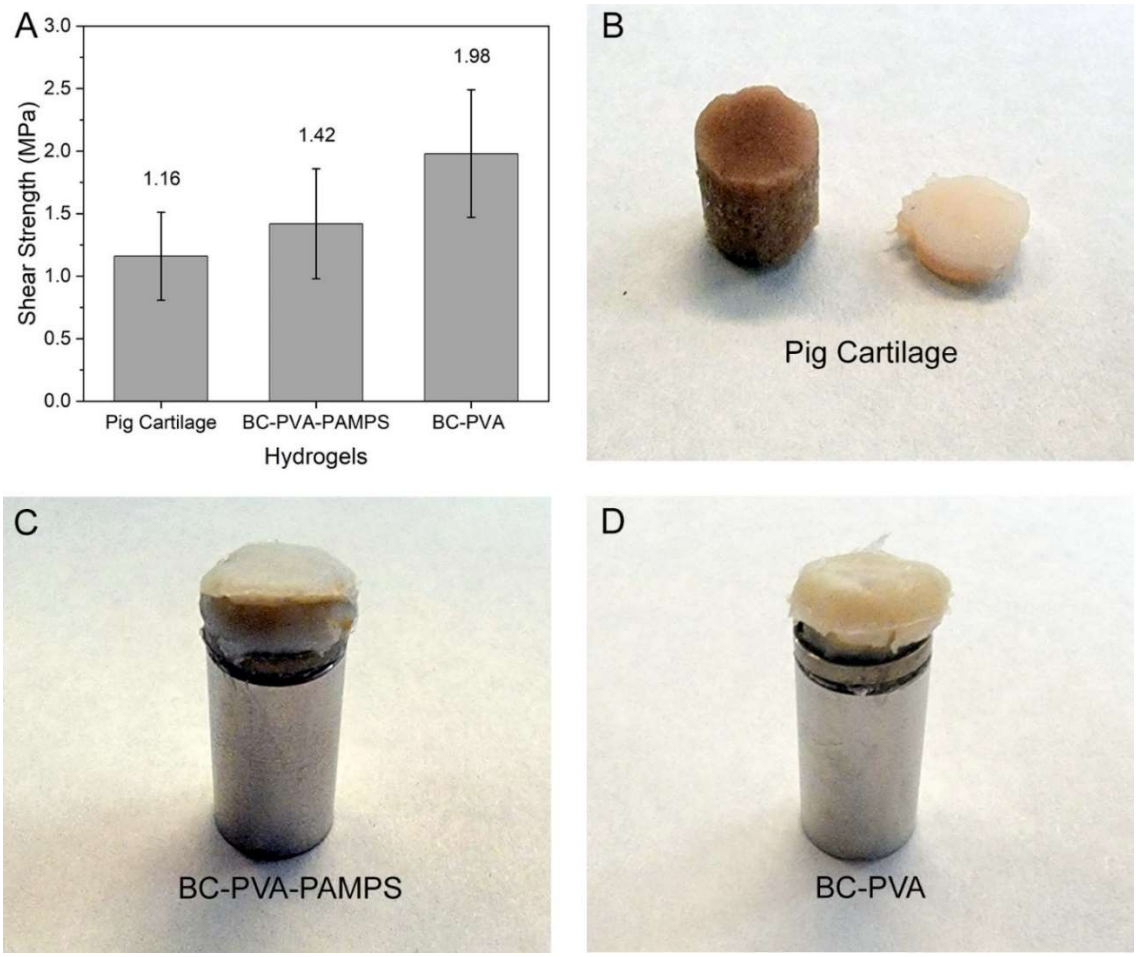

Figure 26. (A) Results for shear testing of pig cartilage and hydrogels secured to metal pins with adhesive and shape memory alloy clamps. (B-D) Images of samples after testing to failure. The osteochondral plug was extracted from a pig knee. The BC-PVA-PAMPS hydrogel was fabricated with the freeze-thaw process. The BC-PVA hydrogel was annealed at 90 ℃ and rehydrated.

4.3.7 Application to an Implant for Partial Knee Resurfacing

Thus far we have described the compression strength and shear strength of BC-reinforced hydrogels attached to a metal pin with a diameter of 5.2 mm. While this size is convenient for testing, such a diameter is too small to serve as an implant for partial knee resurfacing. In addition, the samples

lacked the curvature necessary to mimic the natural curvature of the femoral condyle. Thus we sought to demonstrate the ability of the hydrogel to attach to a metal base with a size and shape representative of an implant for partial knee resurfacing.

Figure 27A&B show images of an implant 20 mm in diameter with a radius of curvature of 20 mm. An implant diameter of 20 mm is a typical size used for an osteochondral allograft, and a 20 mm radius of curvature is within the range of typical curvatures for the femoral condyle.[116] The peak force on the knee during jogging has been measured to be 5 551 N for a body weight of 100 kg.[117] The tibiofemoral contact area has been measured to be 1 500 mm^2 at 3 100 N.[118] If we make the conservative assumption that the contact area will not increase at a higher force, then the peak stress on the contacted area of the knee during jogging is 3.7 MPa. The implants in Figure 8C&D were subjected to a stress of 16 MPa, 4.3 times greater than the peak physiological force on the femoral condyle. After this test, there were no signs of fracture or damage on the surface of the hydrogel. This test indicates an implant created with the annealed BC-PVA hydrogel can withstand the compressive forces in the knee without fracture.

Peak anterior shear forces in the knee for walking have been measured to be 30% of body weight, or 294 N for a 100 kg individual.[119] This is the highest shear force measured in the knee for any investigated daily activity.[117] The tibiofemoral contact area has been measured to be 1 500 mm^2 at 3 100 N, which is approximately equivalent to the peak normal force during walking for an individual with a body weight of 100 kg.[118] As the peak normal force coincides with the peak shear force, we can use this tibiofemoral contact area to calculate that the peak shear stress experienced by cartilage during walking is 0.2 MPa (294 N ÷ 1 500 mm^2). Shear testing on the implant indicated failure did not occur until a stress of 0.9 MPa was applied. Since the implant can withstand shear loads 4.5 times greater than that experienced by cartilage in the knee, this result shows the annealed BC-PVA hydrogel and method of attachment have sufficient strength for creation of an implant for partial knee resurfacing.

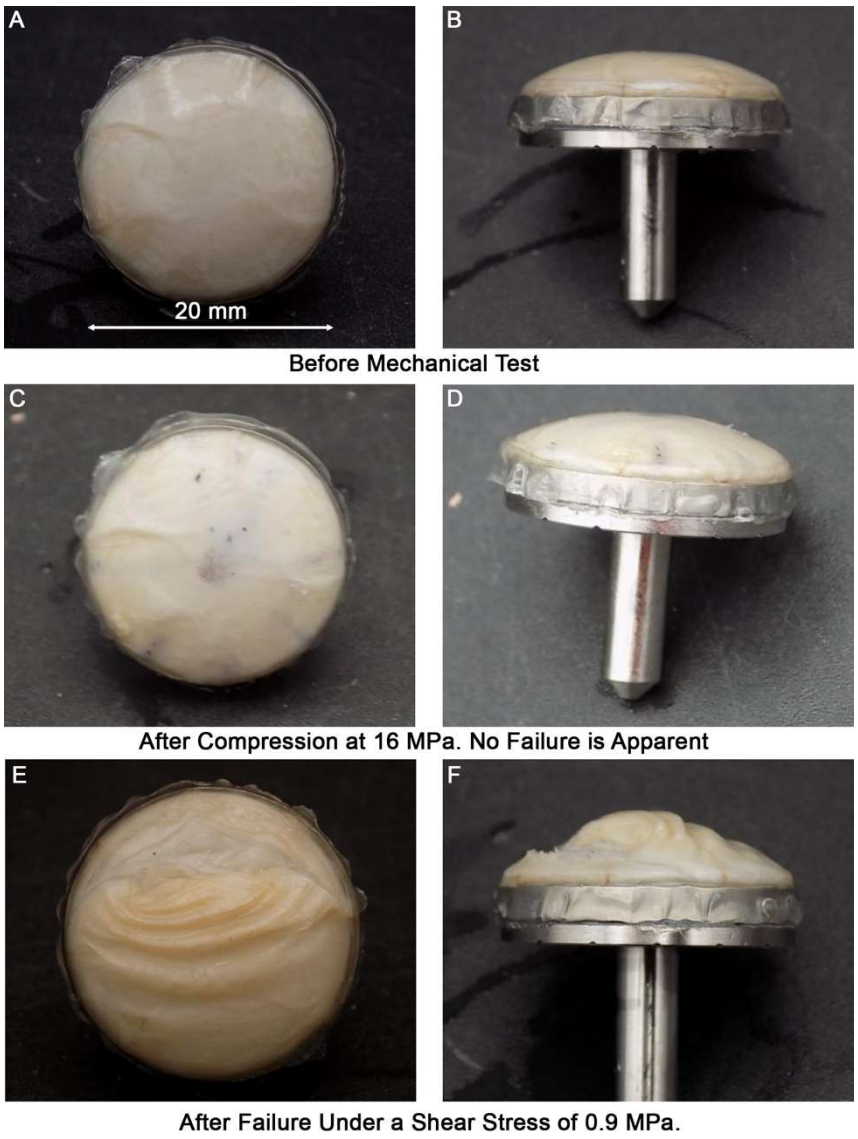

Figure 27. (A) Top and (B) side images of a 20-mm-diameter implant for partial knee resurfacing of the femoral condyle. (C) Top and (B) side images after compression at 16 MPa, which show there are no signs of failure. (E) Top and (F) side images after failure under a shear stress of 0.9 MPa.

5. Nanoclay Doped Synthetic Hydrogel

5.1 Introduction

As discussed in chapter 4, we introduced an annealing process to increase the crystallinity of PVA, thus further increased the mechanical strength of resulted BC-PVA hydrogel. By using this method, we successfully eliminate the use of AMPS (2-acrylamido-2-methyl-1-propanesulfonic acid sodium salt), which may be a potential hazard if implanted. However, as shown in chapter 4, the wear performance of the annealed BC-PVA-AMPS gel on opposing cartilage is better than the annealed BC-PVA gel, it may be due to the negative charge of the PAMPS network, since negatively charged polymer network has shown to provide good lubricity. Gong et al[120] studied the COF of a PAMPS-PMAAm hydrogel, which had a cartilage equivalent compressive strength. The COF was showed to be 0.04 against a cylindrical alumina ceramic pin, compared to 0.07 of a UHMWPE. The wear depth after 1,000,000 wear cycles has shown to be 3.2 μm, similar to that of UHMWPE (3.33 μm). Kinjo et al[121] and Gong et al[122] attribute the low friction of PAMPS hydrogels to the repulsion forces provided between the PAMPS network and the opposing surface (often glass or ceramic). So, we want to replace AMPS with a charged nanoclay which is shown to be biocompatible, aiming for a better wear performance compared to the annealed BC-PVA hydrogel

Laponite is a biocompatible product,[123, 124] which is mostly used in research about Drug Delivery, bioimaging, Regenerative medicine and tissue engineering[125]. A few of research has introduced laponite as a rheology modifier to increase the printability of hydrogel. However, few research has done on the change of the tribological properties with laponite, here, we propose that by adding the laponite particle in the BC-PVA network, the charge of nanoparticle will lead to a better lubrication and wear performance. At the same time, the BC-PVA network will help to maintain the mechanical property in the cartilage-equivalent range.

5.2 Methods

5.2.1 Fabrication of Annealed BC-PVA Hydrogel

BC sheets were pressed to be 0.5 mm thick and placed into a hydrothermal reactor with a mixture of PVA (40 wt.%) and DI water (60 wt.%). The hydrothermal reactor was sealed and heated at 135°C for 24 hours to allow the PVA to diffuse into the voids of BC and form a BC-PVA hydrogel. The BC-PVA hydrogel was removed from the reactor when hot (>85°C). Note the hydrothermal reactor was pressurized with hot steam and created a burn hazard, so personal protective equipment including lab coat, heat resistant gloves and full-coverage face shields should be used when opening the reactor. The residual PVA solution was removed by scrapping the surface of the BC-PVA samples with a metal spatula. The samples were dried in an oven at 90°C for 24 hours. The resulting annealed BC-PVA hydrogel was cut into a desired shape and stored in 0.15 M PBS for at least 24 hours before tests.

5.2.2 Fabrication of Annealed LAP-BC-PVA Hydrogel

BC sheets were pressed to be 0.5 mm thick and placed into a hydrothermal reactor with a mixture of Laponite (1%)- PVA (40 wt.%) and DI water (59 wt.%). The hydrothermal reactor was sealed and heated at 135°C for 24 hours to allow the PVA and Laponite to diffuse into the voids of BC and form a LAP-BC-PVA hydrogel. The LAP-BC-PVA hydrogel was removed from the reactor when hot (>85°C). Note the hydrothermal reactor was pressurized with hot steam and created a burn hazard, so personal protective equipment including lab coat, heat resistant gloves and full-coverage face shields should be used when opening the reactor. The residual PVA solution was removed by scrapping the surface of the LAP-BC-PVA samples with a metal spatula. The samples were dried in an oven at 90°C for 24 hours. The resulting annealed LAP-BC-PVA hydrogel was cut into a desired shape and stored in 0.15 M PBS for at least 24 hours before tests.

5.2.3 Fabrication of Annealed LAP-BC-PVA-2 Hydrogel

BC sheets were pressed to be 0.5 mm thick and placed into a hydrothermal reactor with a mixture of PVA (40 wt.%) and DI water (60 wt.%). The hydrothermal reactor was sealed and heated

at 135°C for 24 hours to allow the PVA and Laponite to diffuse into the voids of BC and form a BC-PVA hydrogel. The BC-PVA hydrogel was removed from the reactor when hot (>85°C). Note the hydrothermal reactor was pressurized with hot steam and created a burn hazard, so personal protective equipment including lab coat, heat resistant gloves and full-coverage face shields should be used when opening the reactor. The residual PVA solution was removed by scrapping the surface of the BC-PVA samples with a metal spatula. The same process was repeated with a mixture of Laponite (1%), PVA (40%) and DI water (59%). The samples were dried in an oven at 90°C for 24 hours. The resulting annealed LAP-BC-PVA-2 hydrogel was cut into a desired shape and stored in 0.15 M PBS for at least 24 hours before tests.

5.3 Results

As can be seen in the figure 28, although the tensile strength of the LAP-BC-PVA gel is still in the cartilage equivalent range, it's much lower than the BC-PVA gel that we previously discussed, we believed that it's due to the high viscosity of the LAP-PVA solution, which leads to less PVA diffused into the BC network. So, instead of only one PVA infiltration step, we developed a two-step PVA infiltration. By starting with infiltration of pure PVA solution followed by the PVA-LAP solution, we ensure the enough amount of PVA in the network as well as the addition of laponite. The resulted tensile strength proved the two-step infiltration is necessary for the mechanical strength of hydrogel.

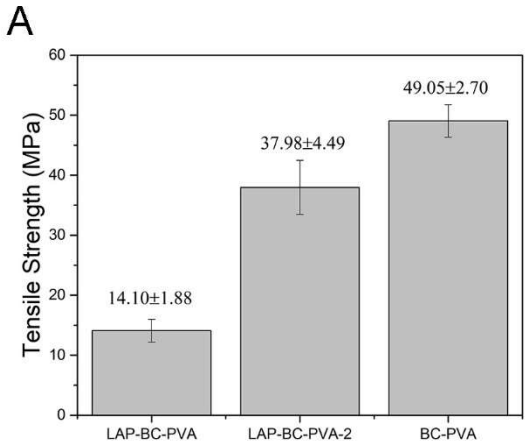

Figure 28. Mechanical strength of Hydrogel

We then examined the wear performance of the LAP-BC-PVA-2 against the pig cartilage after 1,000,000 cycles, as can be seen in the **figure 29A**, although the wear depth of LAP-BC-PVA-2 is slightly larger than BC-PVA (not statistically significant), it's much less than the wear depth of cartilage

Similar tests were done on the wear test of cartilage again LAP-BC-PVA-2, as can be seen in **figure 29B**, there's no obvious wear mark on the cartilage surface after 1,000,000 wear cycles, shown the excellent wear performance of LAP-BC-PVA-2 gel.

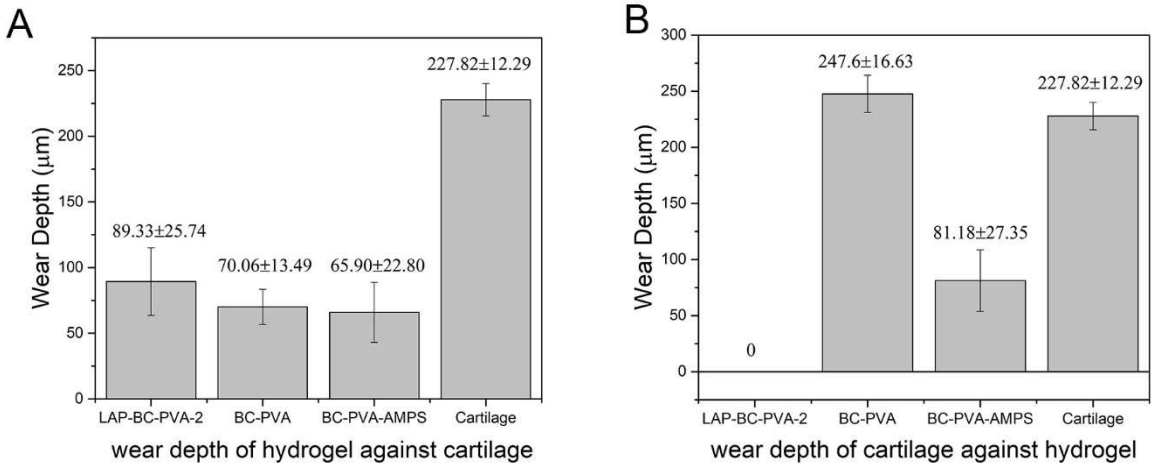

Figure 29. (A) Wear depth of hydrogel against cartilage and (B) wear depth of cartilage against hydrogel

5.4 Conclusion

In conclusion, by using two-step infiltration process, the Laponite can be added to the hydrogel network while still maintain a cartilage equivalent mechanical property. The doping of charged laponite into the hydrogel network resulted in a better wear performance than the original BC-PVA hydrogel.

6. Conclusion and Future Plan

In conclusion, the work of developing two medical devices is demonstrated in the thesis. To solve the specific medical problem, medical device was developed, then the requirement for the medical device is researched. We achieved the desired properties by changing the material and its structure.

To test CT system and evaluate new CT technology, a 3D printed physical phantom was developed. The 3D printing parameters were tested to optimize the uniformity across the phantom. 2D-NPS was used to examine the uniformity. A backfilling printing method was developed to achieve up to 8 levels of contrast with smooth transition in one object. A contrast detailed phantom and an anthropomorphic liver phantom was fabricated based on the backfilling method. Based on the work we have done, researchers can easily create more detailed physical phantoms including realistic, anthropomorphic textures. Such phantoms could be used in CT research including task-specific assessment of imaging technology or patient-specific optimization of acquisition protocols.

In order to further improve the uniformity of the printed physical phantom, a higher resolution FFF printer with a small nozzle size and finer nozzle control can be used. Besides, to address the discrepancy of HU value in backfilling regions, especially in a small area, a printer with more advanced motor and extrusion control can be used. This will help deposit tiny amount of material on the desired region accurately.

Currently we are using a single material to provide the attenuation difference within the CT image, which may be adequate for evaluating non-contrast protocols on conventional CT systems. However, dual energy or photon counting CT requires discerning other materials like iodine or calcium. This can be potentially solved by multi-material printing using commercial or customized filaments, thanks to the open nature of FFF. Future work may focus on using the backfilling method and optimized printing parameters with multiple materials to create phantoms with multiple attenuation levels and material properties that are clinically relevant.

To replace the damaged cartilage in knee, a hydrogel coated orthopedic implant was developed. The requirement for the hydrogel implant is that the hydrogel itself needs to have an cartilage equivalent mechanical properties and wear performance. Moreover, we need to secure the hydrogel tightly in the defect sites.

In order to tightly secure the hydrogel, we can attach the hydrogel to a metal base and implant the whole implant into the bone. In order to enhance the attachment, we developed a new design of hydrogel attachment method by using shape-memory alloy ring-clamp to bypass the delamination of bacterial cellulose layers, which was the limitation of previous cement-adhered sample. The shear test fixture was developed, and the shear strength of the ring clamped sample was proved to be comparable to or even better than the osteochondral joints. In order to further increase the gel's mechanical properties, an annealing process in hydrogel fabrication process was introduced. A 3.2-fold improvement in the tensile strength (from 15.6 to 50.5 MPa) and a 1.7-fold increase in the compressive strength (from 56.7 to 95.4 MPa) was achieved. By using this method, we successfully eliminated the necessity of including a potentially hazardous ingredient to the hydrogel composite for better biosafety and potentially sooner mass application. The annealed hydrogel was proved to have a similar or better wear resistance compared to pig articular cartilage. The wear performance of the hydrogel was further improved by doping the biocompatible nanoclay into the synthetic hydrogel. The mechanical strength of the gel was also in the cartilage-equivalent range. Taken together, a suitable material for cartilage resurfacing was developed, we also integrated it into an actual implant that can be implanted in human knees.

Regarding the future work, currently, the human size implant was fabricated with 5 layers BC, the thickness of top hydrogel is about 1 mm. Although it's much improved compared to previous NEST method, which only contains one layer of gel, but there's still room for improvement considering the thickness of actual cartilage is about 2-4 mm. Due to the using heat-shrinkable ring, the shape of the implant was limited to shape of the ring, which makes it less ideal for fabricating patient specific implant. A potential way to solve this problem is to replace the BC sheets with 3D

composite made by cellulose nanofiber. By eliminating the layered structure of BC, the shear strength won't be limited by the delamination of BC layers if NEST method is used. A thicker hydrogel can also be fabricated using this method, which will better mimicking the actual cartilage. To conclude, by improving the mechanical properties of the hydrogel and achieving better attachment between the hydrogel and base, an orthopedic implant for cartilage repair was developed, this can serve as a minimally invasive treatment for chondral or osteochondral defects of the knee.

References

1. Scafa Udriște, A.; Niculescu, A.-G.; Grumezescu, A. M.; Bădilă, E., Cardiovascular Stents: A Review of Past, Current, and Emerging Devices. *Materials (Basel)* **2021,** *14* (10), 2498.

2. Ho, M.-Y.; Chen, C.-C.; Wang, C.-Y.; Chang, S.-H.; Hsieh, M.-J.; Lee, C.-H.; Wu, V. C.; Hsieh, I. C., The Development of Coronary Artery Stents: From Bare-Metal to Bio-Resorbable Types. *Metals* **2016,** *6* (7).

3. Ako, J.; Bonneau, H. N.; Honda, Y.; Fitzgerald, P. J., Design Criteria for the Ideal Drug-Eluting Stent. *The American Journal of Cardiology* **2007,** *100* (8, Supplement 2), S3-S9.

4. Tsai, M. L.; Hsieh, M. J.; Chen, C. C.; Chang, S. H.; Wang, C. Y.; Chen, D. Y.; Yang, C. H.; Yeh, J. K.; Ho, M. Y.; Hsieh, I. C., Comparison of 9-Month Angiographic Follow-Up and Long-Term Clinical Outcomes of Biodegradable Polymer Drug-Eluting Stents and Second-Generation Durable Polymer Drug-Eluting Stents in Patients Undergoing Single Coronary Artery Stenting. *Acta Cardiologica Sinica* **2020,** *36* (2), 97-104.

5. Panetta, J.; Zhou, Q.; Malomo, L.; Pietroni, N.; Cignoni, P.; Zorin, D., Elastic textures for additive fabrication. **2015,** *34* (4 %J ACM Trans. Graph.), Article 135.

6. Comotti, C.; Regazzoni, D.; Rizzi, C.; Vitali, A., Additive Manufacturing to Advance Functional Design: An Application in the Medical Field. *Journal of Computing and Information Science in Engineering* **2017,** *17* (3).

7. Brenner, D. J.; Hall, E. J., Computed tomography--an increasing source of radiation exposure. *The New England journal of medicine* **2007,** *357* (22), 2277-84.

8. Linet, M. S.; Slovis, T. L.; Miller, D. L.; Kleinerman, R.; Lee, C.; Rajaraman, P.; Berrington de Gonzalez, A., Cancer risks associated with external radiation from diagnostic imaging procedures. *CA: a cancer journal for clinicians* **2012,** *62* (2), 75-100.

9. Radiation Dose in X-Ray and CT Exams (2021) https://www.radiologyinfo.org/en/info/safety-xray

10. Robinson, D., The Phantoms of Medical and Health Physics. *Medical Physics* **2016,** *43* (9), 5264-5264.

11. Teoh, E. J.; McGowan, D. R.; Macpherson, R. E.; Bradley, K. M.; Gleeson, F. V., Phantom and Clinical Evaluation of the Bayesian Penalized Likelihood Reconstruction Algorithm Q.Clear on an LYSO PET/CT System. *Journal of nuclear medicine : official publication, Society of Nuclear Medicine* **2015,** *56* (9), 1447-52.

12. Schindera, S. T.; Diedrichsen, L.; Müller, H. C.; Rusch, O.; Marin, D.; Schmidt, B.; Raupach, R.; Vock, P.; Szucs-Farkas, Z., Iterative reconstruction algorithm for abdominal

multidetector CT at different tube voltages: assessment of diagnostic accuracy, image quality, and radiation dose in a phantom study. *Radiology* **2011,** *260* (2), 454-62.

13. Birnbaum, B. A.; Hindman, N.; Lee, J.; Babb, J. S., Renal cyst pseudoenhancement: influence of multidetector CT reconstruction algorithm and scanner type in phantom model. *Radiology* **2007,** *244* (3), 767-75.

14. Segars, W. P.; Mahesh, M.; Beck, T. J.; Frey, E. C.; Tsui, B. M., Realistic CT simulation using the 4D XCAT phantom. *Med Phys* **2008,** *35* (8), 3800-8.

15. Segars, W. P.; Bond, J.; Frush, J.; Hon, S.; Eckersley, C.; Williams, C. H.; Feng, J.; Tward, D. J.; Ratnanather, J. T.; Miller, M. I.; Frush, D.; Samei, E., Population of anatomically variable 4D XCAT adult phantoms for imaging research and optimization. *Med Phys* **2013,** *40* (4), 043701.

16. Geyer, A. M.; O'Reilly, S.; Lee, C.; Long, D. J.; Bolch, W. E., The UF/NCI family of hybrid computational phantoms representing the current US population of male and female children, adolescents, and adults--application to CT dosimetry. *Physics in medicine and biology* **2014,** *59* (18), 5225-42.

17. Hurtado, J. L.; Lee, C.; Lodwick, D.; Goede, T.; Williams, J. L.; Bolch, W. E., Hybrid computational phantoms representing the reference adult male and adult female: construction and applications for retrospective dosimetry. *Health physics* **2012,** *102* (3), 292-304.

18. Abadi, E.; Harrawood, B.; Sharma, S.; Kapadia, A.; Segars, W. P.; Samei, E., DukeSim: A Realistic, Rapid, and Scanner-Specific Simulation Framework in Computed Tomography. *IEEE transactions on medical imaging* **2019,** *38* (6), 1457-1465.

19. Badano, A.; Badal, A.; Glick, S. J.; Graff, C. G.; Samuelson, F. W.; Sharma, D.; Zeng, R. In *In silico imaging clinical trials for regulatory evaluation: initial considerations for VICTRE, a demonstration study*, Medical Imaging, 2017.

20. Abadi, E.; Segars, W. P.; Harrawood, B.; Sharma, S.; Kapadia, A.; Samei, E., Virtual clinical trial for quantifying the effects of beam collimation and pitch on image quality in computed tomography. *Journal of medical imaging (Bellingham, Wash.)* **2020,** *7* (4), 042806.

21. Abadi, E.; Segars, W. P.; Tsui, B. M. W.; Kinahan, P. E.; Bottenus, N.; Frangi, A. F.; Maidment, A.; Lo, J.; Samei, E., Virtual clinical trials in medical imaging: a review. *Journal of medical imaging (Bellingham, Wash.)* **2020,** *7* (4), 042805.

22. Filippou, V.; Tsoumpas, C., Recent advances on the development of phantoms using 3D printing for imaging with CT, MRI, PET, SPECT, and ultrasound. *Med Phys* **2018,** *45* (9), e740-60.

23. Carton, A. K.; Bakic, P.; Ullberg, C.; Derand, H.; Maidment, A. D., Development of a physical 3D anthropomorphic breast phantom. *Med Phys* **2011,** *38* (2), 891-6.

24. Solomon, J.; Ba, A.; Bochud, F.; Samei, E., Comparison of low-contrast detectability between two CT reconstruction algorithms using voxel-based 3D printed textured phantoms. *Med Phys* **2016,** *43* (12), 6497.

25. Rossman, A. H.; Catenacci, M.; Zhao, C.; Sikaria, D.; Knudsen, J. E.; Dawes, D.; Gehm, M. E.; Samei, E.; Wiley, B. J.; Lo, J. Y., Three-dimensionally-printed anthropomorphic physical phantom for mammography and digital breast tomosynthesis with custom materials, lesions, and uniform quality control region. *Journal of medical imaging (Bellingham, Wash.)* **2019,** *6* (2), 021604.

26. Jahnke, P.; Schwarz, S.; Ziegert, M.; Schwarz, F. B.; Hamm, B.; Scheel, M., Paper-based 3D printing of anthropomorphic CT phantoms: Feasibility of two construction techniques. *European radiology* **2019,** *29* (3), 1384-1390.

27. Ardila Pardo, G. L.; Conzelmann, J.; Genske, U.; Hamm, B.; Scheel, M.; Jahnke, P., 3D printing of anatomically realistic phantoms with detection tasks to assess the diagnostic performance of CT images. *European radiology* **2020,** *30* (8), 4557-4563.

28. Hong, D.; Lee, S.; Kim, G. B.; Lee, S. M.; Kim, N.; Seo, J. B., Development of a CT imaging phantom of anthromorphic lung using fused deposition modeling 3D printing. *Medicine (Baltimore)* **2020,** *99* (1), e18617-e18617.

29. Ceh, J.; Youd, T.; Mastrovich, Z.; Peterson, C.; Khan, S.; Sasser, T. A.; Sander, I. M.; Doney, J.; Turner, C.; Leevy, W. M., Bismuth Infusion of ABS Enables Additive Manufacturing of Complex Radiological Phantoms and Shielding Equipment. *Sensors (Basel, Switzerland)* **2017,** *17* (3).

30. Hamedani, B. A.; Melvin, A.; Vaheesan, K.; Gadani, S.; Pereira, K.; Hall, A. F., Three-dimensional printing CT-derived objects with controllable radiopacity. *Journal of applied clinical medical physics* **2018,** *19* (2), 317-328.

31. Mohamed, O. A.; Masood, S. H.; Bhowmik, J. L., Optimization of fused deposition modeling process parameters: a review of current research and future prospects. *Advances in Manufacturing* **2015,** *3* (1), 42-53.

32. Zhang, H.; Chen, J., Current status and future directions of cancer immunotherapy. *Journal of Cancer* **2018,** *9* (10), 1773-1781.

33. Dancewicz, O. L.; Sylvander, S. R.; Markwell, T. S.; Crowe, S. B.; Trapp, J. V., Radiological properties of 3D printed materials in kilovoltage and megavoltage photon beams. *Physica medica : PM : an international journal devoted to the applications of physics to medicine and biology : official journal of the Italian Association of Biomedical Physics (AIFB)* **2017,** *38*, 111-118.

34. Ivanov, D.; Bliznakova, K.; Buliev, I.; Popov, P.; Mettivier, G.; Russo, P.; Di Lillo, F.; Sarno, A.; Vignero, J.; Bosmans, H.; Bravin, A.; Bliznakov, Z., Suitability of low density materials for 3D printing of physical breast phantoms. *Physics in medicine and biology* **2018,** *63* (17), 175020.

35. Sophia Fox, A. J.; Bedi, A.; Rodeo, S. A., The basic science of articular cartilage: structure, composition, and function. *Sports Health* **2009,** *1* (6), 461-468.

36. Buckwalter, J. A., Articular cartilage injuries. *Clinical orthopaedics and related research* **2002,** (402), 21-37.

37. Hjelle, K.; Solheim, E.; Strand, T.; Muri, R.; Brittberg, M., Articular cartilage defects in 1,000 knee arthroscopies. *Arthroscopy : the journal of arthroscopic & related surgery : official publication of the Arthroscopy Association of North America and the International Arthroscopy Association* **2002,** *18* (7), 730-4.

38. Weightman, B.; Chappell, D. J.; Jenkins, E. A., A second study of tensile fatigue properties of human articular cartilage. *Annals of the Rheumatic Diseases* **1978,** *37* (1), 58.

39. Kaplan, J. T.; Neu, C. P.; Drissi, H.; Emery, N. C.; Pierce, D. M., Cyclic loading of human articular cartilage: The transition from compaction to fatigue. *Journal of the Mechanical Behavior of Biomedical Materials* **2017,** *65*, 734-742.

40. Merkely, G.; Ackermann, J.; Lattermann, C., Articular Cartilage Defects: Incidence, Diagnosis, and Natural History. *Operative Techniques in Sports Medicine* **2018,** *26* (3), 156-161.

41. Ahmed, T. A. E.; Hincke, M. T., Strategies for Articular Cartilage Lesion Repair and Functional Restoration. *Tissue Engineering Part B: Reviews* **2009,** *16* (3), 305-329.

42. Badley, E. M.; Wang, P. P., Arthritis and the aging population: projections of arthritis prevalence in Canada 1991 to 2031. *The Journal of rheumatology* **1998,** *25* (1), 138-44.

43. Mehrotra, C.; Remington, P. L.; Naimi, T. S.; Washington, W.; Miller, R., Trends in total knee replacement surgeries and implications for public health, 1990-2000. *Public Health Rep* **2005,** *120* (3), 278-282.

44. Falah, M.; Nierenberg, G.; Soudry, M.; Hayden, M.; Volpin, G., Treatment of articular cartilage lesions of the knee. *International orthopaedics* **2010,** *34* (5), 621-30.

45. Messner, K.; Maletius, W., The long-term prognosis for severe damage to weight-bearing cartilage in the knee: a 14-year clinical and radiographic follow-up in 28 young athletes. *Acta orthopaedica Scandinavica* **1996,** *67* (2), 165-8.

46. Browne, J. E.; Branch, T. P., Surgical alternatives for treatment of articular cartilage lesions. *The Journal of the American Academy of Orthopaedic Surgeons* **2000,** *8* (3), 180-9.

47. Yen, Y. M.; Cascio, B.; O'Brien, L.; Stalzer, S.; Millett, P. J.; Steadman, J. R., Treatment of osteoarthritis of the knee with microfracture and rehabilitation. *Medicine and science in sports and exercise* **2008,** *40* (2), 200-5.

48. Kreuz, P. C.; Erggelet, C.; Steinwachs, M. R.; Krause, S. J.; Lahm, A.; Niemeyer, P.; Ghanem, N.; Uhl, M.; Südkamp, N., Is microfracture of chondral defects in the knee associated with different results in patients aged 40 years or younger? *Arthroscopy : the journal of arthroscopic & related surgery : official publication of the Arthroscopy Association of North America and the International Arthroscopy Association* **2006,** *22* (11), 1180-6.

49. Solheim, E.; Hegna, J.; Inderhaug, E., Long-Term Survival after Microfracture and Mosaicplasty for Knee Articular Cartilage Repair: A Comparative Study Between Two Treatments Cohorts. *Cartilage* **2020,** *11* (1), 71-76.

50. Brittberg, M.; Faxén, E.; Peterson, L., Carbon fiber scaffolds in the treatment of early knee osteoarthritis. A prospective 4-year followup of 37 patients. *Clinical orthopaedics and related research* **1994,** (307), 155-64.

51. Paletta, G. A., Jr.; Manning, T.; Snell, E.; Parker, R.; Bergfeld, J., The effect of allograft meniscal replacement on intraarticular contact area and pressures in the human knee. A biomechanical study. *The American journal of sports medicine* **1997,** *25* (5), 692-8.

52. Minas, T., Autologous chondrocyte implantation for focal chondral defects of the knee. *Clinical orthopaedics and related research* **2001,** (391 Suppl), S349-61.

53. Harris, J. D.; Siston, R. A.; Pan, X.; Flanigan, D. C., Autologous chondrocyte implantation: a systematic review. *The Journal of bone and joint surgery. American volume* **2010,** *92* (12), 2220-33.

54. Willers, C.; Wood, D. J.; Zheng, M. H., A CURRENT REVIEW ON THE BIOLOGY AND TREATMENT OF ARTICULAR CARTILAGE DEFECTS (PART I & PART II). *Journal of Musculoskeletal Research* **2003,** *07* (03n04), 157-181.

55. Gudas, R.; Kalesinskas, R. J.; Kimtys, V.; Stankevičius, E.; Toliušis, V.; Bernotavičius, G.; Smailys, A., A Prospective Randomized Clinical Study of Mosaic Osteochondral Autologous Transplantation Versus Microfracture for the Treatment of Osteochondral Defects in the Knee Joint in Young Athletes. *Arthroscopy: The Journal of Arthroscopic & Related Surgery* **2005,** *21* (9), 1066-1075.

56. Levy, Y. D.; Görtz, S.; Pulido, P. A.; McCauley, J. C.; Bugbee, W. D., Do fresh osteochondral allografts successfully treat femoral condyle lesions? *Clinical orthopaedics and related research* **2013,** *471* (1), 231-237.

57. Fuchs, A.; Eberbach, H.; Izadpanah, K.; Bode, G.; Sudkamp, N. P.; Feucht, M. J., Focal metallic inlay resurfacing prosthesis for the treatment of localized cartilage defects of the femoral

condyles: a systematic review of clinical studies. *Knee Surg. Sports. Traumatol. Arthrosc.* **2018,** *26*, 2722-2732.

58. Kempson, G. E., Age-related changes in the tensile properties of human articular cartilage: a comparative study between the femoral head of the hip joint and the talus of the ankle joint. *Biochimica et Biophysica Acta (BBA) - General Subjects* **1991,** *1075* (3), 223-230.

59. Kerin, A. J.; Wisnom, M. R.; Adams, M. A., The compressive strength of articular cartilage. *Proceedings of the Institution of Mechanical Engineers. Part H, Journal of engineering in medicine* **1998,** *212* (4), 273-80.

60. Kempson, G. E., Relationship between the tensile properties of articular cartilage from the human knee and age. *Annals of the Rheumatic Diseases* **1982,** *41* (5), 508.

61. Zhao, Y.; Li, M.; Liu, B.; Xiang, J.; Cui, Z.; Qu, X.; Qiu, D.; Tian, Y.; Yang, Z., Ultra-tough injectable cytocompatible hydrogel for 3D cell culture and cartilage repair. *Journal of Materials Chemistry B* **2018,** *6* (9), 1351-1358.

62. Xu, L.; Zhao, X.; Xu, C.; Kotov, N. A., Water-Rich Biomimetic Composites with Abiotic Self-Organizing Nanofiber Network. *Advanced Materials* **2018,** *30* (1), 1703343.

63. Haque, M. A.; Kurokawa, T.; Gong, J. P., Super tough double network hydrogels and their application as biomaterials. *Polymer* **2012,** *53* (9), 1805-1822.

64. Zhang, Z.; Liu, R.; Zepeda, H.; Zeng, L.; Qiu, J.; Wang, S., 3D Printing Super Strong Hydrogel for Artificial Meniscus. *ACS Applied Polymer Materials* **2019,** *1* (8), 2023-2032.

65. Oliveira, A. S.; Schweizer, S.; Nolasco, P.; Barahona, I.; Saraiva, J.; Colaço, R.; Serro, A. P., Tough and Low Friction Polyvinyl Alcohol Hydrogels Loaded with Anti-inflammatories for Cartilage Replacement. *Lubricants* **2020,** *8* (3).

66. Kumar, P.; Oka, M.; Nakamura, T.; Yamamuro, T.; Delecrin, J., Mechanical strength of osteochondral junction. *Nihon Seikeigeka Gakkai Zasshi* **1991,** *65* (11), 1070-1077.

67. Chivers, R. A.; Wolowacz, R. G., The strength of adhesive-bonded tissue joints. *International Journal of Adhesion and Adhesives* **1997,** *17* (2), 127-132.

68. Maier Greg, P.; Rapp Michael, V.; Waite, J. H.; Israelachvili Jacob, N.; Butler, A., Adaptive synergy between catechol and lysine promotes wet adhesion by surface salt displacement. *Science* **2015,** *349* (6248), 628-632.

69. Zhao, Q.; Lee, D. W.; Ahn, B. K.; Seo, S.; Kaufman, Y.; Israelachvili, Jacob N.; Waite, J. H., Underwater contact adhesion and microarchitecture in polyelectrolyte complexes actuated by solvent exchange. *Nature Materials* **2016,** *15* (4), 407-412.

70. Singla, S.; Amarpuri, G.; Dhopatkar, N.; Blackledge, T. A.; Dhinojwala, A., Hygroscopic compounds in spider aggregate glue remove interfacial water to maintain adhesion in humid conditions. *Nature Communications* **2018,** *9* (1), 1890.

71. Zhao, J.; Kirillova, A.; Kelly, C. N.; Xu, H.; Koshut, W. J.; Yang, F.; Gall, K.; Wiley, B. J., High-Strength Hydrogel Attachment through Nanofibrous Reinforcement. *Advanced Healthcare Materials* **2021,** *10* (4), 2001119.

72. Zito, F.; De Bernardi, E.; Soffientini, C.; Canzi, C.; Casati, R.; Gerundini, P.; Baselli, G., The use of zeolites to generate PET phantoms for the validation of quantification strategies in oncology. *Medical Physics* **2012,** *39* (9), 5353-5361.

73. Hattori, K.; Ikemoto, Y.; Takao, W.; Ohno, S.; Harimoto, T.; Kanazawa, S.; Oita, M.; Shibuya, K.; Kuroda, M.; Kato, H., Development of MRI phantom equivalent to human tissues for 3.0-T MRI. *Med Phys* **2013,** *40* (3), 032303.

74. Ianniello, C.; de Zwart, J. A.; Duan, Q.; Deniz, C. M.; Alon, L.; Lee, J.-S.; Lattanzi, R.; Brown, R., Synthesized tissue-equivalent dielectric phantoms using salt and polyvinylpyrrolidone solutions. *Magn Reson Med* **2018,** *80* (1), 413-419.

75. Williams, M. B.; Mangiafico, P. A.; Simoni, P. U., Noise power spectra of images from digital mammography detectors. *Med Phys* **1999,** *26* (7), 1279-93.

76. Samei, E.; Bakalyar, D.; Boedeker, K. L.; Brady, S.; Fan, J.; Leng, S.; Myers, K. J.; Popescu, L. M.; Ramirez Giraldo, J. C.; Ranallo, F.; Solomon, J.; Vaishnav, J.; Wang, J., Performance evaluation of computed tomography systems: Summary of AAPM Task Group 233. *Medical Physics* **2019,** *46* (11), e735-e756.

77. Lev, M. H.; Gonzalez, R. G., 17 - CT Angiography and CT Perfusion Imaging. In *Brain Mapping: The Methods (Second Edition)*, Toga, A. W.; Mazziotta, J. C., Eds. Academic Press: San Diego, 2002; pp 427-484.

78. Solomon, J.; Mileto, A.; Ramirez-Giraldo, J. C.; Samei, E., Diagnostic Performance of an Advanced Modeled Iterative Reconstruction Algorithm for Low-Contrast Detectability with a Third-Generation Dual-Source Multidetector CT Scanner: Potential for Radiation Dose Reduction in a Multireader Study. *Radiology* **2015,** *275* (3), 735-45.

79. Gromovykh, T. I.; Pigaleva, M. A.; Gallyamov, M. O.; Ivanenko, I. P.; Ozerova, K. E.; Kharitonova, E. P.; Bahman, M.; Feldman, N. B.; Lutsenko, S. V.; Kiselyova, O. I., Structural organization of bacterial cellulose: The origin of anisotropy and layered structures. *Carbohydr. Polym.* **2020,** *237*, 116140.

80. Yamanaka, S.; Watanabe, K.; Kitamura, N.; Iguchi, M.; Mitsuhashi, S.; Nishi, Y.; Uryu, M., The structure and mechanical properties of sheets prepared from bacterial cellulose. *Journal of Materials Science* **1989,** *24* (9), 3141-3145.

81. An, S.-J.; Lee, S.-H.; Huh, J.-B.; Jeong, S. I.; Park, J.-S.; Gwon, H.-J.; Kang, E.-S.; Jeong, C.-M.; Lim, Y.-M., Preparation and Characterization of Resorbable Bacterial Cellulose Membranes Treated by Electron Beam Irradiation for Guided Bone Regeneration. *Int. J. Mol. Sci.* **2017,** *18* (11).

82. Cai, Z.; Kim, J., Preparation and Characterization of Novel Bacterial Cellulose/Gelatin Scaffold for Tissue Regeneration Using Bacterial Cellulose Hydrogel. *J. Nanotechnol. Eng. Med.* **2010,** *1* (2).

83. Chen, P.; Cho, S. Y.; Jin, H.-J., Modification and applications of bacterial celluloses in polymer science. *Macromolecular Research* **2010,** *18* (4), 309-320.

84. Pircher, N.; Veigel, S.; Aigner, N.; Nedelec, J. M.; Rosenau, T.; Liebner, F., Reinforcement of bacterial cellulose aerogels with biocompatible polymers. *Carbohydr. Polym.* **2014,** *111*, 505-513.

85. Jeffery, A. K.; Blunn, G. W.; Archer, C. W.; Bentley, G., Three-dimensional collagen architecture in bovine articular cartilage. *The Journal of Bone and Joint Surgery. British volume* **1991,** *73-B* (5), 795-801.

86. Tong, L.; Mouritz, A. P.; Bannister, M. K., Chapter 1 - Introduction. In *3D Fibre Reinforced Polymer Composites*, Tong, L.; Mouritz, A. P.; Bannister, M. K., Eds. Elsevier Science: Oxford, 2002; pp 1-12.

87. Yang, F.; Zhao, J.; Koshut, W. J.; Watt, J.; Riboh, J. C.; Gall, K.; Wiley, B. J., A Synthetic Hydrogel Composite with the Mechanical Behavior and Durability of Cartilage. *Adv. Funct. Mater.* **2020,** *30* (36), 2003451.

88. Bolat, G.; Mareci, D.; Iacoban, S.; Cimpoesu, N.; Munteanu, C., The Estimation of Corrosion Behavior of NiTi and NiTiNb Alloys Using Dynamic Electrochemical Impedance Spectroscopy. *Journal of Spectroscopy* **2013,** *2013*, 714920.

89. Mareci, D.; Chelariu, R.; Cailean, A.; Sutiman, D., Electrochemical characterization of Ni47.7Ti37.8Nb14.5 shape memory alloy in artificial saliva. *Mater. Corros.* **2012,** *63* (9), 807-812.

90. Li, C.; Zheng, Y. F.; Zhao, L. C., Electrochemical corrosion behaviour of Ti44Ni47Nb9 alloy in simulated body fluids. *Materials Science and Engineering: A* **2006,** *438-440*, 504-508.

91. Flachsmann R; Broom ND; Hardy AE; G., M., Why is the adolescent joint particularly susceptible to osteochondral shear fracture? *Clin. Orthop. Relat. Res.* **2000,** *381*, 212-221.

92. Vercaigne, S.; Wolke, J. G. C.; Naert, I.; Jansen, J. A., Histomorphometrical and mechanical evaluation of titanium plasma-spray-coated implants placed in the cortical bone of goats. *J. Biomed. Mater. Res.* **1998,** *41* (1), 41-48.

93. Du, P. Z.; Markolf, K. L.; Levine, B. D.; McAllister, D. R.; Jones, K. J., Differences in the Radius of Curvature Between Femoral Condyles: Implications for Osteochondral Allograft Matching. *JBJS* **2018,** *100* (15).

94. Yang, F.; Zhao, J.; Koshut, W. J.; Watt, J.; Riboh, J. C.; Gall, K.; Wiley, B. J., A Synthetic Hydrogel Composite with the Mechanical Behavior and Durability of Cartilage. *Adv. Funct. Mater.* **2020,** *30*, 2003451.

95. Kempson, G. E., Relationship between the tensile properties of articular cartilage from the human knee and age. *Ann. Rheum. Dis.* **1982,** *41*, 508-511.

96. Kempson, G. E., Age-related changes in the tensile properties of human articular cartilage: a comparative study between the femoral head of the hip joint and the talus of the ankle joint. *Biochim. Biophys. Acta. Gen. Subj.* **1991,** *1075*, 223-230.

97. Kerin, A. J.; Wisnom, M. R.; Adams, M. A., The compressive strength of articular cartilage. *Proc. Inst. Mech. Eng. H* **1998,** *212*, 273-80.

98. Holloway, J. L.; Lowman, A. M.; Palmese, G. R., The role of crystallization and phase separation in the formation of physically cross-linked PVA hydrogels. *Soft Matter* **2013,** *9*, 826-833.

99. Cha, W.-I.; Hyon, S.-H.; Ikada, Y., Transparent poly(vinyl alcohol) hydrogel with high water content and high strength. *Macromol. Chem. Phys.* **1992,** *193*, 1913-1925.

100. Koshut, W. J.; Smoot, D.; Rummel, C.; Kirillova, A.; Gall, K., Tensile Fatigue of Poly(Vinyl Alcohol) Hydrogels with Bio-Friendly Toughening Agents. *Macromol. Mater. Eng.* **2020,** *305*, 1900784.

101. Yokoyama, F.; Masada, I.; Shimamura, K.; Ikawa, T.; Monobe, K., Morphology and structure of highly elastic poly(vinyl alcohol) hydrogel prepared by repeated freezing-and-melting. *Colloid Polym. Sci.* **1986,** *264*, 595-601.

102. Peppas, N. A.; Merrill, E. W., Poly(vinyl alcohol) hydrogels: Reinforcement of radiation-crosslinked networks by crystallization. *J. Polym. Sci., Polym. Chem. Ed.* **1976,** *14*, 441-457.

103. Cha, W.-I.; Hyon, S.-H.; Oka, M.; Ikada, Y., Mechanical and wear properties of poly(vinyl alcohol) hydrogels. *Macromol. Symp.* **1996,** *109*, 115-126.

104. Oliveira, A. S.; Schweizer, S.; Nolasco, P.; Barahona, I.; Saraiva, J.; Colaço, R.; Serro, A. P., Tough and Low Friction Polyvinyl Alcohol Hydrogels Loaded with Anti-inflammatories for Cartilage Replacement. *Lubr.* **2020,** *8*.

105. Hassan, C. M.; Peppas, N. A., Structure and morphology of freeze/thawed PVA hydrogels. *Macromolecules* **2000,** *33*, 2472-2479.

106. Mavraki, A.; Cann, P., Friction and lubricant film thickness measurements on simulated synovial fluids. *Proc. Inst. Mech. Eng. J* **2009,** *223*, 325-335.

107. Nelson, A. E.; Allen, K. D.; Golightly, Y. M.; Goode, A. P.; Jordan, J. M. In *A systematic review of recommendations and guidelines for the management of osteoarthritis: the chronic osteoarthritis management initiative of the US bone and joint initiative*, Semin. Arthritis Rheum., Elsevier: 2014; pp 701-712.

108. Myant, C.; Cann, P., In contact observation of model synovial fluid lubricating mechanisms. *Tribol. Int.* **2013,** *63*, 97-104.

109. Gong, J. P.; Kagata, G.; Osada, Y., Friction of Gels. 4. Friction on Charged Gels. *J. Phys. Chem. B* **1999,** *103*, 6007-6014.

110. Hassan, C. M.; Peppas, N. A., Structure and Applications of Poly(vinyl alcohol) Hydrogels Produced by Conventional Crosslinking or by Freezing/Thawing Methods. In *Biopolymers · PVA Hydrogels, Anionic Polymerisation Nanocomposites*, Springer Berlin Heidelberg: Berlin, Heidelberg, 2000; pp 37-65.

111. Caligaris, M.; Ateshian, G. A., Effects of sustained interstitial fluid pressurization under migrating contact area, and boundary lubrication by synovial fluid, on cartilage friction. *Osteoarthr. Cartil.* **2008,** *16*, 1220-1227.

112. Li, F.; Wang, A.; Wang, C., Analysis of friction between articular cartilage and polyvinyl alcohol hydrogel artificial cartilage. *J. Mater. Sci. Mater. Med.* **2016,** *27*, 87.

113. Katta, J.; Jin, Z.; Ingham, E.; Fisher, J., Biotribology of articular cartilage—A review of the recent advances. *Med. Eng. Phys.* **2008,** *30*, 1349-1363.

114. Oungoulian, S. R.; Durney, K. M.; Jones, B. K.; Ahmad, C. S.; Hung, C. T.; Ateshian, G. A., Wear and damage of articular cartilage with friction against orthopedic implant materials. *J. Biomech.* **2015,** *48*, 1957-1964.

115. Custers, R.; Dhert, W.; van Rijen, M.; Verbout, A.; Creemers, L.; Saris, D., Articular damage caused by metal plugs in a rabbit model for treatment of localized cartilage defects. *Osteoarthr. Cartil.* **2007,** *15* (8), 937-945.

116. Du, P. Z.; Markolf, K. L.; Levine, B. D.; McAllister, D. R.; Jones, K. J., Differences in the Radius of Curvature Between Femoral Condyles: Implications for Osteochondral Allograft Matching. *J. Bone Jt. Surg.* **2018,** *100*, 1326-1331.

117. Bergmann, G.; Bender, A.; Graichen, F.; Dymke, J.; Rohlmann, A.; Trepczynski, A.; Heller, M. O.; Kutzner, I., Standardized Loads Acting in Knee Implants. *PLoS One* **2014,** *9*, e86035.

118. Brown, T. D.; Shaw, D. T., In vitro contact stress distribution on the femoral condyles. *J. Orthop. Res.* **1984,** *2*, 190-199.

119. D'Lima, D. D.; Patil, S.; Steklov, N.; Chien, S.; Colwell Jr, C. W., In vivo knee moments and shear after total knee arthroplasty. *J. Biomech.* **2007,** *40*, S11-S17.

120. Yasuda, K.; Ping Gong, J.; Katsuyama, Y.; Nakayama, A.; Tanabe, Y.; Kondo, E.; Ueno, M.; Osada, Y., Biomechanical properties of high-toughness double network hydrogels. *Biomaterials* **2005,** *26* (21), 4468-4475.

121. Gong, J. P.; Kurokawa, T.; Narita, T.; Kagata, G.; Osada, Y.; Nishimura, G.; Kinjo, M., Synthesis of Hydrogels with Extremely Low Surface Friction. *Journal of the American Chemical Society* **2001,** *123* (23), 5582-5583.

122. Kaneko, D.; Tada, T.; Kurokawa, T.; Gong, J. P.; Osada, Y., Mechanically Strong Hydrogels with Ultra-Low Frictional Coefficients. *Advanced Materials* **2005,** *17* (5), 535-538.

123. Golafshan, N.; Rezahasani, R.; Tarkesh Esfahani, M.; Kharaziha, M.; Khorasani, S. N., Nanohybrid hydrogels of laponite: PVA-Alginate as a potential wound healing material. *Carbohydrate Polymers* **2017,** *176*, 392-401.

124. Li, Y.; Maciel, D.; Tomás, H.; Rodrigues, J.; Ma, H.; Shi, X., pH sensitive Laponite/alginate hybrid hydrogels: swelling behaviour and release mechanism. *Soft Matter* **2011,** *7* (13), 6231-6238.

125. Tomás, H.; Alves, C. S.; Rodrigues, J., Laponite®: A key nanoplatform for biomedical applications? *Nanomedicine : nanotechnology, biology, and medicine* **2018,** *14* (7), 2407-2420.